Al-Cr-N thin film design for high temperature applications

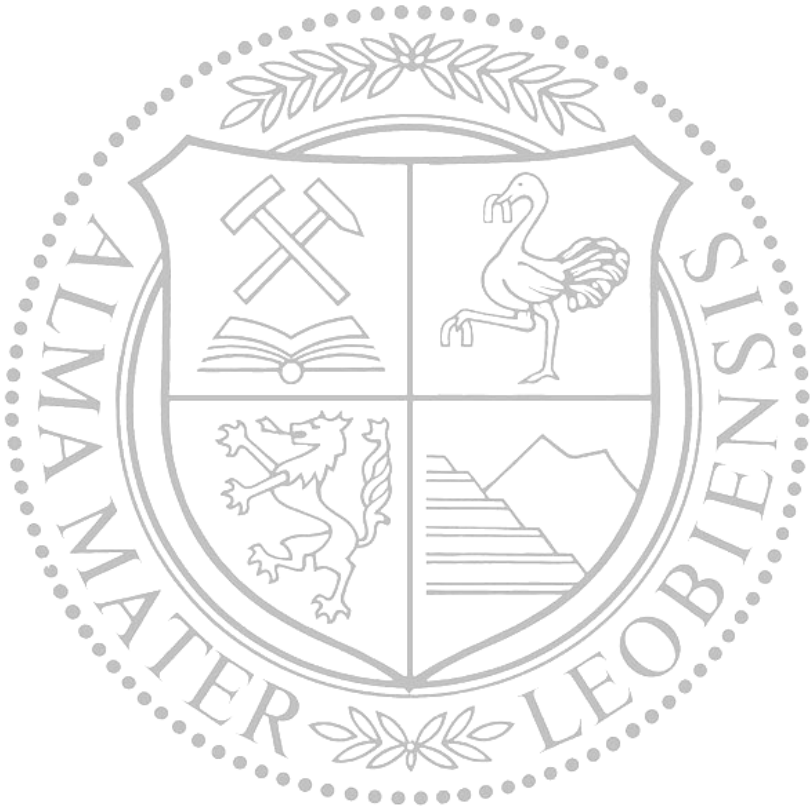

Dipl.-Ing. Herbert Willmann

Being a thesis in partial fulfillment of the requirements for the degree of a

Doctor of Montanistic Sciences (Dr.mont.)

at the Montanuniversität Leoben

Leoben, July, 2007

This thesis was supported by the Technologie Impulse GmbH in the frame of the K-plus Competence Center program at the Materials Center Leoben Forschung GmbH.
Research activities at the Linköping University, Sweden were financed by a Marie Curie training site scholarship within the fifth framework program of the European Union and by the University itself.

Affidavit

I declare in lieu of oath that I did the PhD thesis by myself using only literature cited in this volume.

Leoben, July 2007

(Herbert Willmann)

Acknowledgements

Throughout my years as a PhD student I had the great pleasure to meet a lot of interesting people from around the globe, who supported and helped me at work and made my private life by far more enjoyable. Here is the right place to name some of them.

First of all, I want to express my gratitude to Paul Mayrhofer, who initially persuaded me to start with this project, for his guidance, advice, and all the encouraging words over the last years. Most valuable for me, however, are not his outstanding scientific skills, but his friendship.

In equal measure I want to thank Christian Mitterer and Lars Hultman for their support, supervision, and perfect handling of the project 'Herbert' in sense of scientific and financial concerns. It was a great pleasure to work within their groups. Without a doubt it is difficult to find better bosses, especially ones who also share my interests in sweets, sport, and a proper way of living.

I am very indebted to my employer, the Materials Center Leoben, and the managing director Reinhold Ebner, for giving me the opportunity to be a member of the team. My sincere gratitude goes also to all the helpful people handling my administrative issues, either in Leoben or in Linköping. Furthermore, I want to thank my partners in industry, Andreas Reiter (Oerlikon Balzers Coating) and Peter Polcik (Plansee GmbH Lechbruck), for their valuable contributions to my research.

Special thanks to my office mates; Gert Gassner for all the endless chats and his interesting view of life, making my own problems look meaningless; and David Hochauer for rescuing my day so frequently by providing a piece of chocolate out of his enormous supply, always with perfect timing.

Many thanks also to all my colleagues (past and present) in the Thin Film Physics and Plasma & Coating Physics divisions of the Linköping University, for all the lunches, 'fikas', and Friday cakes we had together. Especially to Manfred Beckers, Carina Höglund, Martina Lattemann, and David Trinh for their work and non-work related discussions as well as to Jens Emmerlich, Axel Flink (my personal golf guru), and Timo Seppänen, for great Swedish golf experiences.

My sincerest appreciation is due to all my colleagues and friends based in the individual groups of the Department of Physical Metallurgy and Materials Testing at the Montanuniversität Leoben. Especially, Harald Chladil and Gerardo Fontalvo for our annual birthday party and for sharing my passion for single malt Whiskies. Also Kerstin Kutschej, Martin Moser, Jörg Neidhardt, Martin Pfeiler, and Josef Wagner for making the daily life at and beside work so enjoyable.

Inexpressible thanks to my family and my beloved girlfriend Barbara Jeitler who motivated and encouraged me during the whole time. At the end of the day it was them, who listened to the reports of my victories and defeats, always finding the right words to keep me on track. Without their trust and support it would not have been possible to reach the goal.

Table of contents

1 Introduction

New developments require people with ideas. Some ideas are outstanding and others may be less successful. Some concepts are probably easy to take to reality, for others it seems that it is just not the right time for them, just because several requirements are missing. However, one of the missing ingredients for approaching new frontiers is quite often the proper material which can fulfill the highflying requirements of such visions. Help as well as inspiration for solving such problems is offered by materials science since ancient times. This interdisciplinary field of science deals with condensed matter, the connection between processing, structure, properties and performance and tries to use the achieved understanding for continuous developments for better and more advanced materials. The approaches for improvements of materials are as manifold as their demands. Nowadays it becomes difficult to develop materials which can fulfill all the severe requirements and are simultaneously easy handle and to shape at the same time. Therefore solutions were generated, where the tailored material is applied just where it is necessary. These so called material compounds allow a combination of economical considerations with a simultaneous optimization of performance. One segment in this wide field is the thin film and coating business, where the surface of a tool or a work piece gets modified to fulfill a certain purpose. This can be the utilization of a physical property of the applied film (or stack of films) like in the semiconductor industry, or the use of an optimized material for the sake of their protective properties like in cutting tool applications. The thin film business has developed rapidly over the last few decades, referring to applications, film materials, and fabrication technologies. Modern film materials themselves are extremely interesting also because physical vapor deposition techniques enable the stabilization of phases far from thermodynamic equilibrium. Therefore, solid solutions of materials can be realized which would not be possible with methods of conventional production. Such materials show outstanding properties and property combinations. On the one hand, they can simply show increased mechanical properties, thermal stabilities, better resistances against certain media, or just different optical appearance. On the other hand, these materials, containing the right composition and arrangement of elements in their

crystallographic structure, exhibit interesting qualities especially in self-adaptation to the operational demands like age-hardening or self-lubrication. This becomes even more interesting due to the limited dimensions of such films, at least in one dimension. Studying the related material effects, resulting in the desired and observed macroscopic responds, requires the most sophisticated investigation techniques available in modern materials science.

The topic of this work is deep within this explained field of materials science and deals with protective hard coatings for industrial applications. Already the deposition of such materials is of high interest, and is therefore also covered in this work. However, the main focus here is in the analytical part, where the structure-property relations of a model coating system (Al-Cr-N) were investigated during thermal load for various chemical compositions. To be able to address all emerging questions and understand ongoing reactions in industrial coatings, selected film compositions were also synthesized in single-crystal form. This approach disclosed details of the materials which were necessary to pinpoint the origins accountable for observed effects. Hence, necessary knobs for optimization and tailoring the coating for the corresponding need could be identified. Even though the direct transfer of this knowledge to a completely different coating system is not simple, the basic concepts and their achieved detailed understanding may be helpful for developments of the next generation of protective hard coatings.

The following chapters of this thesis provide a summary of the used Al-Cr-N model material and give an introduction to the used deposition and analysis techniques. Furthermore, they contain results which are not included in the scientific publications presented at the end of this work.

2 Hard coatings

All commercially relevant hard coatings are nowadays ceramic based materials and are primarily used for protective purposes. These can be manifold and cover protection against thermal loads, corrosion, and oxidation. Sometimes, hard coatings simply enable the underlying material to withstand the mechanical demands resulting from the application. Biggest segment of the wear protective coating business are tools for cutting and forming applications. Some parts of this industry, e.g. gear cutting, are early users and employ new developments or materials in the coating sector, as long as a performance increase is observable. However, there is no universal coating on the market today which could satisfy all needs. A lot of optimization of consisting materials in sense of structure-property relation was done in the last few decades, and the materials are becoming more and more complex, already pointing towards multinary coatings. Nevertheless, there are still unexplored and unexplained fields on the knowledge map of binaries and ternaries which are necessary for a detailed understanding to further develop such coating materials.

2.1 Binary systems

In the class of protective coatings, mainly binary materials were used in industry for several years. The most prominent representatives are TiC, TiN, and Al_2O_3 which are still heavily used nowadays. Here, one should also draw the attention to other industrial fields, e.g. optical coatings or semiconductor industry, where also different thin film materials are in use. The focus of this work, however, are ceramic based protective hard coatings, and there, especially nitrides. These binaries are the basis for further developments in coating technologies, and therefore the understanding of ongoing reactions in the materials and their response to the partly severe operating conditions is crucial. Only with this knowledge it is possible to improve the performance by a structured scientific approach.

2.1.1 Cr-N

In the binary System Cr-N several compounds can be found [1]. Most interesting for this work is CrN having NaCl (B1) structure (Fig. 2.1a) with a lattice parameter a of 4.140 Å [2]. In literature values range up to 4.160 Å, measured for epitaxially grown films [3]. Below 260-270 K there is a transition from the paramagnetic to the antiferromagnetic state in CrN connected with a resulting change in lattice structure to orthorhombic [4,5]. Also studies on the electronic structure are reported [6,7] whereas CrN has mainly metallic bonding character. Like most of the transition metal nitrides, CrN has been studied extensively and, therefore, plenty of experimental and calculation results are documented in literature [8]. CrN exhibits a small compositional range and it decomposes at relatively low temperatures dependent on the nitrogen partial pressure [1]. At atmospheric pressure this temperature is at ~1000 °C but especially for thin films the experimentally obtained values rank from 400 °C [9] to ~1000 °C [10-12] dependent on the quality of the films and the annealing conditions. A deficiency of nitrogen during the preparation of CrN leads to the formation of a two phase compound or even a single-phase Cr_2N coating [10]. This crystal structure is reported to be hexagonal closed packed (hcp) for the Cr-atoms with a random arrangement of the N-atoms at the interstitial sites [13] (a = 2.744 Å, c = 4.429 Å [14]) which is displayed in Fig. 2.1b.

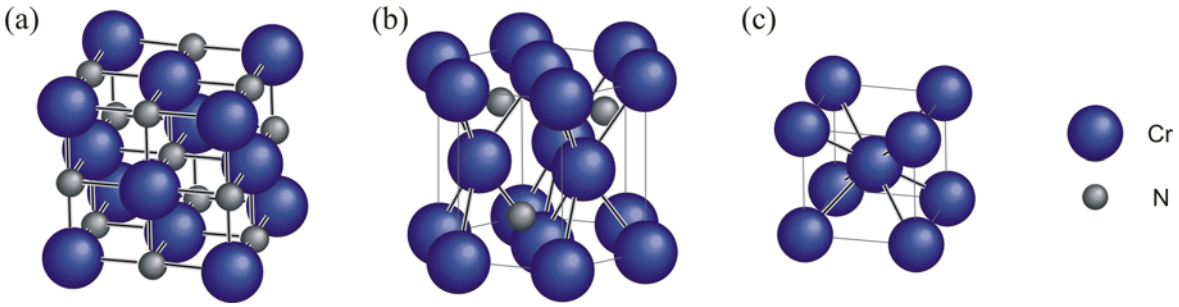

Fig. 2.1. Lattice structures of a) NaCl structure CrN, b) hexagonal Cr_2N, and c) bcc Cr.

The stochastically positioned N-atoms in the Cr_2N are part of a superstructure with a unit cell of $a' = a \cdot \sqrt{3} = 4.752$ Å and $c' = c = 4.429$ Å [14]. At room temperature Cr_2N has a existence range down to $Cr_2N_{0.9}$ [1] which becomes larger for higher temperatures and can

tolerate substoichiometries up to >10 at% [1]. Also Cr_2N exhibits a decomposition point which is dependent on the present nitrogen partial pressure. Pure Cr crystallizes in the body-centered cubic structure (bcc), see Fig. 2.1c. High-pressure or low-temperature modifications of compounds in this material system are not considered in this work. A detailed description of the different compounds and their physical, mechanical and thermal properties can be found in [15].

CrN coatings are, next to TiN, one of the classical universal nitride coatings which are used since the 1980s [16-18]. Nowadays, several developments of ternary and multinary films build up on this binary system, however, it is still extensively used in industry as single-phase CrN. The fields of application are based on the good hardness, oxidation resistance, chemical inertness, and anti-adhesive properties resulting in predominant use as protective coating for metal forming and plastic molding tools [19-22].

However, the need for increasing productivity also changes the demands for tools and their coatings. Technologies like high-speed or dry cutting generate conditions at certain points of the tools which limit the usability of pure single-phase CrN coatings. Limiting properties are next to the hardness mainly the thermal stability and missing low friction abilities.

2.1.2 Al-N

The only compound in the Al-N system [23] is the mainly covalently bonded AlN (with ionic but no metallic contributions [24,25]). It is stable in the hexagonal wurtzite-type (B4) crystal structure, see Fig. 2.2a, and decomposes at ~2800 °C in nitrogen atmosphere. The lattice parameters are a = 3.1114 Å and c = 4.9792 Å [26], whereas there exists also a high-pressure modification which has NaCl-structure (Fig. 2.2b) with a lattice parameter of a = 4.0450 Å [27]. The cubic ZnS-structure (B3) could be stabilized in epitaxial growth for some nm [28-30] with a resulting lattice parameter of a = 4.38 Å [30,31], shown in Fig. 2.2c. AlN in the B4 modification is a semiconductor material with an extremely wide band gap of 6.2 eV [32] which is interesting for ultraviolet optoelectronics. It is used for surface acoustic wave devices [33], field emission cathodes

[34], and gate dielectrics in high power, high frequency metal-insulator-semiconductor transistors [35], and also shows piezoelectric properties. As semiconductors in general, also AlN is subject of intensive investigations why values on electrical, optical, thermal, and mechanical properties are easily available in literature and are even collected in well documented databases [36].

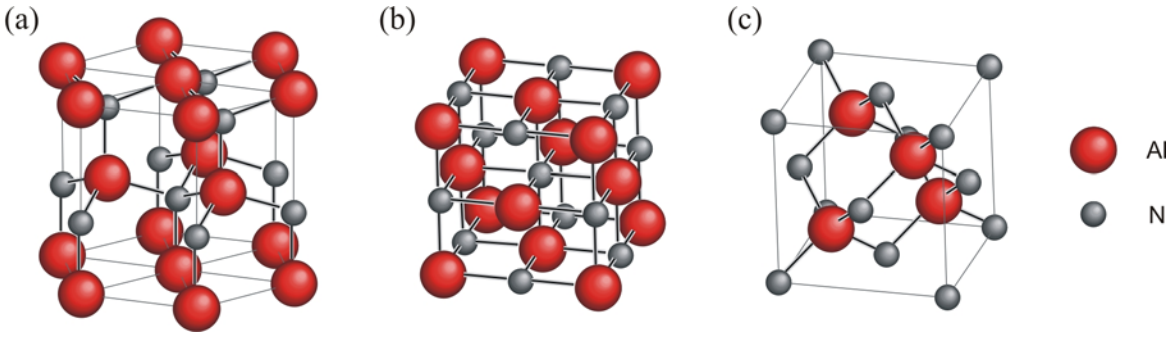

Fig. 2.2. Possible crystal lattice structures of AlN. a) Wurtzite, b) NaCl, and c) ZnS type.

2.2 Ternary system Al-Cr-N

Alloying of materials to improve their properties is used since ancient times. Unfortunately not every composition can be realized with standard production technologies (e.g. melting) due to thermodynamic restrictions. For thin films and there especially ternary hard coatings there are different ways of production via deposition, where a widely used technique is physical vapor deposition (PVD), described in the next chapter. This enables the generation of materials far from thermodynamic equilibrium. One of the most prominent representatives for ternary hard coatings was developed in the 1980s on the base of TiN. The addition of Al leads to the formation of the nowadays well known $Ti_{1-x}Al_xN$ which shows improved hardness and oxidation resistance compared to binary TiN. Considering the significantly improved properties of $Ti_{1-x}Al_xN$ and the great success as protective coating, it was just a logical step to carry this approach forward to CrN, which is superior to TiN in several applications. Candidates for suitable alloying elements were ZrN and TiN to form $Zr_xCr_{1-x}N$ and $Ti_xCr_{1-x}N$, respectively [20]. In 1989 [37] and at the beginning of the 1990s, first reports on the synthesis of films in the Al-Cr-N system were

published using magnetron sputtering [38,39] followed by first results on corrosion behavior and wear tests [37,39-41]. At the end of the 1990s interest in AlCrN coatings was rising significantly and the number of publications became quite remarkable [20,42-48]. Today the high interest in this coating system is of course triggered by the outstanding properties which make this coating system superior to the state of the art coatings in many applications. Therefore AlCrN coatings are nowadays commercially available at the market (Balinit® Alcrona, Oerlikon Balzers Coating). AlCrN is recommended as a protective coating for mills and cemented carbide indexable inserts for roughing and finishing as well as for cubic boron nitride indexable inserts for turning. Due to the high oxidation resistance, wear resistance, and thermal stability combined with the chemical inertness and good hot hardness it is also a good choice in aluminum die casting and hot forging. This is fostered by several independent investigations reported in literature, also showing potential of this coating for other applications.

Best performance in machining tests was obtained for stoichiometric AlCrN coatings with Al/Cr ratios in the range of 50/50 to 70/30 [49,50]. Most results are available for metal cutting where the performance enhancement is most pronounced for applications with interrupted cuts [49,51]. Nevertheless, results on dry turning are promising [52]. Considering interrupted turning tests, AlCrN was superior to state of the art ternary coatings like TiCN and TiAlN [51]. End milling tests of structural ferrite-perlite steel with coolant showed a reduced flank wear of AlCrN coated tools compared to TiAlN [53] and also for dry end milling of austenitic stainless steel, an increased performance in sense of cutting length was observed [54]. Also in wet drilling, AlCrN outperforms the nowadays used TiAlN [50,55] why a partial replacement in milling and drilling operations can be foreseen [56]. Tools for punching, gear shaping, and sheet perforation show at least performance/life time increases of 200% compared to the used standard coatings. Therefore, in some cases a substitution in aid for AlCrN coatings would result in reduced tooling costs [51,55]. This material was also successfully applied as protective layer for stamping and forging tools [56]. Initial tests for roller bearings showed best results of fine grained AlCrN coatings [57] and also tests for high end spindle bearings are promising [58].

Developments are aiming towards multinary coating systems based on AlCrN for tailoring required properties with the goal of further performance increase of the corresponding coated tool [59]. Nevertheless, there is still enough room for improvement by optimizing the production parameters and therefore the required properties of the ternary coating.

The reported approaches for synthesizing films within the system Al-Cr-N are quite manifold, and cover direct current (DC) sputter deposition [38-40,43,45,60-72], radio frequency (RF) sputter deposition [46-49,52,73], combined DC/RF sputter deposition [74-77], arc evaporation [41,50,51,53,54,56,70,78-88] (filtered arc [89,90]), pulsed laser deposition [91,92], and electron beam evaporation [55]. All depositions were performed in reactive atmosphere except one work which reports on pulsed laser deposition from Cr_2N and AlN targets [92]. However, the authors report significant amounts of oxygen in the films due to residual gases. There is no trend detectable if two single elemental targets or one compound/alloyed target is favored for a certain deposition technique. AlCrN films deposited by PVD techniques show in general good adhesion [49,55,57,58,70,84] and exhibit compressive stress [50,73,84]. Films with different stoichiometries are reported in literature, whereas the focus of this work lies on pseudobinary $Al_xCr_{1-x}N$ coatings along the CrN-AlN tie line. The investigated films were deposited by reactive arc evaporation as well as reactive unbalanced DC magnetron sputtering (UBMS) from compound targets with different Al/Cr ratios.

2.2.1 Crystal structure

This work deals with stoichiometric nitride films along the pseudobinary tie line CrN-AlN. The binary nitrides AlN and CrN with wurtzite and rock salt crystallographic structures, respectively, have very low solubility for each other in thermodynamic equilibrium. This can be seen in Fig. 2.3 by a calculated isothermal cut of the ternary phase diagram Al-Cr-N at 1000 °C and 10^5 Pa (1 bar) [48]. Also other Al-Cr-N phase diagrams, composed out of the binary phase diagrams Al-N [23], Cr-N [1], and Al-Cr [93,94], can be

found in literature [95,96] and all of them confirm the limited solubility of AlN and CrN for each other.

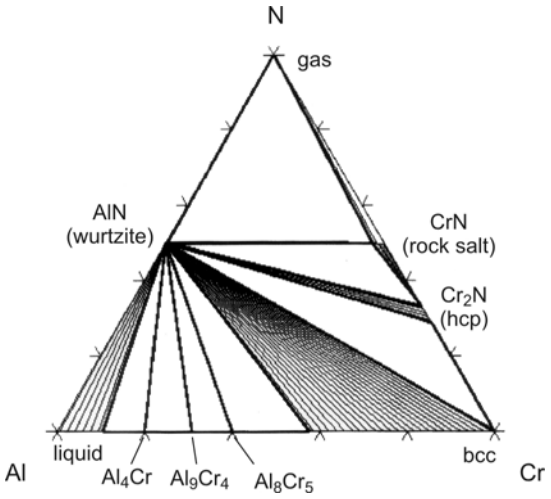

Fig. 2.3. Isothermal cut at 1000 °C of the ternary phase diagram Al-Cr-N [48].

By synthesis via PVD it is possible to stabilize metastable solid solutions of $Al_xCr_{1-x}N$ in crystallographic modifications of the corresponding binary systems, where Al and Cr atoms are substituting each other. The evolved structure is dependent on the chemical composition and can be described along the pseudobinary tie line either with start on the cubic (rock salt, B1) CrN or the hexagonal (wurtzite type, B4) AlN side which is illustrated in Fig. 2.4.

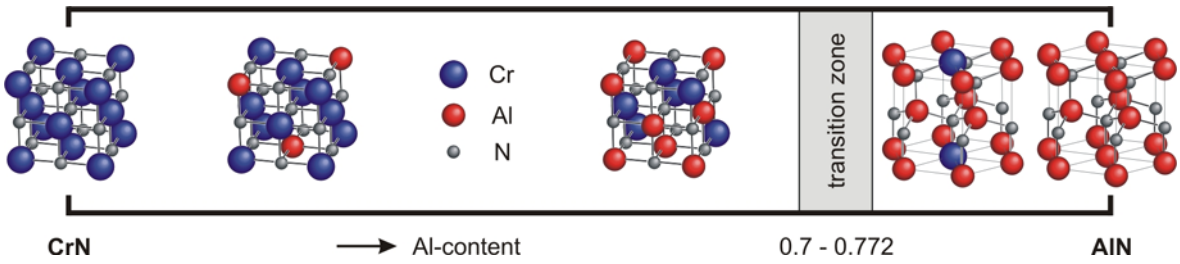

Fig. 2.4. Structural developments along the pseudobinary tie line AlN-CrN. The transition zone between the CrN based rock salt structure and the AlN based wurtzite type AlCrN is indicated by the grey area defined by values obtained experimentally [47,50,91] and calculations [97].

Calculations on the maximum metastable solubility of AlN in cubic CrN by the band parameters method based on the concept of localized electron theory yield a value of

77.2 at% [97]. Ab-initio calculations result in 50-75 at% dependent on the configuration of the Al and Cr atoms in the unit cell [98]. Experimental results on the highest achieved incorporated Al content in the cubic modification are dependent on the used deposition technique. The stated compositions are $Al_{0.7}Cr_{0.3}N$ for sputtering [47], $Al_{0.71}Cr_{0.29}N$ for arc evaporation [50], and $Al_{0.75}Cr_{0.25}N$ for pulsed laser deposition [91].

In this work, the focus lies on compositions close to this transition but within the cubic phase field; nevertheless also the question of the exact B1/B4 transition is addressed. Using heteroepitaxial growth experiments by reactive unbalanced magnetron sputtering on single-crystal MgO substrates revealed stabilization of a ~100 nm thick $Al_{0.81}Cr_{0.19}N$ layer at the interface followed by growth of columnar wurtzite type $Al_xCr_{1-x}N$. This is the highest Al-content in c-$Al_xCr_{1-x}N$ among all the reported values in literature, also exceeding the calculated theoretical limit. The chemical composition was determined with Rutherford backscattering spectroscopy (RBS) with an accuracy of ±1% for Al and Cr and ±2% for the lighter N. Fig. 2.5 shows transmission electron microscopy (TEM) results of such a film.

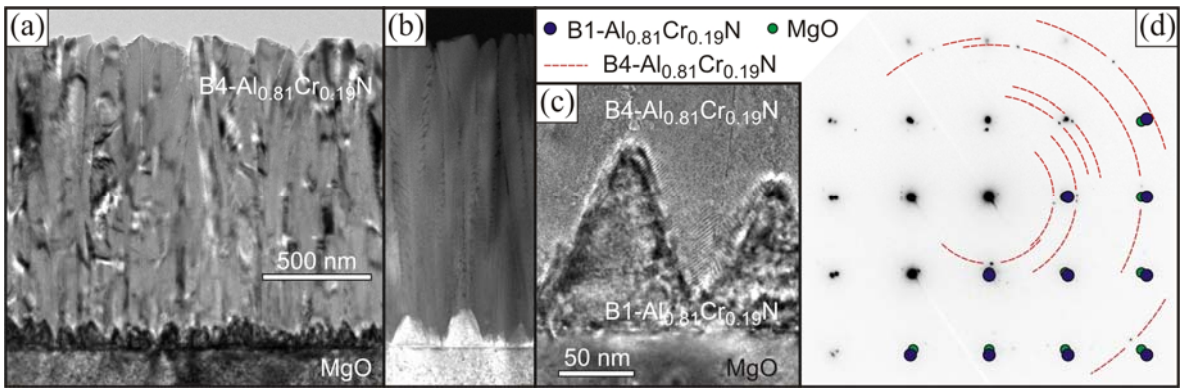

Fig. 2.5. (a) Cross-sectional BF-TEM of an $Al_{0.81}Cr_{0.19}N$ film epitaxially grown on MgO(001) with a stabilized c-$Al_{0.81}Cr_{0.19}N$ interlayer and the corresponding STEM image with z-contrast (b). (c) Detailed view of the interlayer. SAD pattern of this area with theoretical positions for single-crystal MgO and c-$Al_{0.81}Cr_{0.19}N$ as well as rings for w-$Al_{0.81}Cr_{0.19}N$ are displayed in (d).

Cross-sectional bright-field (BF) transmission electron micrograph Fig. 2.5a and the corresponding scanning transmission electron microscopy (STEM) image recorded under optimized conditions for mass/density contrast in Fig. 2.5b display this interlayer followed

by columnar growth. The shape of this interlayer is shown by the detailed view of the BF-TEM in Fig. 2.5c exhibiting pyramids of c-$Al_xCr_{1-x}N$. These features appear bright compared to the w-$Al_xCr_{1-x}N$ columns in the STEM image Fig. 2.5b, indicating higher mass/density, due to the ~26% lower molar volume of the rock salt structure compared to the wurtzite one for the same chemical composition. Selected area electron diffraction (SAD) of such an interface region (Fig. 2.5d) reveals epitaxial growth of fully relaxed c-$Al_xCr_{1-x}N$ on MgO(001) matching the theoretical positions as indicated by the different colored spot patterns. Traces of polycrystalline w-$Al_xCr_{1-x}N$ (indicated by segments of theoretical diffraction rings) are also present as a result of the investigated area extending also to the w-$Al_xCr_{1-x}N$ columns.

Substituting Cr atoms by Al in the rock salt structure has significant influence on the bonding characteristics. The metallic character of CrN is due to the overlapping d-orbitals of the Cr and adding Al without d-electrons decreases the density of states at the Fermi level. This leads to hybridized (p-d) states resulting in covalent/ionic character between the N p and metal d-p orbitals [74] which also explains the improved mechanical properties of the ternary compound. This change in bonding characteristics results also in different bonding lengths leading to different lattice parameters dependent on the chemical composition. Several authors have published lattice parameters [45-47,50,66,70,74,77,85-88,91,99] where the results for the films with rock salt modification are summarized in Fig. 2.6 and compared to the obtained values from this work. Even though the absolute values for the different cubic films scatter over a wide range, it is clearly visible that the lattice parameter is not behaving according to Vegard's rule. This, however, was anyway not expected due to the drastic change in bonding character. Reference values for pure CrN and cubic AlN are included in the diagram for comparison. The presented values of this work, from arc evaporated films and epitaxially grown AlCrN on MgO(001) and MgO(111) substrates by reactive unbalanced magnetron sputtering (UBMS), are indicated with black solid symbols.

Hexagonal w-$Al_xCr_{1-x}N$ on the other hand shows an anisotropic lattice expansion for increasing the Cr-content in the AlN [87]. While there is an expansion along the basal plane (increasing a value), the c-axis shrinks slightly which was also observed in this work.

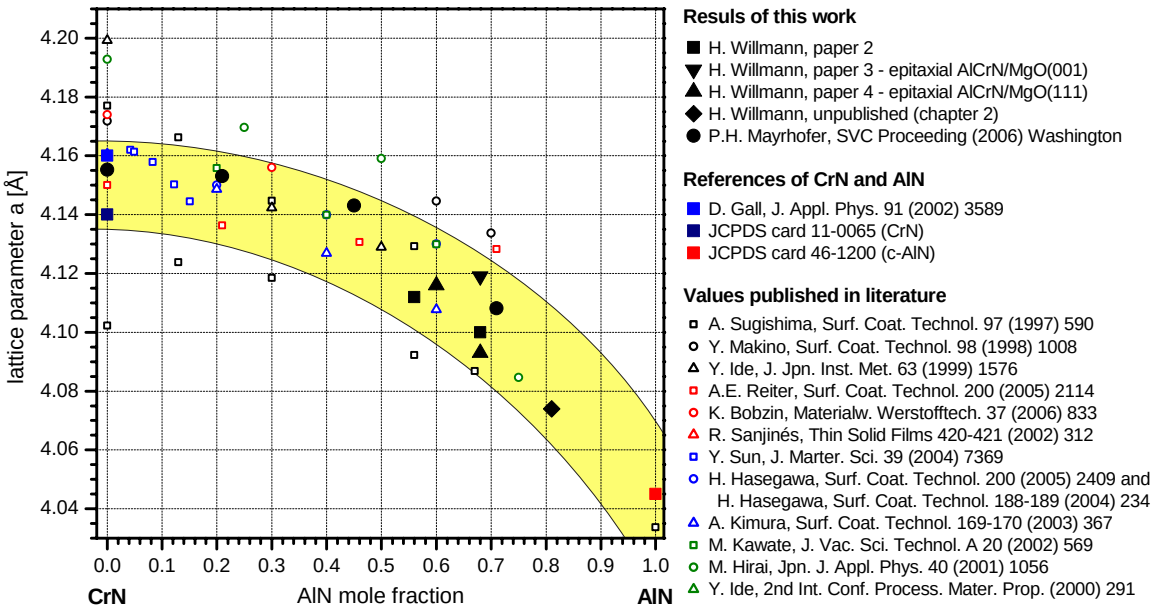

Fig. 2.6. Lattice parameters of rock salt structure $Al_xCr_{1-x}N$ films. Results of this work compared with reported literature values, including CrN and c-AlN references.

2.2.2 Mechanical and tribological properties

One of the most documented properties in the material system Al-Cr-N is hardness. Due to the explained changes in the bonding characteristics within the ternary Al-Cr-N phase diagram, the hardness is also a function of the chemical composition. Reported values for comparable compositions, however, show a significant scatter which may result from differences in achieved microstructure due to the used deposition technique/parameters or probably just inadequate measurement parameters. The factor of different hardness measurement equipments should also not be neglected, where a critical review on this topic is available in literature [100]. However, the majority of the results state an indentation hardness increase with Al-content for c-$Al_xCr_{1-x}N$ from ~23 GPa for CrN [101-103] to ~32 GPa close to the B1/B4 transition [43-45,48,50,53-55,58,63-65,67,68,70-73,79,84-86,88,91,99], but also values up to 40 GPa are reported [41,69,80]. The corresponding elastic modulus is comparably seldom reported and shows even higher scatter (~200-600 GPa) [43,53-55,58,67-72,79,80,84]. Measurements on single-crystal $Al_{0.68}Cr_{0.32}N$ (paper 3) yield 32.4 GPa indentation hardness and 460 GPa elastic modulus. Considering temperature effects on the hardness, c-$Al_xCr_{1-x}N$ shows high hot hardness

[53], the hardness for post annealed films decays or is stable up to ~1000 °C dependent on the structure and conditions used [50,65,69,91,99]. At these temperatures, the thermal stability of the substrate and interdiffusion between substrate and film becomes important. In this work no change in hardness up to 1100 °C for c-$Al_{0.56}Cr_{0.44}N$ on cemented carbide inserts was detected (paper 2). It was also found that for chemical compositions close to the B1/B4 transition (arc evaporated $Al_{0.68}Cr_{0.32}N$ coatings) a precipitation hardening effect leads to a hardness increase at ~750 °C. Paper 2 shows a detailed study on this topic. A further increase in Al-content with a corresponding change on crystal structure (w-$Al_xCr_{1-x}N$) results in an abrupt decrease in hardness to values of ~15 GPa [91,99] which are close to that of w-AlN [50,86,88].

Results on residual stresses in $Al_xCr_{1-x}N$ PVD films are rarely reported. In general they are compressive [73] and increase with film thickness [84]. Starting from pure CrN with moderate values of -1 to -1.5 GPa [15,50], an increasing Al-content leads to a peak in residual compressive stresses of -5 GPa for Al/Cr ratios of ~50/50 with a subsequent decrease to -3.5 GPa close to the B1/B4 transition [50]. For films in the wurtzite modification the compressive stresses are generally smaller than -2 GPa [50].

Also the tribological properties of AlCrN are of great interest and therefore, subject of investigation. Results on reciprocal sliding [52] and pin-on-disc tests at room temperature [41,44,61,62,66,69,70,72,79,80,82,99] and elevated temperatures (500 °C) [99] show no low friction behavior. However, the wear resistance is excellent [55,67] and the abrasive wear is superior to other ternary coatings [51]. Even though the wear rate increases with temperature [99] and is dependent on residual stress and hardness [50], this may be considered as a key property for the good performance as protective hard coating. In combination with the good oxidation resistance, $Al_xCr_{1-x}N$ is also a candidate for the protection of semi-solid Al-metal forming dies being an extremely material demanding production process [61].

2.2.3 Thermal properties

Modern machining and forming applications continuously generate increasing demands on the tools and therefore, their protective overcoat. One major aspect is the resulting high temperature which can exceed even 1000 °C during operation. At these temperatures factors like thermal stability of the coating as well as the resistivity against reactions with the ambient atmosphere are crucial. Increasing the stabilities against disintegration or oxidation is one of the driving forces for developments in the coating business which lead i.e. to ternary compounds. $Al_xCr_{1-x}N$ is based on CrN which has a limited thermal stability and decomposes under the release of nitrogen to pure Cr via the intermediate step of Cr_2N [11,12,15]. For optimization of $Al_xCr_{1-x}N$ coatings in this respective, the influence of Al on these decomposition processes and a detailed understanding of the ongoing reactions are necessary. Investigations of the coatings by post-deposition annealing in inert atmosphere were performed up to 1500 °C (paper 1) [12,50,78]. Simultaneous thermal analysis (STA) measurements on coatings with different chemical composition within this work showed a stabilizing effect with increasing AlN-content (see chapter 6.1.1). A significant improvement of the onset of decomposition (~120 °C) was achieved for AlN-contents >45% [12]. Cubic $Al_xCr_{1-x}N$ films with compositions close to the B1/B4 transition show precipitation of w-AlN starting at temperatures of ~650 °C (paper 1 and 2). The resulting depletion of Al in the matrix on the other hand weakens the resistance against decomposition slightly. The decomposition route is obviously dependent on the present crystallographic modification of the $Al_xCr_{1-x}N$ [12,50] and is schematically displayed in Fig. 2.7 for c-$Al_xCr_{1-x}N$ (a) and w-$Al_xCr_{1-x}N$ (b) close to the B1/B4 transition. Whereas for c-$Al_xCr_{1-x}N$ films a decomposition route similar to CrN was detected, however with elevated onset temperatures and possible w-AlN precipitation, w-$Al_xCr_{1-x}N$ is based on w-AlN with a thermal stability of ~2800 °C, see paragraph 2.1.2. For these coatings precipitation of CrN was observed with an encapsulation in a stable w-AlN matrix. This matrix depicts an effective diffusion barrier which results in combination with the different nitrogen partial pressure for the precipitates in very high observed decomposition temperatures for CrN (paper 2) [12].

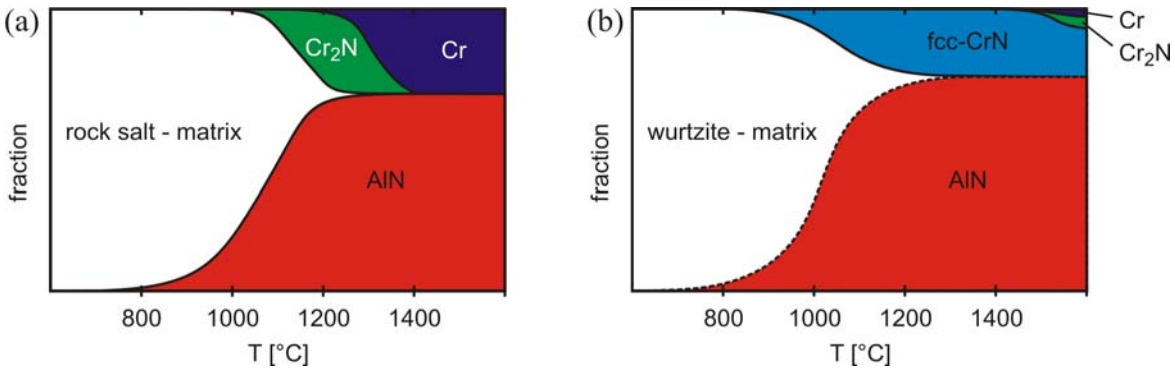

Fig. 2.7. Schematic decomposition rout of (a) c-$Al_xCr_{1-x}N$ and (b) w-$Al_xCr_{1-x}N$ with x close to the transition point (modified after [12]).

The strong influence of the nitrogen partial pressure on the decomposition behavior of $Al_{0.56}Cr_{0.44}N$ could be investigated in this work and is presented in paper 2. Also the influence of oxygen containing atmospheres is investigated in this paper which is also of major interest for several applications and is therefore addressed intensively in literature [44,54,68,76,90,91,99]. The oxidation resistance increases with the Al-content for c-$Al_xCr_{1-x}N$ [50,75,83] and for compositions close to the B1/B4 transition it is approximately five times higher than for CrN in air up to ~1000 °C [39,51]. As for the mechanical properties also the oxidation resistance decreases for w-$Al_xCr_{1-x}N$ with an almost tripled oxidation rate [50,56]. Annealing temperatures of ~900 °C result in the formation of a very dense thin oxide on c-$Al_xCr_{1-x}N$ which makes it superior to other ternary nitride coatings [51,83], as thereby further oxidation is inhibited. The kinetics follows a parabolic law [60] and the activation energy for oxidation is reported to be ~150 kJ/mol [39]. The improved resistance compared to CrN results from the changed oxide formation mechanism due to the presence of Al. Detailed investigations on the oxide were performed by x-ray diffraction (XRD), electron microscopy, x-ray photoelectron spectroscopy (XPS) [56], secondary ion mass spectroscopy (SIMS) [78], Raman investigations [65,79,81] as well as several techniques for elemental analysis. The formation model of the oxide layer proposes several steps how oxygen reacts with $Al_xCr_{1-x}N$. In the early stages, Cr_2O_3 and Al_2O_3 are formed simultaneously at the surface. This results in a thin layer of solid solution $(Al,Cr)_2O_3$ [60,75] which acts as a diffusion barrier. The limiting step for further oxidation therefore is the inward diffusion of oxygen to the $Al_xCr_{1-x}N$. Considering the cations it is Cr which diffuses outwards due to the lower

affinity to oxygen compared to Al which will be bonded in the oxide. However, the diffusion speed of Cr in the mixed $(Al,Cr)_2O_3$ decreases with increasing Al-content resulting in a homogeneous oxide for $Al_xCr_{1-x}N$ films with high Al-contents. For low Al-contents (i.e. $Al_{0.18}Cr_{0.82}N$) and long oxidation times, the formation of pure Cr_2O_3 grains were observed at the surface of the oxide layer [60] due to the possibility of the Cr ions to reach the surface and react with oxygen. The oxidation, however, is accompanied with the decomposition of the $Al_xCr_{1-x}N$ having nitrogen as a gaseous reaction product. Compared to the beginning of the oxidation, at a later stage the formed nitrogen at the interface has to diffuse through the oxide layer which goes easily compared to i.e. Cr or O and is therefore no crucial time limiting step [60].

2.2.4 Physical and chemical properties

Optimum performance of coatings in cutting applications is a complex combination of several properties, i.e. thermal conductivity defines the amount of heat from the cutting process transferred either to the tool or to the chip. Therefore, low values are desired for best thermal protections of the tool material whereas c-$Al_xCr_{1-x}N$ exhibits ~4 W/(m·K) at room temperature compared to ~6 W/(m·K) for TiAlN [51]. Thermal conductivity is a temperature dependent property and contrary to TiAlN the values for $Al_xCr_{1-x}N$ are decreasing above 250 °C [51].

Properties of importance for other fields of application (e.g. semiconductor industry) are mentioned here as well. The electrical surface resistance increases with Al-content from ~5 Ω·cm ($Al_{0.30}Cr_{0.70}N$) to ~200 Ω·cm ($Al_{0.60}Cr_{0.40}N$) [44,74] and shows also a dependence on the temperature with negative coefficient of resistivity [74]. Obtained values for single-crystal c-$Al_{0.68}Cr_{0.32}N$ on MgO(001) are ~2.7×10^3 Ω·cm (paper 3).
CrN was already applied as protective overcoat due to its very good chemical resistance which could even be improved by $Al_xCr_{1-x}N$ [65]. Additionally, investigations on arc evaporated coatings showed no influence of their deposition-typical droplets on the current density curve measurements [41].

3 Deposition technology

Production of covers, overcoats, films, or in general thin layers can be considered as a quite old idea due its usage already by ancient civilizations for decorative purposes. The field of applications of various coated products has developed significantly. Processes for the fabrication of thin films can be divided into wet and dry. Used techniques for this work are exclusively dry processes, why wet ones (i.e. electro planting, electro less plating, sol-gel deposition, anodic oxidation) as well as classic surface modification techniques (i.e. nitration, blasting, surface hardening, ion implantation) are not explained here. Also dry processes have sub-categories where the focus here lies on Physical Vapor Deposition (PVD). There a solid target material gets evaporated and condensed at the substrate. Descriptions of other techniques, like Chemical Vapor Deposition (CVD), their specific characteristics, modifications or their apparatus designs can be found in textbooks [104-109]. The PVD techniques used in this work are Unbalanced Magnetron Sputtering (UBMS) and arc evaporation (AE) both in the reactive mode. In the used form these are plasma assisted methods operating in vacuum conditions. This chapter summarizes the most important aspects of these two techniques, where more in depth explanations can be found in textbooks and scientific articles [104-109].

3.1 Sputter deposition

Sputtering is based on the interaction of energetic particles with solid matter. This material which contributes to the film forming process is called target. The transfer of the target species to the vapor state is different for several deposition techniques. In the case of non-reactive sputtering, the evacuated deposition chamber is backfilled with a noble gas (typically Ar) to a pressure of 0.1-1 Pa (0.75-7.5 mTorr) [107]. By applying a negative voltage to the target (-1 to - -5 kV), the electrons in the gas are affected by the electric field and get repelled. These electrons can cause ionization of the gas which occurs with a probability related to the scattering cross-section. Such positively charged ions on the other

hand are accelerated towards the target where they can get reflected as ions or neutrals, get implanted, or initiate a collision cascade with momentum transfer to the atoms in the target material. If the energy of the backscattered atoms in the target material is higher than the surface binding energy they can be ejected. The quantity of this effect is influenced by the energy of the impinging particles, the sputter yield of the target material, and the resulting mass ratio to the working gas. The resulting particles are mainly neutrals, ~1% negative ions, and ~10^{-3}% positive ions for sputtering [108].

As a result of the ion bombardment of the target there is also the generation of secondary electrons which contribute to the ionization process of the gas and therefore help sustaining the plasma. The electrons also excite the noble gas whereas the relaxation results in the generation of photons which can be seen in the characteristic glow of the plasma. An arrangement like this with the substrates or the chamber wall acting as anode is called DC diode system. This technique can only be used for conducting target materials; for isolators (i.e. oxides) the target can be operated under alternating current at high frequencies of 2 to 30 MHz (radio frequency - RF) [108].

The diode arrangement results in rather low deposition rates which was subject of several developments over the years. Goal is an increased number of electrons which can contribute to the ionization process. One approach is the combination of the described electric field with a magnetic field generated by magnets placed behind the target. Such a construction is called magnetron and the technique is called magnetron sputtering. Die to the fields the electrons get trapped close above the target where they travel on a circular orbit along the field lines. This longer way results in a higher probability of ionization events followed by more ejected particles from the target. As also excess heat in the target material is generated, the magnetron is water cooled to protect magnets and prevent the target from melting. Due to the trapping of the electrons in the vicinity of the target at the so called balanced magnetrons, there is no substantial heating of the substrates or generation of plasma at their vicinity. The latter effects are sometimes beneficial for the coating development. Additional bombardment of the growing film may be desired, why also arrangements are available where the magnetic field lines extend towards the substrates. Such a form is called unbalanced magnetron and was used in this work.

Magnetron sputtering can also be conducted in reactive atmospheres instead of pure noble gases. In this case the sputtering gas is simultaneously also a film forming species. Unfortunately this film also forms on the target causing an effect called target poisoning where the sputtering conditions change depending on the coverage of the target with the sometimes non-conductive film. This effect can be controlled by the partial pressure of the reactive gas, whereas the resulting working point is defined by requirements like high deposition rate and right stoichiometry of the produced film.

Fig. 3.1 shows the used high-vacuum laboratory deposition system located at Linköping University. It is equipped with two planar unbalanced magnetrons which are tilted by 25° from the substrate normal as can be seen in Fig. 3.1a. For the depositions in this work one magnetron mounted with a Ø 75 mm Al/Cr compound target was used.

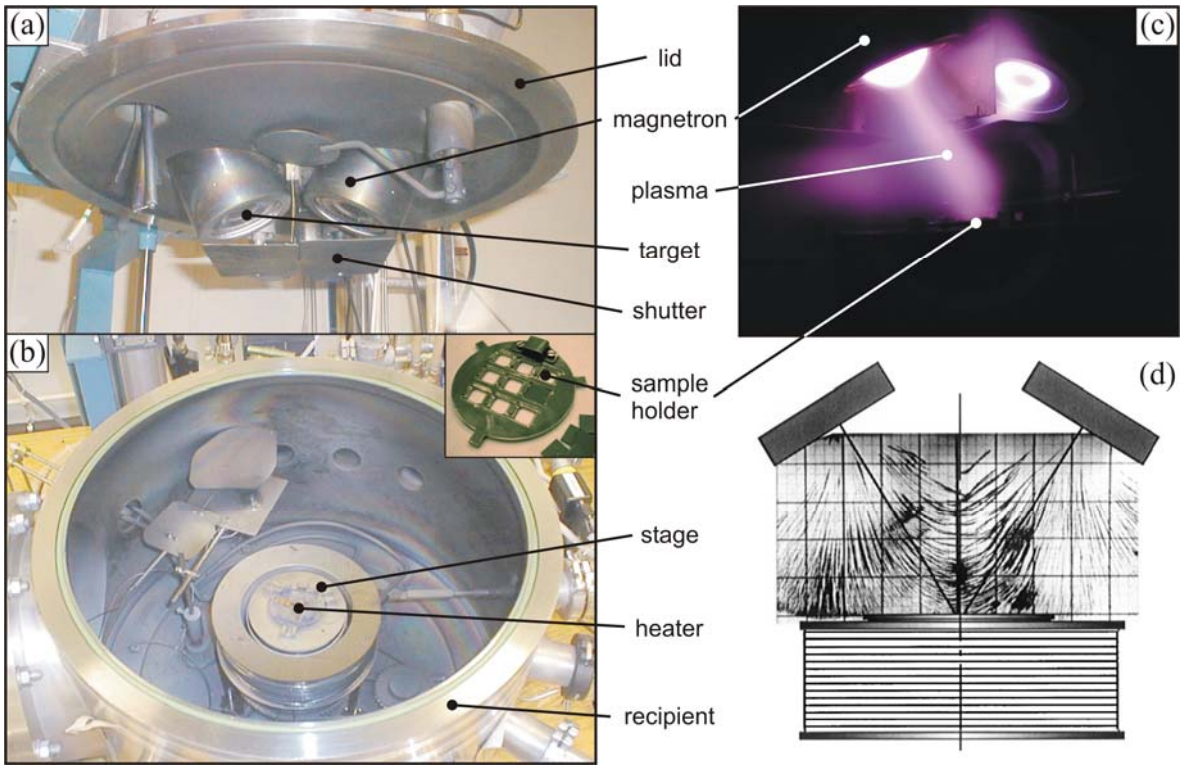

Fig. 3.1. High-vacuum deposition system (ADAM) with the shutter protected dual magnetron system in the lid (a) and the sample holder stage with heater and sample holder in the recipient (b). (c) Nitrogen plasma extending towards the substrates along the magnetic field lines like illustrated in (d) visualized by iron powder [110].

Fig. 3.1b shows the setup of the rotatable sample stage with heater and the corresponding sample holder. The base pressure of the chamber was 2.67×10^{-4} Pa (2×10^{-6} Torr) while sputtering was carried out in pure N_2 (99.999 %) at a pressure of 0.4 Pa (3×10^{-3} Torr) resulting in a plasma similar to the one seen in Fig. 3.1c. Here also the second target is in operation shielded by a shutter. There, the higher plasma density close to the target in the typical donut like shape as a result of magnet configuration can be seen. This figure also shows the effect of the extending magnetic field lines guiding the plasma to the substrates. This is also illustrated by Fig. 3.1d where the field lines were made visible by iron powder [110]. To support film growth, a negative substrate bias of -40 V was applied to attract ions close to the substrates and enhance the ad-atom mobility of the film forming species.

3.2 Arc evaporation

Several forms of evaporation techniques are available today where they mainly differ by the used physical effect for evaporation. This can be done by simple thermal heating, laser, electron beam, or as used for paper 1 and 2, by a low voltage (10-100 V) high current (up to 1000 A) arc discharge between two electrodes. Typically the cathode, which gets evaporated, is made of the target material why this technique is also called cathodic arc evaporation. A detailed historic review of arc plasma science is given by Anders [111,112]. Like sputtering, this is a vacuum technique which can be operated in reactive or non-reactive mode. The difference to magnetron sputtering is the extremely high ionization rate of the film forming species which is due to the given form of evaporation. The initiated arc results in a very high surface temperature of the target in the arc spot (with a typical dimension of 1-10 µm [108], which results in a very localized melting of the material. From this area strong particle and electron emission occurs [108] where especially the lighter electrons get accelerated in the electric field close to the target [113]. By collisions with the metal vapor atoms, the plasma gets highly ionized which can reach 100% for high melting metals [108]. These ions also exhibit very high energies of 50-150 eV. The arc, however, moves over the target randomly (random arc) with the risk of staying too long on the same spot resulting in the ejection of liquid metal drops with 0.1-5 µm diameter from

the cathode surface [104]. There are different hypothesis how these macroparticles (droplets) are formed exactly [104,108,113], however, it is proven that the angular distribution of the emerging droplets is inhomogeneous with a peak emission of ~20° to the target surface [113]. The influence of droplets on the developed film microstructure is displayed in Fig. 3.2a which shows a cross-sectional transmission electron micrograph of an $Al_{0.20}Cr_{0.80}N$ hard coating deposited under conditions far off the optimum working point. In general the droplets are in a solid state when they arrive at the substrate, offering a new curved growth surface (Fig. 3.2b). Due to the shadowing of the incoming particles by the droplet, large voids are formed behind it (Fig. 3.2c) which can act as a weak spot in the film under mechanical or tribological loads. The droplet as well as the cone shaped film material grown on top of it can quarry out and leave big holes. But also with the resulting growth artifacts, the surface roughness increases which can be seen schematically in Fig. 3.2c and in real dimensions by a fracture cross-sectional scanning electron micrograph in Fig. 3.2d.

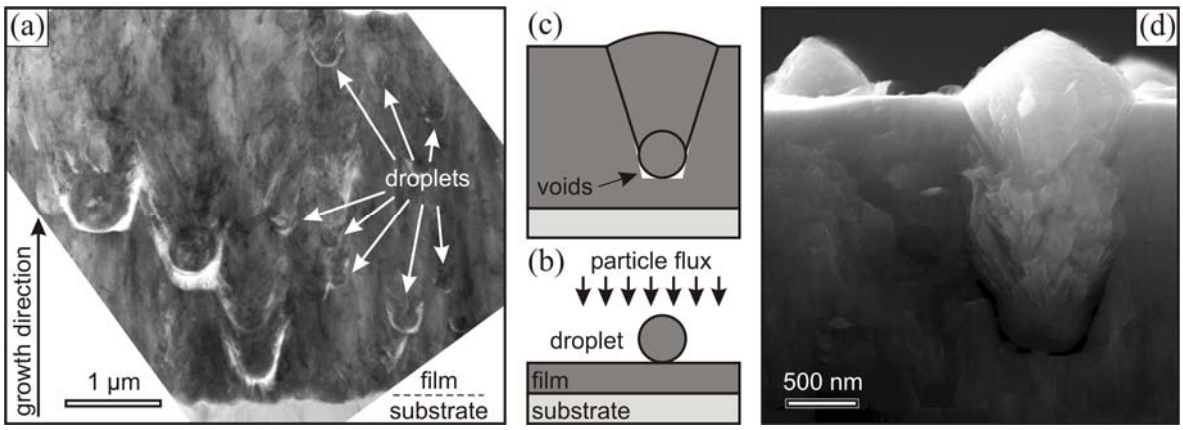

Fig. 3.2. a) Cross-sectional TEM micrograph of an $Al_{0.20}Cr_{0.80}N$ film with a high number of droplets due to bad deposition conditions. b) and c) show schematically the influence of droplets on the film microstructure. d) Resulting surface roughness of the growth artifacts in a fracture cross-sectional scanning electron micrograph.

Nevertheless, the high degree of ionization is beneficial for production of good adherent and dense films which makes arc evaporation successful for the production of protective hard coatings. However, droplets with their resulting growth defects make this technique less suitable for applications where a smooth surface is required (i.e. optical and magnetic purposes). Therefore, the goal is a reduction of macroparticles in the film or even

to avoid them. Generally, droplet formation is dependent on the melting point of the target material, the geometry of the cathode, their surface morphology, as well as the arc current [108]. For most applications the target material and form can not be changed and also a change in deposition parameters my have undesired effects (i.e. lower deposition rate). Another option is steering the discharge over the target surface by a movable magnetic field in the back of the cathode. This should be done in a form that the material has the chance to cool down before the arc spot comes again to the same place (steered arc). Another approach to reduce the local current density is splitting up of the arc. The maximum current density for a given cathode is limited. By reaching this level the arc starts to split, but this would require an increase in total arc current. Alternatively an array of several small magnets in the back of the cathode can be used which results in a disperse arc formation leading to a better cathode exploitation. If the application requires a droplet free film, there is also the opportunity of filtering with a magnetic field, where the ionized plasma gets directed to the substrates which are not located in front of the cathode (typically 90°). Thereby, neutral particles and droplets are not contributing to the film growth causing a reduction of the deposition rate.

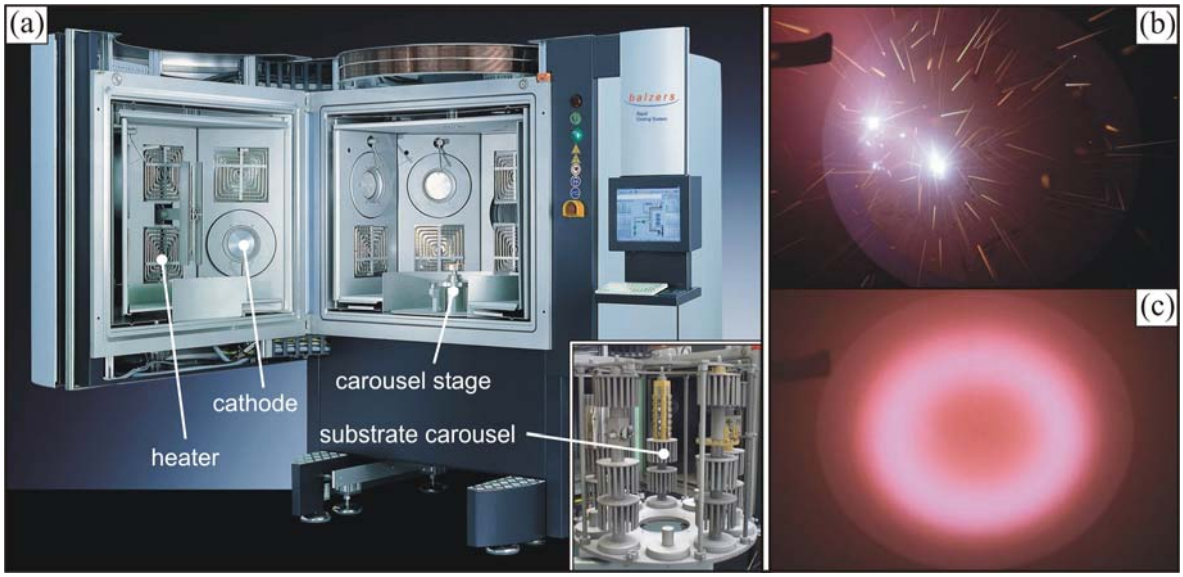

Fig. 3.3. a) Oerlikon Balzers Rapid Coating System (RCS) with mounted substrates on carousel (insert). b) Undesired and c) optimized arc formation during deposition in nitrogen.

In this work an Oerlikon Balzers industrial arc evaporation system (RCS - Rapid Coating system) was used for paper 1 and 2 (Fig. 3.3), equipped with four Al/Cr compound cathodes operated with 140 A each. Depositions were performed in pure nitrogen and the substrates were mounted on a two-fold planetary rotating substrate carousel (insert Fig. 3.3a). Fig. 3.3b shows an undesired form of an arc discharge where two arcs are burning on a spot resulting in a large amount of droplet formation emerging in all directions from the target. Contrary, Fig. 3.3c shows a standard arc discharge how it was observed for the depositions of this work where a cathode specific array of permanent magnets results in this fine-dispersed extremely fast moving arcs.

4 Thin film microstructure

In the previous chapter different deposition techniques were mentioned, focusing on the equipment characteristics and the corresponding ways how the vapor of film forming species is produced. This chapter describes the formation of the film from the generated vapor. The influence of several deposition parameters on the film's microstructural development is discussed and also basics on x-ray diffraction and transmission electron microscopy, two techniques used for microstructural analysis in this work, are presented.

Film formation in general occurs by condensation of the film forming species at the solid substrate. Additionally there are several more possible interactions, dependent on the kind of involved particles, their energy, and the type of substrate, summarized in Fig. 4.1a. The impinging particles exhibit an energy distribution due to the used deposition technique and the applied deposition parameters. Depending on this energy and the place of impact, several lattice defects can be caused by knock-on processes (Fig. 4.1b).

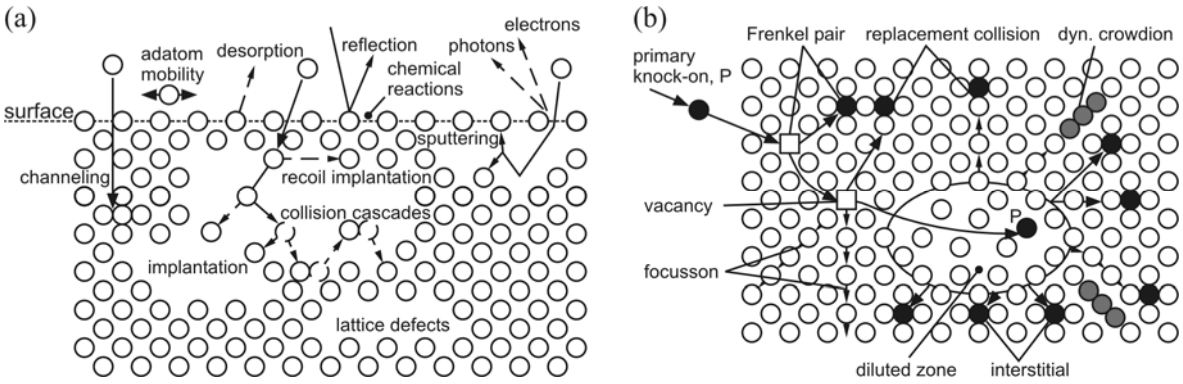

Fig. 4.1. (a) Schematic illustration of possible interactions between impinging particles and substrate during deposition and (b) possible resulting lattice defects due to knock-on processes of energetic atoms [114] (based on [115-117])

Particles impinging on the substrate can immediately re-evaporate or adsorb and diffuse on the substrate. Even desorption is possible if they gain enough thermal energy. The fraction of adsorbed particles which are incorporated in the film out of the total flux is called sticking coefficient. Surface diffusion of these atoms on the substrate surface is influenced by the temperature and crystallographic type of the surface as well as the kind of the

diffusing species and the bonding state (physisorbed or chemisorbed). Considering more than one randomly diffusing atom opens the field of nucleation and growth processes. Heterogeneous nucleation on a solid surface out of a vapor phase can be described by the heterogeneous capillary model of nucleation. When diffusing particles encounter each other they may form a cluster which becomes stable if it reaches a critical size, illustrated in Fig. 4.2a. The model takes the surface energies of the free substrate surface ($\gamma_{S\text{-}V}$), the film/substrate interface ($\gamma_{S\text{-}F}$), and the film surface to the vapor ($\gamma_{F\text{-}V}$) into account. The resulting contact angle α indicates the potential of the nucleus to cover the substrate, schematically shown in Fig. 4.2b, and is called wetting. More detailed description of the nucleation and growth processes can be found in literature [104,118,119].

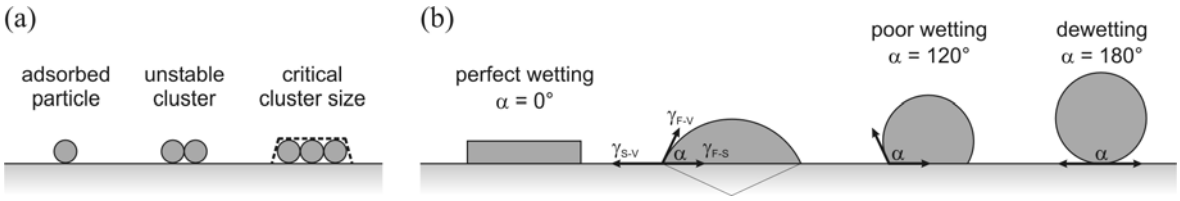

Fig. 4.2. (a) Schematic of the atomistic nucleation process and (b) different wetting conditions of the film developed on the substrate (after [120] and [121]).

4.1 Growth mechanisms

The growth of thin films is, amongst others, defined by the initial nucleation layer. A wetting angle $\alpha > 0°$ means that the particles forming the nucleus have a stronger tendency to stick together than to the substrate which results in a pile up as seen in Fig. 4.2b. With the continuous supply of particles to the nuclei during growth and the existence of a nucleation barrier the nuclei may develop to three-dimensional islands. Such a growth mode is therefore called island growth or Volmer-Weber growth and is schematically illustrated in Fig. 4.3a. For a wetting angle of 0° the energetic calculations show that neither nucleation barriers nor a critical nucleation size exist [104,118]. The preferred place for particles is the surface which will be fully covered before a next monolayer will be started. This form is called layer-by-layer growth or Frank-van der Merve growth, presented in Fig. 4.3b. However, the nucleation phenomena are influenced by several more

parameters which can change during deposition, i.e. impurities, energy distribution of impinging ions, different surface temperature, or stress/strain state with film thickness. Such variations can result in a change of the growth mode from layer-by-layer to island mode if the corresponding energetic requirements are fulfilled. This layer plus island growth is also called Stranski-Krastanov growth mode and is displayed in Fig. 4.3c. The switch in growth modes occurs after the substrate is already covered by some layers since the contributions for the energetic balance are different ones. The interface energy between the film and the substrate surface ($\gamma_{S\text{-}F}$) has to be substituted by an interfacial energy considering interactions between the nuclei and the already grown film whereas contributions of $\gamma_{S\text{-}V}$ totally vanish. Driving force for all growth modes is the minimization of the total surface energy. More detailed descriptions and mathematical explanations on the background of the growth modes can be found in literature [104,117-119,122,123]

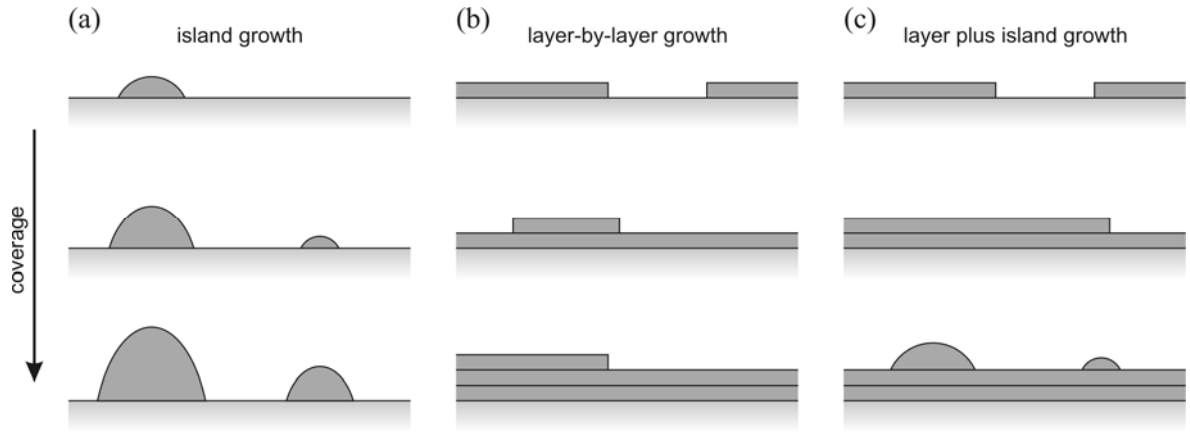

Fig. 4.3. Nucleation and growth controlled by surface and interface energies. (a) Island mode (Volmer-Weber), (b) layer-by-layer growth (Frank-van der Merve), and (c) layer plus island growth (Stranski-Krastanov).

4.1.1 Epitaxial growth

Epitaxy describes a special form of growth with a defined crystallographic relationship between the growing single-crystal film and the crystalline substrate. The root of the term is Greek consisting out of the words *epi* (placed or resting upon) and *taxis* (arrangement). Epitaxial growth can be divided into homoepitaxy, where the film forming particles and the substrate are the same material (i.e. Si on Si-wafers), and heteroepitaxy, where the film forming elements are not necessarily related to the substrate material (i.e. c-$Al_xCr_{1-x}N$ on MgO like in this work) [122]. For homoepitaxy, the growth conditions are optimum in respect of identical material, crystallographic structure, and lattice parameter of film and substrate. This is not valid for heteroepitaxy, however, even films with different crystallographic structure as the substrate were successfully grown (i.e. Cr on MgO) [124]. Such combinations become possible when the lattice spacing in a given set of planes fits on the substrate like for Cr on MgO with $a_{MgO} \sim \sqrt{2} \cdot a_{Cr}$ resulting in a crystallographic relation of $(001)_{Cr}||(001)_{MgO}$ and $[110]_{Cr}||[100]_{MgO}$. In most applications film and substrate have the same crystallographic structure, like in this work. The growth of c-$Al_xCr_{1-x}N$ on MgO results in a so called cube-on-cube relation with $(001)_{AlCrN}||(001)_{MgO}$ and $[100]_{AlCrN}||[100]_{MgO}$ (paper 3 and paper 4). Dependent on the difference in lattice parameter, the character of the resulting interface can change, which is caused by the ability of the lattice to adjust for small misfits. Strain fields can change physical properties of materials being especially undesirable in the semiconductor industry which uses epitaxial growth extensively. For some applications and material combinations it is possible to overcome these problems by using alloying elements to adjust the lattice parameter of the film to the substrate [125]. A schematic illustration of such a lattice-matched system is given in Fig. 4.4a. As a comparison Fig. 4.4b shows a film-substrate combination with $a_{film} < a_{substrate}$ where the mismatch is completely compensated elastically by the film lattice. In this so called pseudomorphic strained film, the lattice adjusts in-plane ($a_{||}$) elastically to the larger substrate resulting in a reduced lattice parameter in growth direction ($a_{\perp}$). Interfacial elastic energy can also be relaxed by misfit dislocations as illustrated in Fig. 4.4c. Dependent if $a_{film} < a_{substrate}$ or $a_{film} > a_{substrate}$ a lattice half-plane is inserted or missing during the growth process, respectively. With increasing density of

misfit dislocation, the film becomes more and more relaxed until fully relaxed growth of the film is obtained where the film grows with its bulk lattice parameter a_f. It should be noted here that this considers not the microscopic strain fields which are present around the dislocations.

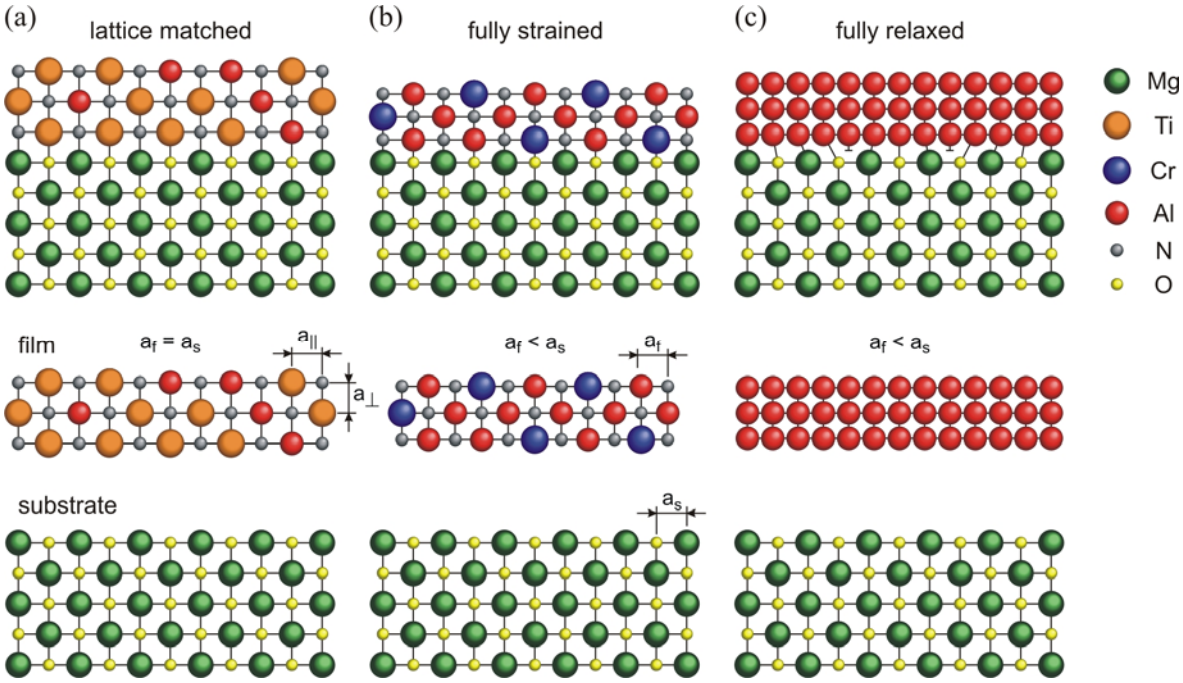

Fig. 4.4. Schematic overview of the strain states in heteroepitaxially grown cubic layers. (a) Lattice matched $Ti_{1-x}Al_xN$ layer on MgO, Al-content adjusted for matching film and substrate lattice parameters ($a_f = a_s$). (b) $Al_xCr_{1-x}N$ film with $a_f < a_s$ where the film is elastically adjusted to the in plane lattice parameter ($a_{||}$) of the substrate resulting in a reduction of the out-of-plane lattice parameter ($a_\perp$). (c) Fully relaxed growth of the layer due to the insert of additional half planes (misfit dislocation) to adjust to the lattice mismatch ($a_f < a_s$).

4.1.2 Polycrystalline growth

If the substrate is amorphous, polycrystalline, or even a single-crystal with a too large lattice mismatch (as a rule of thumb >9% [122]), epitaxial single-crystal growth can not be achieved. However, for most cases and material combinations this is the rule instead of the exception and results in nucleation and growth of different oriented grains. Growth of the nuclei can proceed via incorporation of atoms directly from the deposition flux or of

diffusing ad-atoms at the surface. Also coalescence of two growing nuclei and coarsening (Ostwald ripening), with a net material transport from the smaller to the bigger islands, occur [104,118,126-128]. These can lead to a restructuring of the resulting grains due to the interactions of the growing islands/grains [129]. Two impinged neighboring islands are normally separated by a grain boundary which can migrate if the mobility is sufficient. This means that some atoms detach from one grain and become part of the other grain with a resulting movement of the grain boundary [120]. Contrary to the epitaxial growth which normally proceeds via a layer-by-layer growth mode, polycrystalline materials can undergo a competitive selection where crystals in preferred growth orientation overgrow slower growing ones. The developed microstructure, however, is a function of a variety of parameters where next to the chosen substrate and film material the used deposition parameters have a strong influence.

Described film forming processes like nucleation, growth, and restructuring are strongly dependent on the diffusivity/mobility of the atoms during growth. These properties scale with the melting temperature (T_m) of the deposited material [122,130] resulting in different microstructures dependent on the deposition temperature (T_s). Movchan and Demchishin distinguished between three different characteristic structural zones which are summarized in a structure zone model (SZM) [131]. In literature this is also called basic structure zone model (BSZM) because it just considers the homologous temperature (T_s/T_m) as a variable for the developed microstructure. Thornton, who used sputtering instead of evaporation as Movchan and Demchishin, added the gas pressure as a second variable [132]. He also observed an additional structural zone between 1 and 2 which he called transition zone (zone T). Over the years several authors worked on the further development of SZMs and contributed to a detailed understanding of the underlying processes [126-128,133-141]. The terminology introduced by Movchan and Demchishin [131] (zone 1, 2, and 3) and Thornton [132] (zone T) can be found in almost all of them, however not used consistently. A comparison of different SZMs and detailed explanations can be found in literature [104-106,109,116,118,120,136,137]. Here just a short description of the individual zones and the underlying physical processes is given.

To draw an exact border between the different zones is difficult. One way for a definition can be made by the predominant form of diffusion during growth. In zone 1 the

homologous temperature is low why the ad-atom mobility is very limited. This can result in a hit-and-stick growth where the only parameter affecting the film growth is the incoming direction of the particle flux, why it is also called 'ballistic' deposition. A voided columnar structure, due to shadowing effects [104], with amorphous-like or small equiaxed grains and no preferred out-of-plane orientation is the result [136]. Bombardment of particles with higher kinetic energy during growth can result in knock-on processes resulting in increased film density due to filling of the voids. Another way of activating the ad-atom mobility is an increase in thermal energy (higher T_s/T_m). When diffusion on grain surfaces is possible but impossible from one grain to another one, the resulting microstructure consists of faceted columns separated by grain boundaries. The voids are filled due to the higher ad-atom mobility. Also in this case no preferential out-of-plane orientation is developed because the particles can not diffuse to another grain so the only competition between the columns is still shadowing (bigger columns can overgrow smaller ones). As already mentioned the notation and classification of the different zones varies between the authors. This description is based on the scheme of Mahieu [136] who also offers a comparison between the various works available in literature.

At higher T_s/T_m the mobility of the ad-atoms increases and they can diffuse also to other grains now. Such activation can additionally be achieved by other energy enhancing processes (i.e. substrate bias). The resulting microstructure is called transition zone or zone T with typically cone-shaped and faceted columns [142]. This is due to randomly oriented nuclei in combination with anisotropic growth rates of the crystals [104,142]. Therefore preferred oriented crystals can overgrow less preferred ones resulting in a competitive growth mode and a preferred out-of-plane orientation according to the fastest growing crystallographic direction.

For zone 2 development, the temperatures are high enough to promote restructuring of nuclei and island during growth via ripening or grain boundary migration. Driving force is the surface and interface energy difference between neighboring crystal faces due to their orientation relationship [142]. This results in a straight columnar structure with a preferred orientation perpendicular to the plane of the lowest surface energy.

Further increase in temperature will lead to even wider columns in zone 2 films until T_s/T_m is high enough that bulk diffusion is allowed. In this state, grains in the structure of

the film can nucleate, grow, and shrink during and even after deposition. As a result the columnar structure is substituted by large crystalline grains in zone 3. However, this zone is not observed in material systems where processes which stop grain boundary migration are active.

A schematic summary of the different zones is given in Fig. 4.5. The exploded illustration shows the result of the single processes like shadowing, surface diffusion, and bulk diffusion and combines them in an overlay in the bottom of the figure resulting in the SZM of Thornton [134]. The increased range of existence of zone 1 at higher gas pressures can be explained by more scattering events of the particles before impinging with the result of a reduction in bombardment energy and a higher angular spread of the incoming material flux.

Several authors considered additional effects during growth or influences on the microstructure and made important extensions to the SZM, where some of them are summarized in Fig. 4.6. Hentzell et al. discussed the process of granular epitaxy during grain growth of vapor-deposited films resulting in a bimodal grain structure in zone T (Fig. 4.6a) [139]. Messier et al. separated the effects of thermal- and bombardment (applied bias voltage) induced mobility (Fig. 4.6b) [138]. In this model zone T extends to lower T_s/T_m values with higher applied bias voltage (V_S) due to the additional energy input by the energetic particle bombardment. Barna and Adamik investigated the influence of impurities on the developed microstructure starting from an ideal SZM (Fig. 4.6c) [142]. This is of tremendous importance because the deposition of pure films is rarely possible in industrial processes. The source of impurities can be the remaining atmosphere, insufficiently cleaning of substrates prior to the deposition, bad process gas quality, or imperfect deposition materials. More importantly, this model is also valid for intentionally introduced alloying or dopant elements like co-deposited additives in multicomponent films.

The impurities can influence the resulting growth in several ways. If such a particle gets adsorbed at the growth surface it can influence the ad-atom mobility or form compounds with the metallic species and change the basic film forming processes (i.e. nucleation). If the density of 'impurities' is high enough they can even form their own phase resulting in changed surface conditions for the impinging and diffusing film forming

species. One of the most important effects at high temperatures is the ability of the impurities to change the mobility of grain boundaries which can be seen in Fig. 4.6c by the fine grained microstructure at high impurity levels.

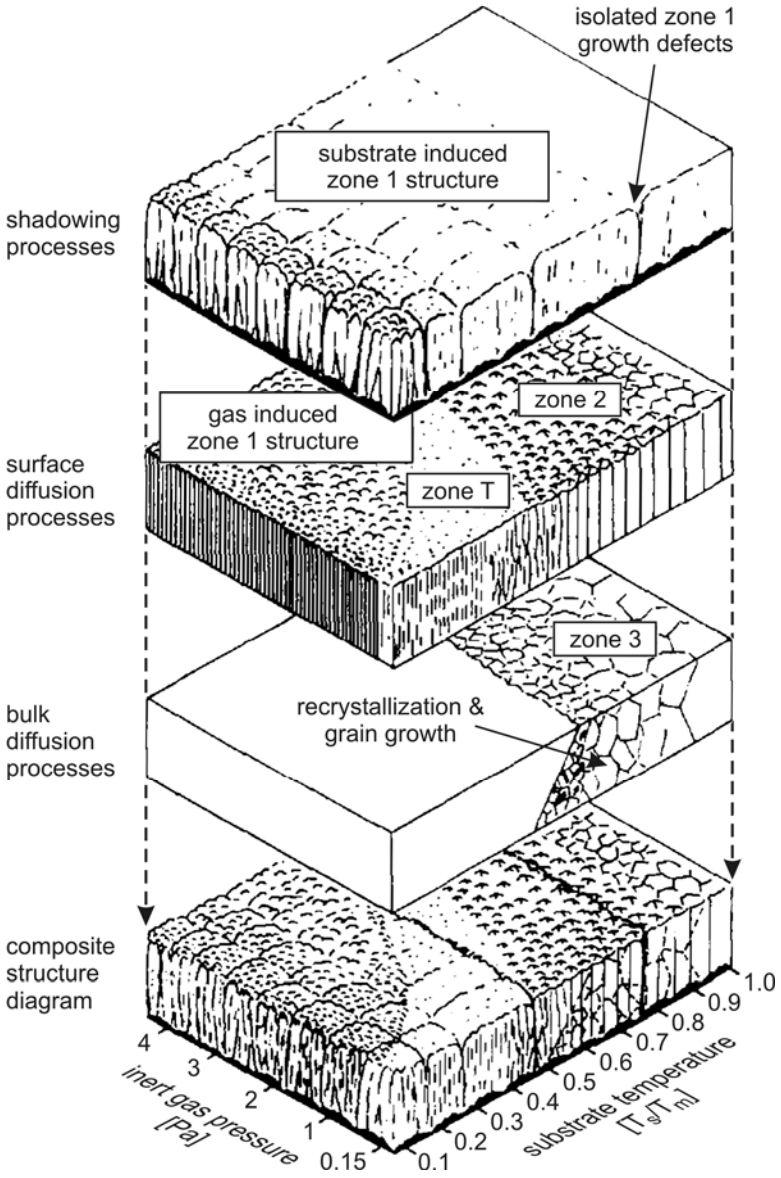

Fig. 4.5. Exploded view of the physical processes underlying the Thornton structure zone model consisting of the zones 1,T,2, and 3 (modified [122,134]).

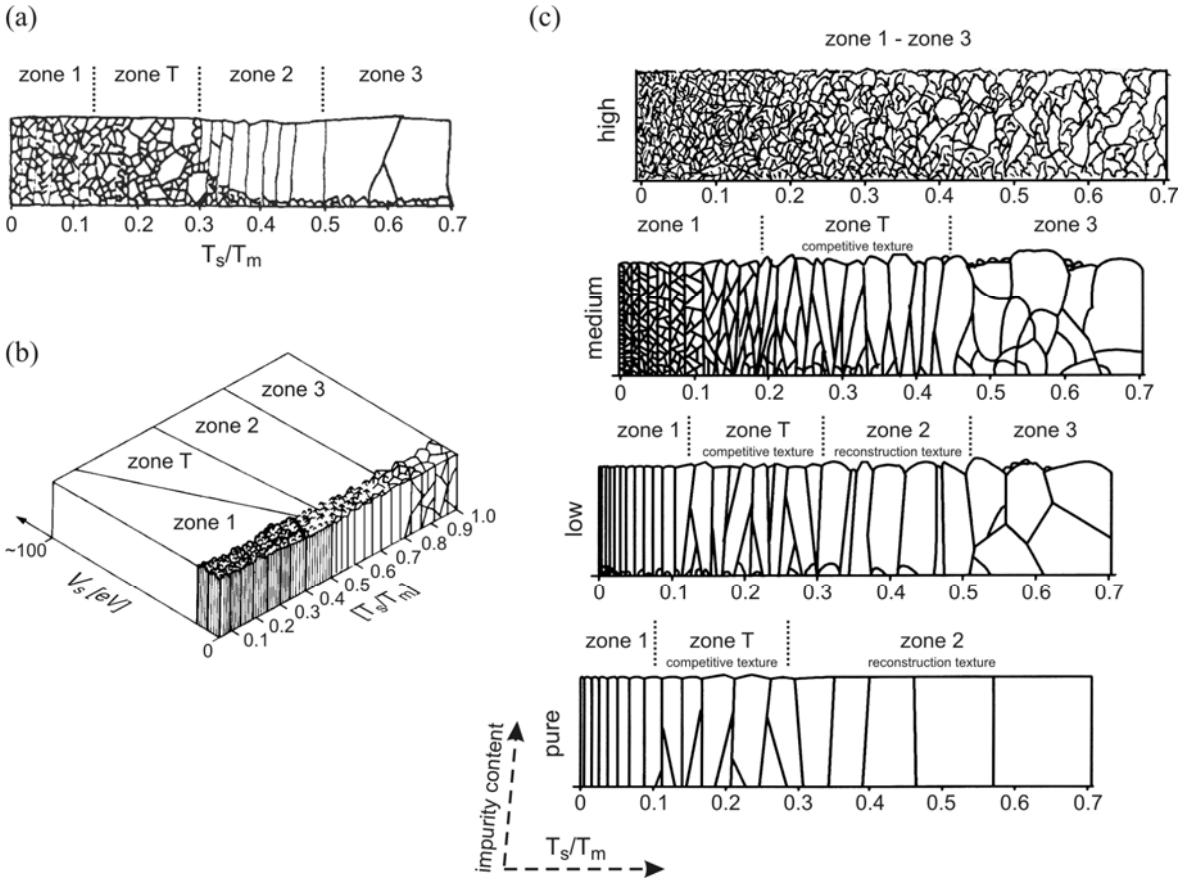

Fig. 4.6. Structure zone model of (a) Hentzell including the bimodal grain size distribution in zone T, (b) Messier showing the effect of ion bombardment, and (c) Barna and Adamik considering impurity concentrations during growth.

4.2 Structural characterization

Differences in the developed microstructure of deposited films result in significant changes of the corresponding properties. Not just obvious effects like the film density but also grain size, form, and orientation in dense films have a strong influence on properties like hardness. For coating/thin film development and optimization of deposition parameters, a detailed knowledge of the microstructure is necessary. Considering modern coating materials consisting out of several elements, also the question of developed phases must be addressed. In this work the focus is on single-phase solid solution films with chemical compositions close to a phase transition. Therefore, the criterion of a single-phase material must be ensured before further tests (i.e. on thermal stability) are conducted.

Finally, also potential changes in the microstructure due to mechanical, chemical, or thermal load must be characterized to improve the produced material.

Due to the small lateral dimensions of the film structures, a characterization with the bare eye or an optical microscope can just give limited or indirect information of the predominant structure and phases (film roughness/glance, color). More information can be obtained by using probing media with a resulting wavelength smaller than visible light. X-ray diffraction (XRD) and transmission electron microscopy, two techniques used for characterization in this work, are described in the following section.

4.2.1 X-ray diffraction (XRD)

This non-destructive structural characterization technique is based on the principle of scattering which becomes possible due to the fact that the wavelength of x-rays is in the order of the atomic distances of the investigated material. Electromagnetic radiation with these requirements (like x-rays) can undergo diffraction with constructive and destructive interference on periodic structures in the materials (i.e. lattice planes). In case a material can be described by the crystal structure and the lattice spacings, this provides the possibility of phase determination. X-ray diffraction, however, can also be used to obtain structural properties such as grain size, texture, epitaxial relations, or residual stress in the film. The requirements for constructive interference were mathematically formulated by W.H. Bragg and W.L. Bragg in their famous Bragg's law [143] which can be found, including a schematic visualization, in Fig. 4.7. Constructive interference is observed when the path difference $2 \cdot \Delta$ is an integral number (n) of the wavelength λ of the traveling x-rays. With the geometrical correlation $\Delta = d \cdot \sin\theta$, the final form of Bragg's law is derived. There, θ is the angle of the incoming x-rays and d (or d_{hkl}) the lattice plane spacing which can be derived for the different Miller indices (hkl) and the dimensions of the unit cell. Equations for cubic and hexagonal crystals are also given in Fig. 4.7.

However, the diffracted intensity depends on several parameters like atomic form factor, structure factor, and absorption factor. Detailed descriptions and explanations of these influences and analysis by x-rays in general can be found in literature [144,145].

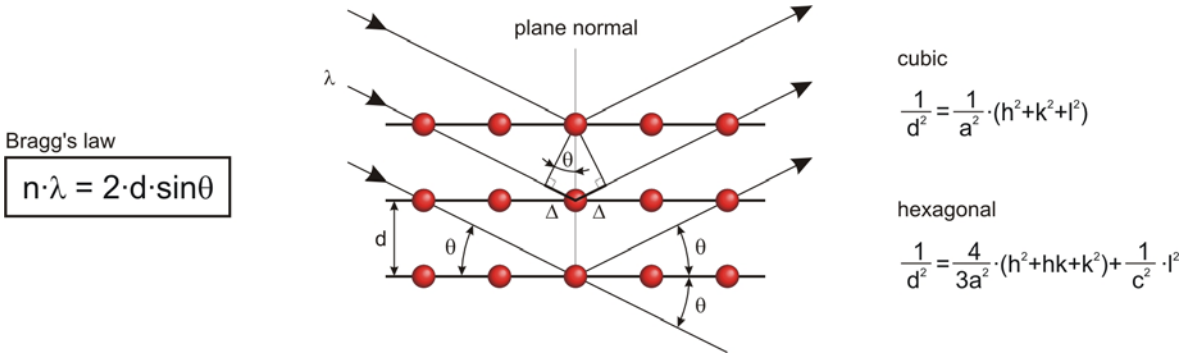

Fig. 4.7. Bragg's law of x-ray diffraction with a schematic graphical interpretation and mathematical correlation between lattice plane spacing of given Miller indices and the unit cell dimensions for cubic and hexagonal crystals.

4.2.1.1 Reciprocal lattice

The explanation of Bragg's law in the previous chapter was based on geometrical relations in real space. Explanations for several problems or measurement techniques become simpler in a construct called reciprocal lattice. Therefore, a few basics will be described here. A crystallographic lattice (in real space) is constructed of a periodic arrangement of unit cells which can be described by a set of independent basis vectors ($\mathbf{a}_1$, $\mathbf{a}_2$, and $\mathbf{a}_3$). The three primitive vectors of the corresponding reciprocal lattice can be calculated to be $\mathbf{b}_1 = V^{-1}(\mathbf{a}_2 \times \mathbf{a}_3)$, $\mathbf{b}_2 = V^{-1}(\mathbf{a}_3 \times \mathbf{a}_1)$, and $\mathbf{b}_3 = V^{-1}(\mathbf{a}_1 \times \mathbf{a}_2)$ with V being the volume of the crystal unit cell in real space. As a result these vectors have the dimension of inverse length why the space is called reciprocal space where small distances in real space become big and vice versa. Without going into detail and without mathematical derivations, which can be found in literature [144,145], some fundamental relations between real and reciprocal space are listed below

- Miller indices hkl ↔ coordinates of reciprocal lattice point G
- plane spacings d_{hkl} ↔ length of vector **G** from origin to G
- plane orientation (hkl-normal) ↔ direction of vector **G**
- Structure factor ↔ weight of reciprocal lattice point G.

Each crystallographic lattice structure has a corresponding reciprocal lattice which is illustrated in Fig. 4.8 by a face-centered cubic material and the corresponding body-centered cubic reciprocal lattice.

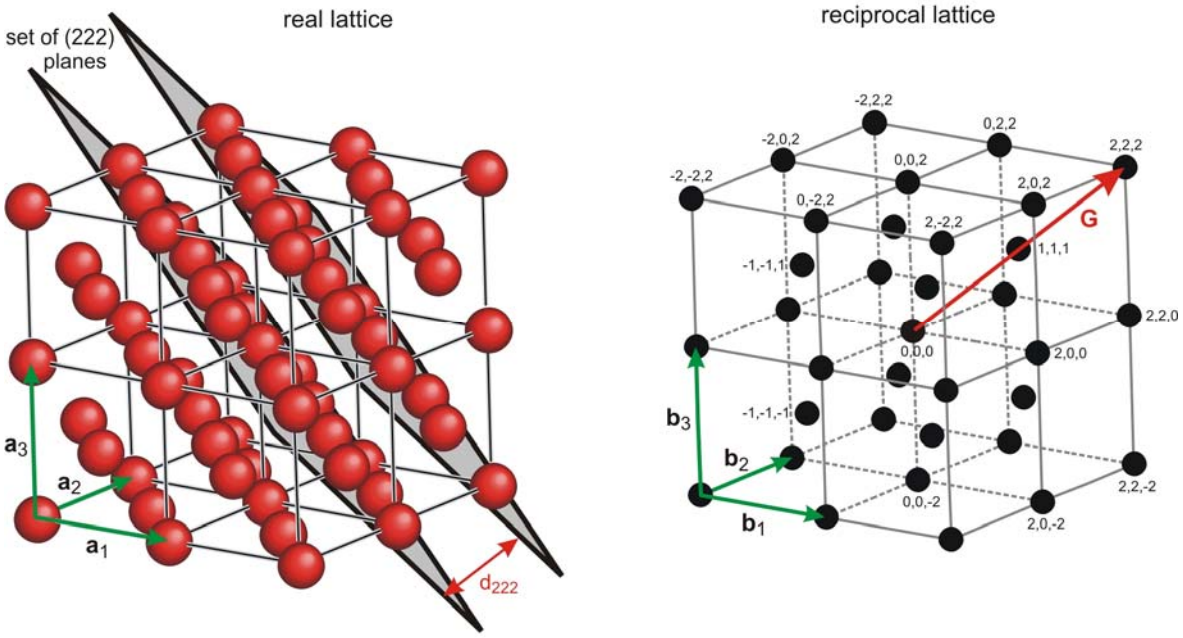

Fig. 4.8. Face-centered cubic structure with corresponding reciprocal lattice (body-centered cubic) containing the vector **G**, representing the plane spacing and orientation of the indicated set of (222) lattice planes.

Let's consider now a diffraction experiment with x-rays on a set of crystal planes (Fig. 4.9). The x-rays transform to wave vectors (**K**) in reciprocal space where the length of the vector is inverse proportional to the wavelength ($|\mathbf{K}| = 2\pi/\lambda$). Out of the incident ($\mathbf{K}_0$) and a diffracted wave vector (**K**) the scattering vector can be calculated to be $\mathbf{Q} = \mathbf{K}\text{-}\mathbf{K}_0$. Constructive interference (diffraction) occurs when this scattering vector hits a reciprocal lattice point. This is called the Laue condition and replaces the Bragg's law in reciprocal space. A sphere in reciprocal space with the radius $|\mathbf{K}_0|$ is called Ewald sphere and all possible scattering vectors start and end on this sphere. In laboratory equipments the wavelength of the x-rays is normally fixed by the material of the x-ray tube (Cu, Co, Cr, Mo), and therefore also the length of the incident wave vector is defined. In the measurements of this work Cu-K_α radiation with $\lambda = 1.54056$ Å was used.

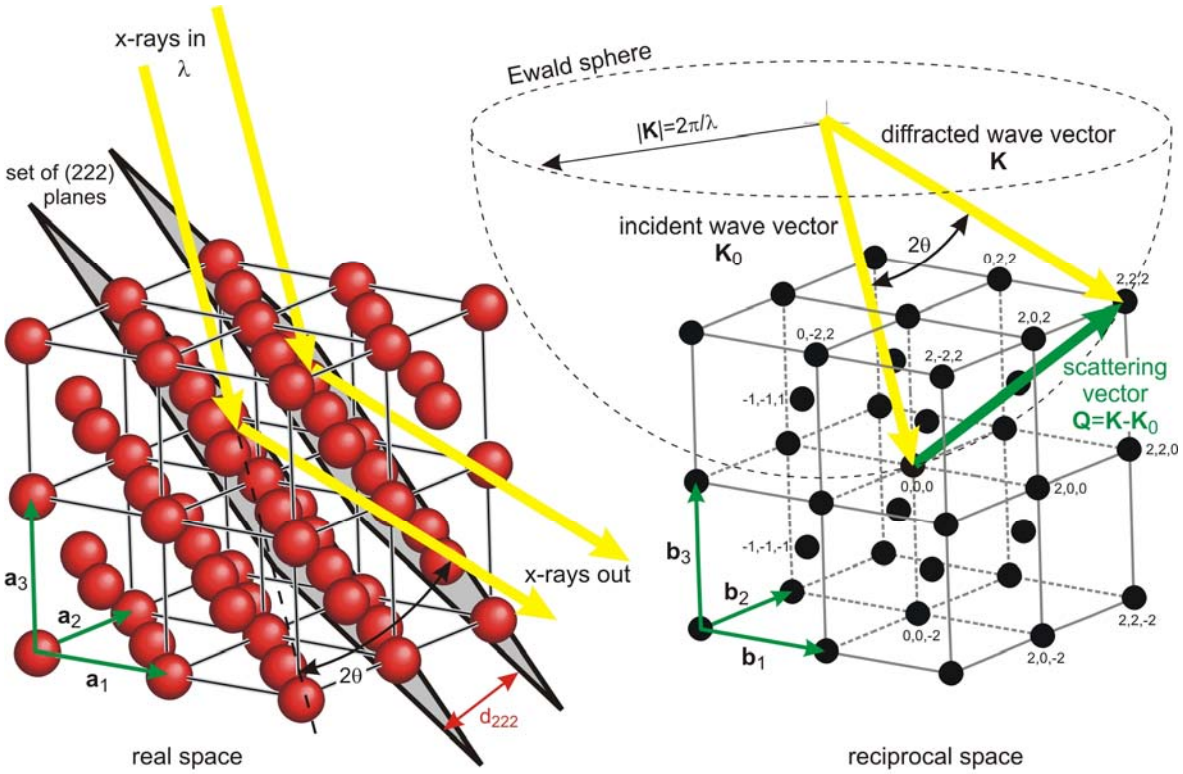

Fig. 4.9. Schematic illustration of diffraction on lattice planes in real space and the corresponding vectors in reciprocal space. To underline the geometrical relations one half of the Ewald sphere is included.

4.2.1.2 Measurement techniques

X-ray diffraction (XRD) measurements on laboratory scale equipments face geometrical limitations for the analyzable dimensions in reciprocal space as illustrated in Fig. 4.10a. The borders are defined by the length of the scattering vector (used x-ray radiation) and possible restrictions in the degrees of freedom of the goniometer. A two-dimensional cross-section of the reciprocal space including the three vectors $\mathbf{K}_0$, $\mathbf{K}$, and $\mathbf{Q}$ is called scattering plane and is shown for a rock salt single-crystal in Fig. 4.10b. Within the outer limits (large hemisphere) two areas can be distinguished, labeled with reflection and transmission. The reason therefore is based on the path which the incident ($\mathbf{K}_0$) and diffracted ($\mathbf{K}$) wave vectors have to take, in order that the scattering vector ($\mathbf{Q}$) reaches a certain point in reciprocal space. For the grey shaded areas in Fig. 4.10b either

$\mathbf{K}_0$ or $\mathbf{K}$ points through the sample why these refer to transition areas. Important for this work is the remaining reciprocal space which is accessible by reflection.

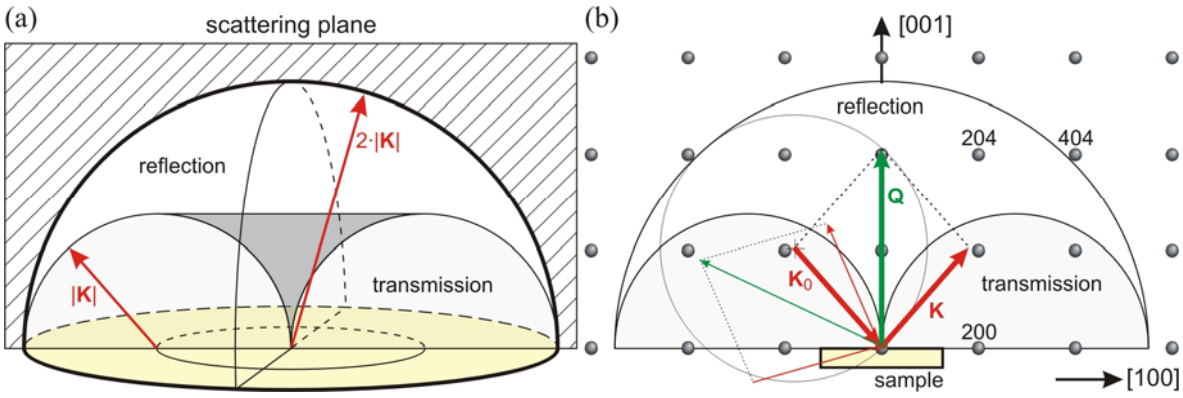

Fig. 4.10. (a) Three dimensional illustration of the accessible reciprocal space due to the fixed wavelength of the x-rays and geometrical restrictions of the measurement equipment. (b) Rock salt single-crystal in reciprocal space with examples for necessary configurations for accessing the area of reflection and transmission in the scattering plane.

XRD is a very versatile and powerful technique for material characterization and most of the measurements can be performed without recognizing any of the limitations. However the observed features in reciprocal space strongly depend on the investigated material. In this work single-crystalline and polycrystalline films were investigated why Fig. 4.11a compares rock salt materials (like c-$Al_xCr_{1-x}N$) differing just in this point. The single-crystal material shows a discrete spot pattern due to the well aligned lattice planes. Polycrystalline materials on the other hand consist of a huge number of randomly oriented small crystallites which all fulfill the diffraction conditions. Considering same sets of diffracting planes result in the same length of scattering vector for each crystallite. However, their direction is different due to the different crystallite orientations resulting in a hemisphere as a sum of all scattering vectors describing the same lattice planes. This is illustrated by rings in Fig. 4.11a. The dark grey rings have also a corresponding reflection of the single-crystal in the displayed scattering plane.

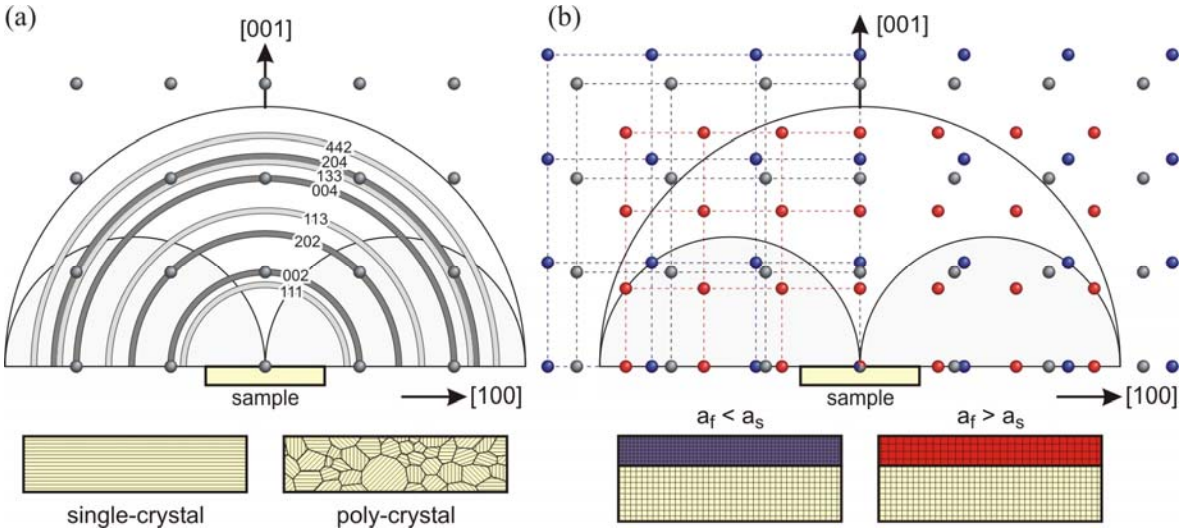

Fig. 4.11. (a) Comparison of single-crystalline (discrete spot pattern) and polycrystalline material (sum of reflexes from all crystallites result in spheres) in reciprocal space. The rings represent the cross-section of the spheres where rings in light grey show reflexes which have no discrete spot in this scattering plane. (b) Changes in the reciprocal lattice for epitaxial single-crystal rock salt films (cube-on-cube orientation) with lattice parameters smaller (blue) and larger (red) as the substrate (grey dots).

Until now we have just considered bulk materials, but the focus of this work is thin films. With XRD, information of film and substrate is obtained simultaneously and therefore the corresponding individual results also overlap in reciprocal space. A polycrystalline film on a single-crystal substrate of the same material would probably look like the representation in Fig. 4.11a. Single-crystal films on single-crystal substrates however show overlapping spot pattern as illustrated in Fig. 4.11.b. If the lattice parameter of the film is smaller than the substrate (i.e. c-$Al_xCr_{1-x}N$ on MgO), the corresponding reciprocal lattice becomes bigger as shown by the blue (film) and grey (substrate) lattices in Fig. 4.11b. This is inversed for films with larger lattice parameters (red dots).

The various XRD measurement techniques differ by the resulting paths of the scattering vector in reciprocal space, where the most important ones for this work are summarized in Fig. 4.12a-d. Each example has three sets of vectors (thick, middle, and thin lines) consisting of an incident wave vector $\mathbf{K}_0$ (corresponds to the x-ray source), a scattered wave vector **K** (corresponds to detector), and a scattering vector **Q**. The relative movements of x-ray source and detector are indicated by solid black arrows, the resulting movement of the scattering vector in reciprocal space by dashed black arrows/lines/areas.

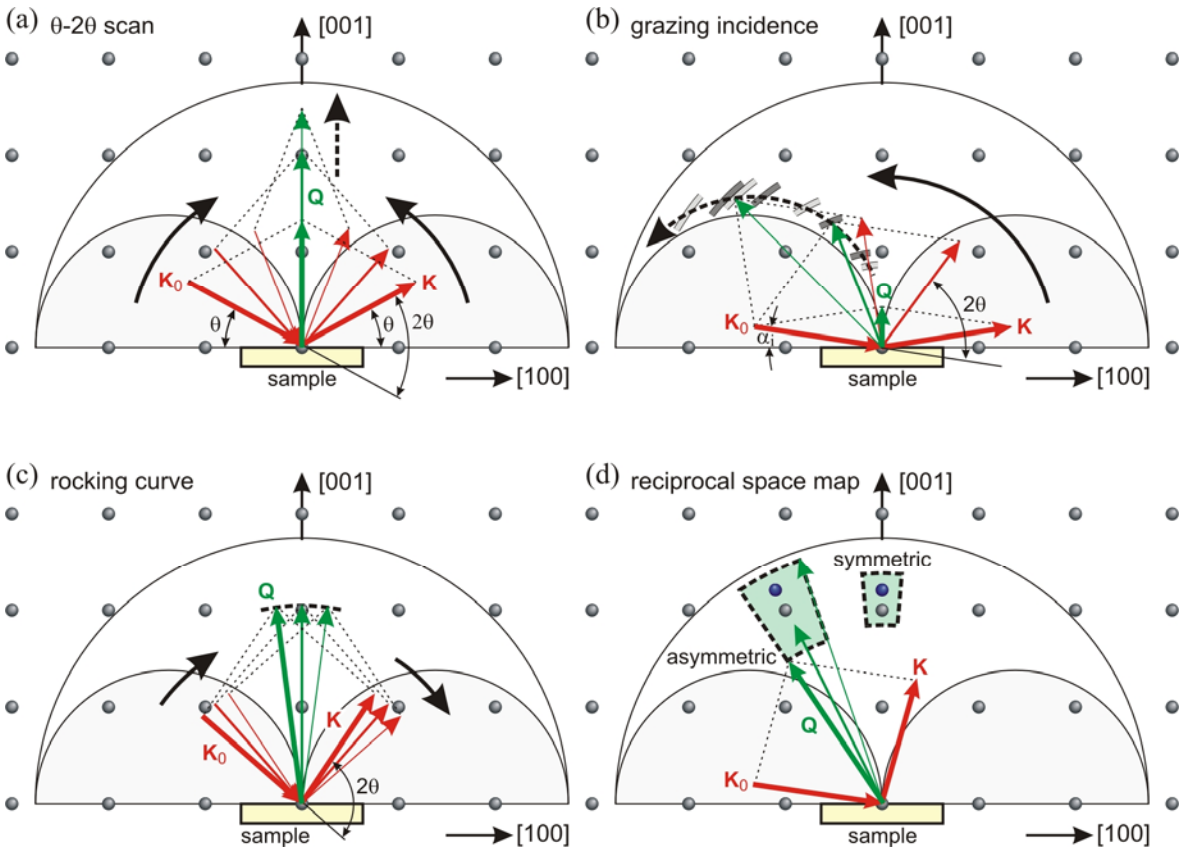

Fig. 4.12. Different x-ray diffraction techniques schematically illustrated in reciprocal space. (a) θ-2θ scan, (b) grazing incidence diffraction with indicated ring positions of polycrystalline material along the path of the scattering vector, (c) rocking curves, and (d) reciprocal space maps, assembled out of several rocking curves at different 2θ values.

Probably the most used technique in material science for analyzing present phases in a sample is the θ-2θ scan (Fig. 4.12a). The angles of x-ray source and detector in respect to the sample surface are equal and are increased symmetrically during the measurement. Accurately this refers to a θ-θ scan because the sample is fixed. Sometimes, especially in older diffractometers, the source can not be moved so the sample will be rotated by θ and the detector by 2θ which is the origin of this name. However, independent of the movement of sample and diffractometer arms, the scattering vector is always perpendicular to the sample surface and increasing in length for higher 2θ values. If the scattering vector hits a reciprocal lattice point or a corresponding ring of a polycrystalline material, the diffraction conditions for constructive interference are fulfilled and the detector records intensity.

Sometimes the diffraction information from the underlying substrate is desired as an angular reference but normally, especially for overlapping peaks in the diffractograms, a reduction of the substrate contribution is desired. Using an asymmetric measurement geometry with a fixed low incidence angle α_i of the x-rays (Fig. 4.12b) results in a significant increase in traveling distance for the x-rays in the film material. Therefore, the relative amount of information coming from the film compared to the substrate can be improved compared to θ-2θ scans. It should also be mentioned that the low incidence angles require a parallel beam of x-rays, which makes a suitable primary x-ray optic necessary. A schematic illustration of this measurement technique is given in Fig. 4.12b. Due to the resulting path of the scattering vector, grazing incidence diffraction is unsuitable for single-crystal investigations. However it is perfect for studying polycrystalline materials because **Q** intersects with all occurring rings in reciprocal space during the measurement (indicated in Fig. 4.12b). Diffractograms of a polycrystalline film on a single-crystal substrate will therefore result in just film reflexes.

Size and shape of reciprocal lattice points (RLP) offer detailed insights in structure and crystalline quality of single-crystal films [144-146]. One way to access this information is to combine a θ-2θ scan with a rocking curve (Fig. 4.12c) resulting in two perpendicular line scans across the selected reciprocal lattice point. Rocking curves are generated by keeping the 2θ angle fixed and varying the incidence angle to the substrate.

Investigations on the exact position and shape of a reciprocal lattice point or the relations of substrate and epitaxially grown films require knowledge of the complete area. This can be achieved by rasterizing via a combination of θ-2θ scans and rocking curves Fig. 4.12d. Such a set of measurements, representing an area in reciprocal space, is called reciprocal space map (RSM). Dependent on the investigated RLP, symmetric and asymmetric RSM are distinguished as displayed in Fig. 4.12d.

4.2.2 Transmission electron microscopy (TEM)

Transmission electron microscopy (TEM) is a special technique among electron microscopy due to the obtained volume information of a specimen by the transmission of

an electron beam. The first transmission electron microscope was built in the early 1930s with the goal to improve the image resolution compared to optical microscopes. Over the years, these microscopes developed to a very valuable analyzing tool in materials science (and other field of science as well) where various electron matter interactions are utilized to obtain sample information additional to imaging. Several of these possible interactions between an electron beam and a thin specimen are illustrated in Fig. 4.13.

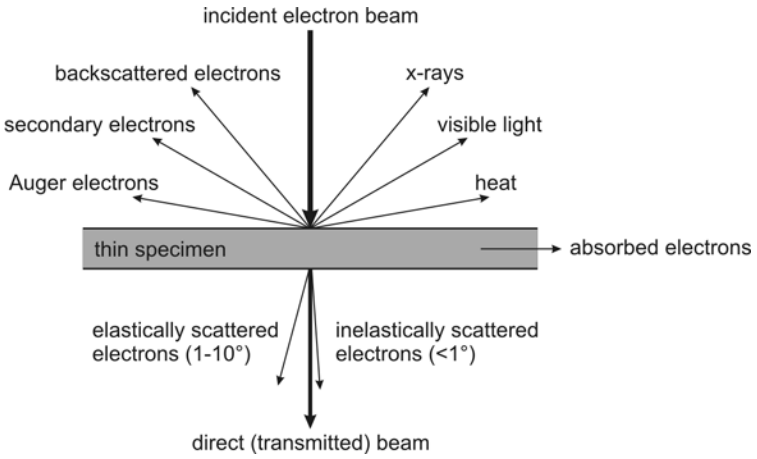

Fig. 4.13. Schematic illustration of possible signals due to interactions of a high energy electron beam with a thin specimen [147].

Some of these signals were employed for analytical purposes in this work next to imaging in different modes. Elastically scattered electrons were used for diffraction, x-rays for chemical analysis by energy dispersive x-ray spectroscopy (EDX), and inelastically scattered electrons for electron energy loss spectroscopy (EELS). These analytical opportunities combined with the superior resolution and the simultaneous generation of real space and reciprocal space information (diffraction) are the big strengths of transmission electron microscopy and are a perfect complementary investigation technique for XRD. However, one has to keep in mind that the obtained material information is very local due to the small probed volume. The interpretation of the resulting images can be difficult due to a two-dimensional projection of the investigated volume and superposition of different contrast mechanisms. The field of TEM is huge and can not be covered here. For further details general TEM literature and specialized textbooks for each technique are

available [147-151]. This chapter summarizes just very briefly some of the techniques important for this work and the corresponding publications.

The basic principle of a transmission electron microscope is quite comparable to a microscope operating with visible light just that the 'light' is coming from an electron source and the optical lenses are substituted by electromagnetic complements to magnify or condense the image. Improved resolution is achieved due to the lower equivalent wavelength of the electrons ($\sim 10^{-12}$ m for 200 keV acceleration voltage) compared to visible light ($\sim 10^{-7}$ m). To increase the mean free path of the electrons in the microscope the specimen has to be investigated in vacuum. All investigations in this work were performed on a FEI Tecnai G^2 TF20 UT microscope, equipped with EDX, EELS, and the opportunity for scanning transmission electron microscopy (STEM), shown in Fig. 4.14a. A schematic and simplified layout of a transmission electron microscope in general is presented in Fig. 4.14b.

Modern microscopes improved significantly over the years and are very sophisticated equipments nowadays. Some parts, however, like the electromagnetic lenses, have still room for improvement causing aberrations (chromatic aberration, spherical aberration, and astigmatism) which require correction procedures during the measurements. However, the most important factor, which limits the quality of the results, is the specimen itself. There exist several preparation techniques and dependent on the investigated material or the purpose of the study, different ones may lead to best results. The goal however is identical for all of them, namely to generate an electron transparent area of constant thickness (<100 nm) with as less as possible preparation artifacts.

In this work, the thin film samples were investigated by plan view and cross-sectional TEM. For the cross-sectional specimen, the sandwich technique was used where two sample pieces were glued together on the film side und placed in a TEM-grid. After this preparation step, the resulting disc was mechanically ground and polished to a thickness of ~50 µm, followed by dimpling from one side (production of a spherical cap for local thickness reduction), and a final ion milling step. Plan view samples were treated similar, obviously just from the back side of the film. Final thinning was done with Ar-ions in a Gatan precision ion polishing system (PIPS) where the energy was reduced to 2.5 kV for a final polishing step to remove amorphized layers of the specimen surface. The

purpose of this routine is the generation of a small hole (for sandwich specimen possibly at the interface) surrounded by thin electron transparent areas. During the whole preparation procedure it has to be ensured that the damage to the specimen due to mechanical forces (i.e. cutting, grinding) or thermal energy (i.e. ion milling) is low and no chemical or structural changes occur.

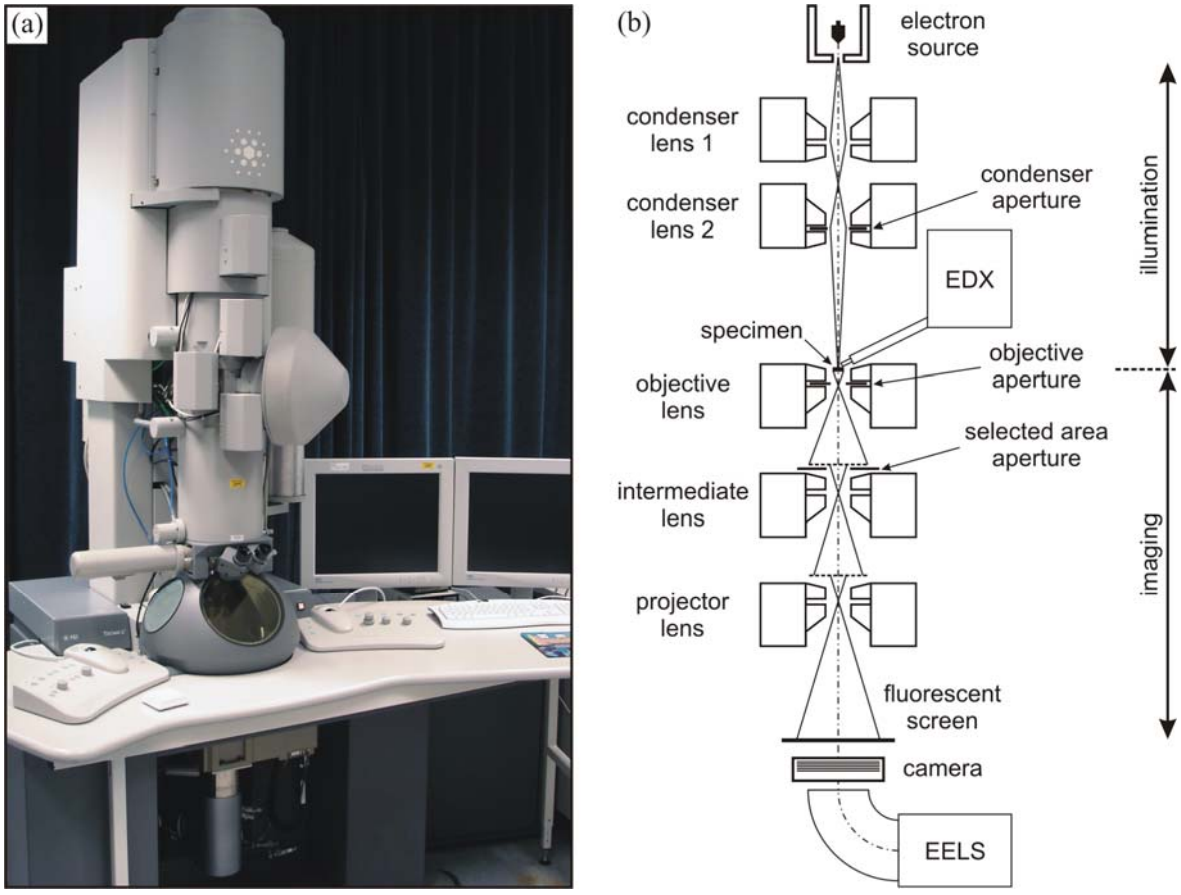

Fig. 4.14. (a) FEI Tecnai G^2 TF20 UT STEM transmission electron microscope equipped with EDX and EELS located at the Linköping University (called Galadriel). (b) Simplified schematic layout of an analytical transmission electron microscope (modified [152]).

The two fundamental operations of a transmission electron microscope are the formation of diffraction patterns and images, shown schematically in Fig. 4.15a and b, respectively. Displayed is the path of the beam in the imaging part of the microscope assuming that the specimen is illuminated by a parallel electron beam. Basically, the only difference between these two modes is the strength of the intermediate lens. The diffraction pattern gets projected to the screen when the back focal plane of the objective lens is the

object plane of the intermediate lens. If the image should appear at the screen, the object plane of the intermediate lens must coincide with the image plane of the objective lens. In the ray diagram in Fig. 4.15a electrons from the whole illuminated specimen area contribute to the diffractogram.

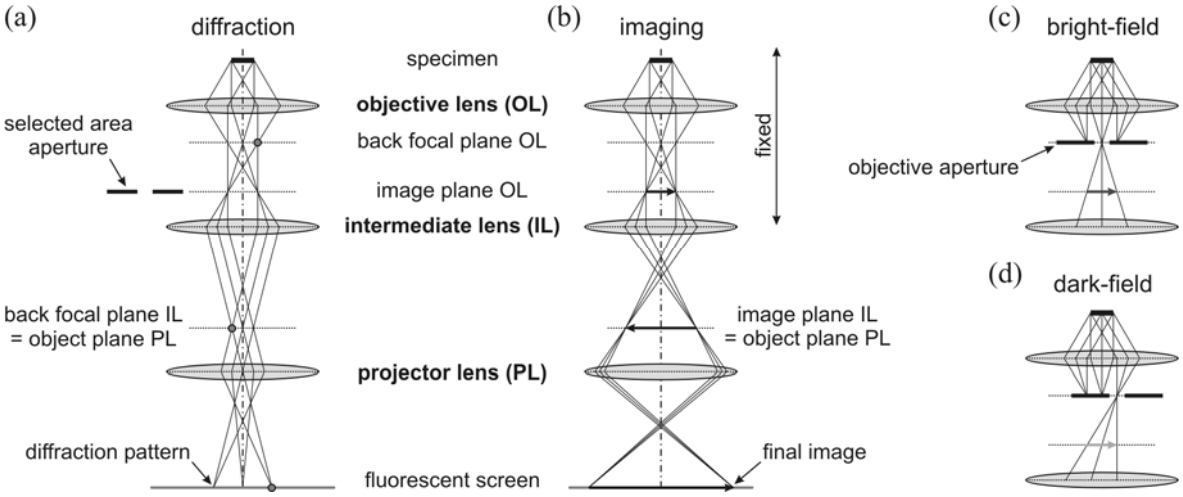

Fig. 4.15. Beam path for projection of the diffraction pattern (a) and image (b) on the screen. Displayed is the imaging part of the microscope with parallel incoming electron beam. Contrast enhancement by selecting just the direct beam (c) or the scattered beam (d) result in bright-field (BF) or dark-field (DF) images, respectively (based on [147,152]).

To determine the orientation of specific crystallites, or the crystallographic relation between two neighboring ones, the electrons contributing to the diffraction pattern must be limited to this area. This is done by inserting a selected area aperture in the image plane of the objective lens (Fig. 4.14b) resulting in selected area diffraction (SAD). Details on such an investigation are presented in Fig. 4.16, showing a cross-sectional BF image of a c-$Al_{0.60}Cr_{0.40}N$ film epitaxially grown on MgO (Fig. 4.16a). The film exhibits twins with a crystallographic orientation relationship of $(100)_{matrix}||(122)_{twin}$ and $[110]_{matrix}||[110]_{twin}$ demonstrated by the SAD patterns in Fig. 4.16b and c.

Variations for the image formation are done to enhance the contrast. In the ray diagram of Fig. 4.15b the direct and the diffracted beam contribute to the generation of the image, resulting in low contrast. Positioning an aperture around the direct beam or any diffracted beam in the diffraction pattern limits the image forming electrons and result in bright-field (BF) or dark-field (DF) images, respectively.

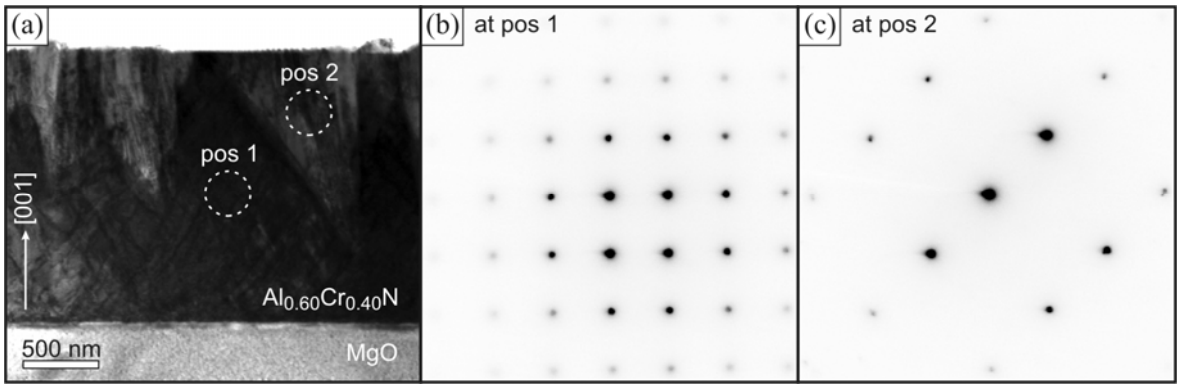

Fig. 4.16. (a) Cross-sectional BF transmission electron micrograph of c-$Al_{0.60}Cr_{0.40}N$ on MgO with (b) SAD patterns of the epitaxial grown matrix and (c) from one of the observed twins showing the crystallographic orientation relationship.

Such limitations are done by the objective aperture which gets inserted in the back focal plane of the objective lens (Fig. 4.14b). The corresponding differences are displayed in the according section of the ray diagrams for bright-field imaging, Fig. 4.15c, and dark-field imaging, Fig. 4.15d. Dark-field images like shown in Fig. 4.15d are made with an off-axis scattered beam and are therefore difficult to focus due to lens aberrations which are increasing with the distance to the optical axis [147]. This effect can be compensated by tilting the incident electron beam in a fashion that the scattered beam stays on the optical axis which then is called centered dark-field imaging (CDF). A comparison between BF and DF images of a specimen at the same position can be seen in paper 3.

Another possible TEM mode is scanning transmission electron microscopy (STEM). There, a small probe is focused into a small spot on the specimen. This spot is scanned parallel to the optical axis across the area of interest deflected by two pairs of scan coils [147]. Important for this work are images with mass-thickness contrast (Z-contrast). This can be achieved by a high-angle annular dark-field detector (HAADF) which, due to the special design, collects mainly incoherently scattered electrons [147]. Best mass-thickness contrast is obtained for high scattering angles meaning low camera lengths. The differences between a BF and a Z-contrast image can be seen in Fig. 2.5a and b, respectively. The very small probe (some Å) allows also localized chemical analysis via EDX or EELS. Due to the scanning coils also line scans or even maps can be realized. A line scan covering some grains of an annealed $Al_{0.70}Cr_{0.30}N$ specimen is presented in paper 1.

5 Mechanical properties

Mechanical properties are based on the bonding characteristics and the microstructure of a material [114]. Grain size, grain boundary dimensions, or voids therefore influence such properties (i.e. hardness). Variation of these parameters can be used for modification and improvement of the material which on the other hand directly influences technological properties like wear resistance or cutting performance. Different definitions of hardness can be found dependent on the subject area [153], where in materials science the hardness is the resistance to indentation. However, all definitions have in common, that the material is subject of plastic deformation, and the more difficult this deformation is, the harder the material is. Measuring hardness can become quite challenging, especially if anisotropic materials are tested, or the sample dimensions are small like in thin films.

5.1 Hardening mechanisms

Plastic deformation is connected to the movement of dislocations in the material and therefore, limitation of their mobility results in a hardness increase. General hardening mechanisms, which are important for this work, are described below. They are based on the variation of the material chemistry and/or characteristic lengths of the microstructure i.e. grain size, grain boundary width, obstacle radius, or obstacle spacing [154]. In this work only single-phase materials are considered as a base where mechanisms like defect hardening and solid solution hardening are important. In supersaturated materials, as concerned in this work, also change or formation of additional phases can occur after annealing. In special cases such newly formed phases, which precipitate out of a matrix, can lead to a hardness increase which is called precipitation hardening. Deposition technologies allow the production of nano-structured thin films where the structuring can be in one (multilayer), two (nano-columnar structure), or three (nano-composite) dimensions [114]. Each of them can lead to a strengthening effect. In sum all present

hardening mechanisms in a material superimpose, resulting in the measured hardness [154]. The contributing amount of each individual mechanism can change, i.e. with annealing temperature. However, this does not necessarily mean that the total hardness decreases, because a developing mechanism can compensate or even over-compensate the decrease/vanishing of another one. The individual mechanisms are described very briefly, but detailed descriptions and further information of all hardening mechanisms can be found in literature [114,154-157].

5.1.1 Strain hardening

Strain hardening (also called defect or work hardening) is caused by dislocation-dislocation and/or dislocation-lattice defect interactions. Applying a high enough shear stress results in dislocation movement or in special cases in a dislocation-multiplication (i.e. Frank-Read source). Dislocations, however, are lattice defects with resulting local strain fields around the lattice disturbance. For edge dislocations they are compressive above the slip plane and tensile below. Two edge dislocations with the same sign moving on the same glide plane experience repulsion. When the movement of a dislocation is blocked (i.e. at grain boundaries) this can lead to a pile-up and a local increase in dislocation density. If the sign is opposite (one half-plane above and one below the slip plane) they attract each other and can annihilate [156]. This, however, is just one special case of perfectly aligned edge dislocations. In a material also screw dislocations or mixed ones are present, moving on different slip planes where it can therefore occur that they intersect perpendicular resulting in kinks or jogs [157]. Such events occur more frequently for higher dislocation densities in a material. Since such interactions require additional shear stresses the material appears to be harder and stronger.

Deposition of polycrystalline hard coatings by PVD techniques creates a huge amount of lattice defects as a result of the growth processes (described in chapter 4) and the intense ion bombardment (see Fig. 4.1). These defects with their resulting strain fields also influence the dislocation mobility resulting in an effective hardening. Epitaxial films

can additionally show misfit dislocations which occur due to the different lattice parameters of film and substrate.

5.1.2 Solid solution hardening

A solid solution describes an alloy where the heterogeneity is on an atomic level [155]. There are different possible arrangements of the alloying elements in solid solutions, displayed schematically in Fig. 5.1, whereas the developed one depends on the size of alloying atoms and host matrix atoms. If the alloying atoms are small compared to the matrix atoms, they can sit in interstitial sites (Fig. 5.1a). For small size differences the alloying element can substitute a matrix element on a lattice site (Fig. 5.1b) which can occur ordered (Fig. 5.1c) if the elements show preferred bonding for each other.

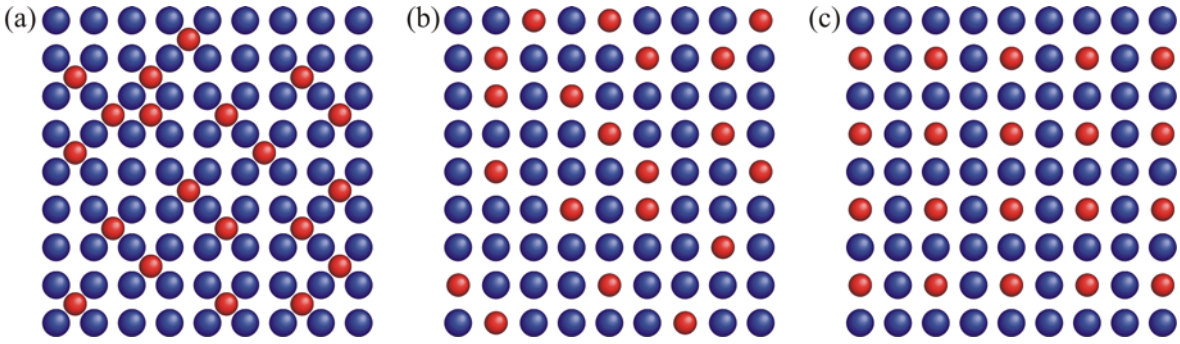

Fig. 5.1. Schematic illustration of different possible forms of a solid solution (after [158]). (a) The alloying element sits on interstitial sites, (b) alloying elements have a random distribution on lattice sites of the host lattice, and (c) ordered solid solution.

Compared to pure materials, alloying causes strain fields around the atoms which interact with dislocations. The hardness increases with the concentration of these alloying atoms compared to the base material. Solid solution hardening is a very effective hardening mechanism which is partly due to the strain fields of the dislocation itself, indicated for an edge dislocation in a pure material in Fig. 5.2a. Above the slip plane the additional half-plane causes compression whereas below tensile stresses are present. Alloying elements are able to reduce these strain fields and therefore the total energy of the material. Dependent on the size of the atoms they can arrange themselves above or below the slip

plane. Small atoms tend to be positioned in the compressive region (Fig. 5.2b), whereas the bigger ones find additional place in the tensile zone where it is easier to expand the lattice (Fig. 5.2c). Such preferred positioning causes locally an elastic relaxation of the lattice whose energy has to be applied additionally to move the dislocation. The resulting effect is hardening of the material due to an effective hindrance of the dislocation movement.

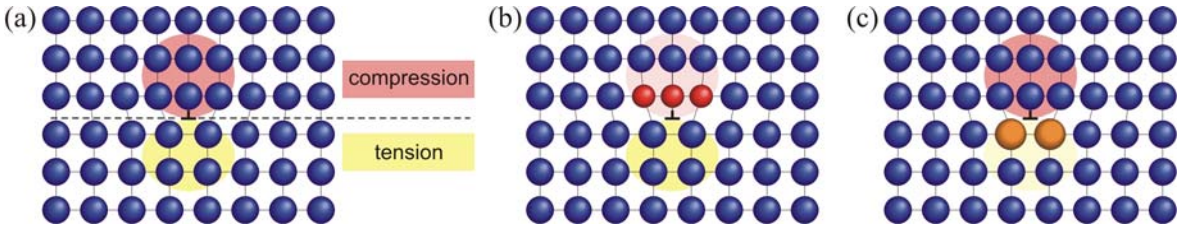

Fig. 5.2. (a) Schematic illustration of strain fields around an edge dislocation and their variation by (b) smaller or (c) larger substitutional atoms positioned in the compression or tension field, respectively (after [156]).

It also has to be considered that by addition of alloying atoms the chemical composition is changed and properties like shear modulus (increase) or stacking fault energy (typically decrease) are modified. This again has direct impact on the dislocation mobility [158].

5.1.3 Precipitation hardening

Small second-phase particles imbedded in a matrix material are able to interact with moving dislocations and can therefore enhance the hardness. If such particles are included in the material already during the production process the mechanism is called dispersoid hardening/strengthening. However, in solid solutions the formation of particles can also be initiated by a heat treatment resulting in so called precipitation hardening. Not all materials show such reactions, but if, the phase transformations can proceed via nucleation and growth or spinodal decomposition, two mechanisms described in detail in literature [114,155,157,159]. The kind of interaction of the particles with the dislocations is partly similar to them of lattice defects, described above. They can generate a strain field around themselves or change the overall shear modulus. Next to size, volume fraction,

distribution, and shape of the particles also their relation to the host lattice of the matrix is important for the amount of the resulting effect [155]. Different interfaces between the precipitates and the matrix are displayed schematically in Fig. 5.3. It can be distinguished between coherent particles where the lattice of the matrix is continued in the precipitate with only a slight misfit Fig. 5.3a, semi-coherent (Fig. 5.3b) and incoherent (Fig. 5.3c) precipitates where only certain or no lattice planes are continued, respectively.

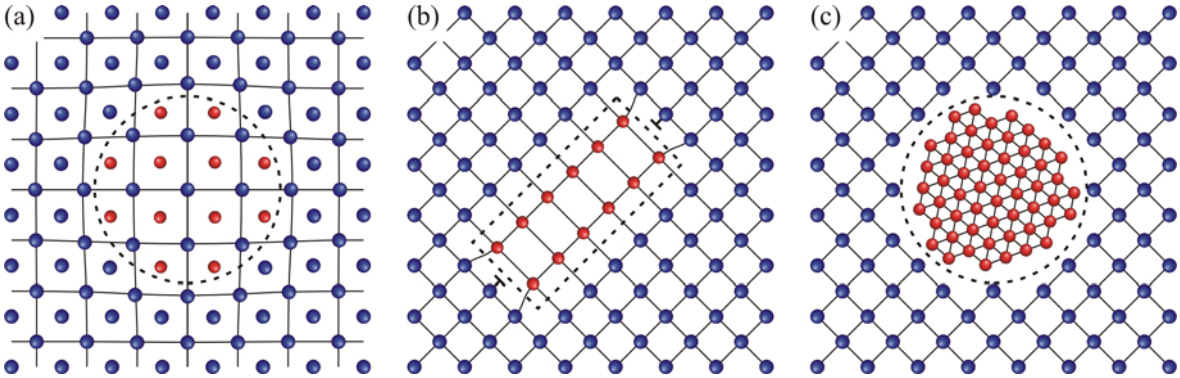

Fig. 5.3. Precipitates distinguished by the relation of their lattice to the matrix (after [157]), (a) coherent, (b) semi-coherent, and (c) incoherent.

If dislocations want to move on, they have to cut the precipitates or bypass them. For cutting, the dislocation has to be on a slip plane which prolongs to the precipitate. To do so, the dislocation has to overcome the strain field and the energy required to produce new additional interface between matrix and precipitate [155,159]. If the particle consists of an ordered alloy there may also be the contribution of additional anti-phase boundaries [155]. When the particles become too large to be deformed (cut), the dislocations have to bypass them. Therefore the moving dislocation line has to bow out between two particles until they curl around the obstacles and move on, leaving a dislocation loop around the precipitates [158]. This so called Orowan mechanism contributes to the overall hardness due to an effective reduction of the particle spacing with each loop and the contribution of the additional dislocation-dislocation interaction itself. Both effects, cutting and Orowan, occur simultaneously, whereas the optimum hardening effect is achieved for a given size-distribution relation of the precipitates, dependent on the material.

5.2 Nanoindentation

Various methods of indentation were developed over the decades, where the most important ones for materials science were defined by Vickers, Knoop, Brinell, and Rockwell [153]. All of them relate the applied load to a geometrical feature of the remaining imprint produced by indenters of different geometry. Vickers and Knoop uses different shaped four sided diamond pyramids, Brinell a steel ball, and Rockwell a steel ball or a diamond cone. These measurement techniques depend on a residual imprint in the tested material due to plastic deformation which is evaluated in size by optical methods.

To investigate thin films or modified surfaces, the indentation depth has to be reduced to ~10% of the film thickness and therefore the applied load has to be low [160]. This is a challenging task for the mechanics and electronics of the equipment which can be handled nowadays [153]. More limiting for thin film investigations are the dimensions of the residual imprints reaching a size where an accurate determination is difficult. The solution to this problem is called depth sensing indentation or instrumented indentation testing where force and depth of a loading and unloading indentation cycle are recorded. A schematic illustration of such an indentation is shown in Fig. 5.4a with a corresponding load-displacement curve in Fig. 5.4b. This technique is today standardized in the standard DIN EN ISO 14577 part 1-3 [161-163] and has the benefit that no size evaluation of the remaining imprint is necessary because hardness values are obtained from the evaluation of the unloading segment of the load-displacement curve (described below). Because the indentation area is measured indirectly a well defined geometry of the indenter is required. Therefore the four-sided Vickers pyramid was substituted by a three-sided pyramid which is easier to prepare with a sharp tip. This so called Berkovich indenter, which was also used in this work, has a face angle of 65.27° [160]. Measurements in this work were performed with loads in the range of mN and indentation depths of a few hundred nm. For such small loads the contribution of elastic deformation to the measured depth is significant and must be considered in a proper evaluation (Fig. 5.4a). In general the probed volume is small, why it can be ranked as a non-destructive investigation technique. On the other hand it is necessary to evaluate several indents to obtain a statistical representative hardness value of the material.

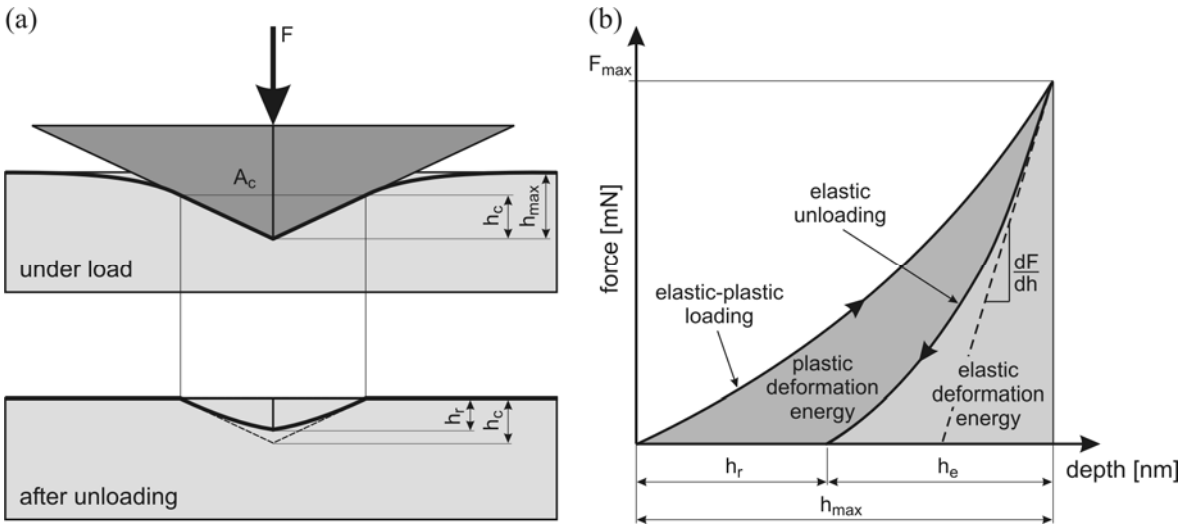

Fig. 5.4. (a) Schematic illustration of an indentation with a pyramidal indenter under the load F. The elasto-plastic behavior of the material causes an indentation depth of h_{max} under maximum load F_{max}, whereas the indenter is only in contact with the material for the depth h_c. After unloading the residual imprint has the depth h_r due to elastic recovery (after [153]). (b) Schematic of a corresponding load-displacement curve with the loading and unloading segment. The elastic contribution to the maximum displacement is indicated with h_e (after [153] and [160]).

The most common evaluation method of the load-displacement curves, also used in this work, was proposed by Oliver and Pharr [164]. Hardness is defined as applied load (F) divided by the corresponding projected contact area (A_c). Whereas the load can be measured directly the determination of the projected contact area is more difficult. Direct imprint evaluation is associated with a large error due to the small dimensions. Therefore an indirect technique is used requiring analysis of the real indenter shape. Such area functions relate a cross-sectional area of the indenter to the distance from the tip. Thus, correct values of the contact depth are required, which can be calculated out of an indenter geometry dependent factor and the contact stiffness dF/dh at h_{max} [164]. This is indicated by the linear fit of the upper part of the unloading curve in Fig. 5.4b, however, Oliver and Pharr discovered that best description of the unloading segment can be obtained by a power law relation w[164]. According to the standard, the upper 80% of the unloading data (dependent on the quality of the curve) should be fitted for proper stiffness evaluation [161]. Hence, all values for hardness determination are accessible from the load displacement curve. Mathematical derivations as well as detailed information on indentation and data evaluation and can be found in literature [153,160-164].

6 Thermal stability

Microstructural and mechanical properties of thin films which are usually excellent in the as-deposited state can change during thermal load. In many applications the local or general temperature exceeds the deposition temperature. To evaluate the usability of film materials as protective coatings for such applications primary investigations of reactions in the desired temperature range and the associated changes in the material properties have to be known. Basically this can be obtained in-situ, where the property of interest is monitored directly at a given temperature. But also ex-situ techniques, like post-deposition annealing and subsequent investigations allows drawing conclusions on the material response to the applied temperature program.

In this work, measurements like nanoindentation, transmission electron microscopy, or x-ray diffraction were performed ex-situ after annealing the samples to temperatures of interest. The corresponding time-temperature programs for the heat treatment were extracted from in-situ measurements, in this work especially from simultaneous thermal analysis. Structural changes of selected samples, however, were investigated in-situ by high-temperature x-ray diffraction. Thereby additional information of the processes, like onset or development over temperature, can be obtained from one sample avoiding possible additional reactions during cooling. The used in-situ techniques are described in this chapter with an emphasis on simultaneous thermal analysis (STA) which is a powerful tool for high-temperature studies.

6.1 Simultaneous thermal analysis (STA)

Thermal Analysis (TA) is defined as the analysis of a change in a sample property, which is related to an imposed temperature alteration [165]. This definition is very general and covers several measurement techniques. If two or more of these are applied simultaneously on one and the same sample at the same time, this combination is called simultaneous thermal analysis. The huge benefit of such combined measurements

compared to separate ones are mainly the identical measurement conditions (sample mass, heating rate, gas flow conditions, type of furnace, …) and the perfect correlation of the different signals because all data are obtained from the same sample at the same time.

In this work (paper 1 and 2) a Netzsch STA 409C was used (Fig. 6.1a), combining differential scanning calorimetry (DSC), thermogravimetric analysis (TGA), and mass spectrometry (MS) which are described later on in this chapter. The picture in Fig. 6.1a shows the equipment open. For the measurements a furnace is put over the sample carrier (Fig. 6.1b) and the desired atmosphere is adjusted, which can be inert (i.e. He, Ar) or oxidizing (air, O_2). The sample is exposed to a time-temperature program which can be continuous or isotherm [166] and the resulting signals are monitored by the corresponding sensors, recorded and analyzed by a computer based system.

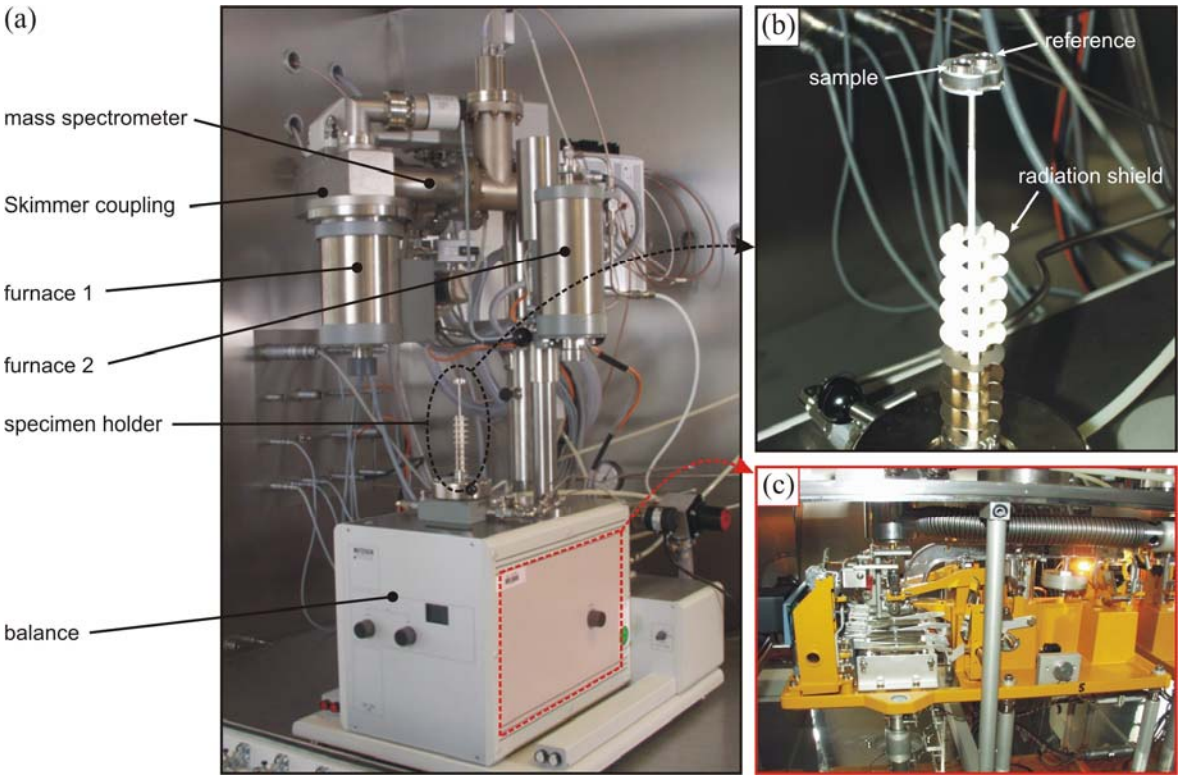

Fig. 6.1. (a) Netzsch STA 409C combining DSC, TGA, and MS. (b) Sample carrier with radiation shields as used for DSC measurements. Positions for sample and reference are indicated. (c) Mechanical balance for TGA measurements.

STA measurements require just a small amount of material making this technique perfect for thin film analysis. Some important points, however, have to be considered.

Initially it can not be distinguished if a monitored effect is caused by the film itself or the corresponding substrate. To overcome this problem, different sample preparation techniques can be used according to the goal of the investigation. If the contribution of the film material to the signal is too weak, the volume can be increased by thicker films, double side coated substrates or simply measuring more samples simultaneously [166]. For investigation of interface reaction also the fabrication of multilayers can be an option [167]. For all of these techniques, substrates are recommended, which are thermally inert in the investigated temperature range and show no undesired reactions with the film materials (e.g. sapphire). Another opportunity is to remove the film from the substrate to generate a free standing film. This can be achieved by using an initial layer which is soluble or has bad adhesion [167]. In this work (paper 1 and 2), low alloyed steel foils (Fig. 6.2a) were used as substrates which were chemically dissolved in 10 mol% nitric acid after deposition, leaving pure film material behind. Generally it has to be ensured that the removal procedure is not influencing the investigated films (e.g. chemical composition). The way from the plain substrates to the ready to use STA crucible is shown in Fig. 6.2a-d with the example of $Ti_xZr_{1-x}N$ (Fig. 6.2b). After dissolving the deposited substrates, the film material was cleaned, dried, and ground to a fine powder (Fig. 6.2c) whereof 30 mg were used for each measurement in the designated crucibles (Fig. 6.2d). Before investigation, the powder was exposed to elevated temperatures (100-150 °C) to remove potential residuals coming from this preparation procedure.

Fig. 6.2. Sample preparation steps for STA measurements to obtain film material without substrate. Low alloyed steel foils (a) coated with $Ti_xZr_{1-x}N$ (b). Cleaned powder after chemical substrate removal (c) placed in a STA crucible with lid (d).

Before conducting such high-temperature analysis it is important to ensure that there are no possible reactions (e.g. low melting eutectics) of the film material with the crucible or the sample carrier material.

6.1.1 Thermogravimetric analysis (TGA)

Thermogravimetric analysis (TGA) or thermogravimetry (TG) are methods for measuring the sample mass or mass difference as a function of temperature and/or time [165]. Various different instruments are commercially available today, whereas they are equipped either with a digital or a mechanical balance system. The STA system used in this work has a mechanical balance located below the sample holder (Fig. 6.1a), where the mechanics of the balance can be seen in Fig. 6.1c.

In TGA the change in mass can be positive (increase) due to reactions with the ambient atmosphere (e.g. oxidation), or negative (decrease) as in the case of e.g. decomposition with volatile reaction products. Both effects were investigated in this work (paper 1 and 2). In general TGA is a straight forward technique without many difficulties. The absolute mass change can be easily obtained by determining the sample mass before the measurement. However, parameters like gas flow or gas density and their temperature dependence affect the buoyancy of the sample carrier. For comparability of measurements in different atmospheres it is recommended to generate a base line of the equipment which can be used to correct the signal. Otherwise it has just to be ensured that the sample can freely interact with the surrounding atmosphere to consume potential reaction partners or release volatile products. If the mass change should be related to a given surface, fully coated substrates are preferably better than fine powders with undefined surface area.

Examples for isothermal TGA measurements are shown in Fig. 6.3a. There, coated discs were rapidly heated to the indicated temperatures which were then kept constant. The mass gain due to this isothermal oxidation is monitored over time showing different oxidation rates [19]. The effect of decomposition due to braking Cr-N bonds can be seen in Fig. 6.3b. $Al_xCr_{1-x}N$ powders ($0 < x < 1$) were continuously heated up to 1450 °C with a heating rate of 10 K/min. A significant decrease in sample mass is observed for c-$Al_xCr_{1-x}N$ due to the release of nitrogen in a two-step decomposition process where Cr is formed via Cr_2N (paper 1 and 2) [168]. The total mass loss is dependent on the amount of Cr-N bonds and therefore on the Cr-content in the stoichiometric nitride film. However, this comparison demonstrates a stabilizing effect of Al on the decomposition of c-$Al_xCr_{1-x}N$ for $x > 0.45$ by a ~120 °C higher onset temperature. AlN is reported to be

stable up to 2800 °C and therefore shows no mass loss [23]. $Al_{0.85}Cr_{0.15}N$ has a low amount of Cr-N bonds anyway, but additionally the material exhibits wurtzite crystal structure, which explains the minor mass loss which is shifted to higher temperatures [12]. This is caused by encapsulation of the CrN in a thermally stable AlN based matrix which acts as diffusion barrier and therefore changes the effective nitrogen partial pressure.

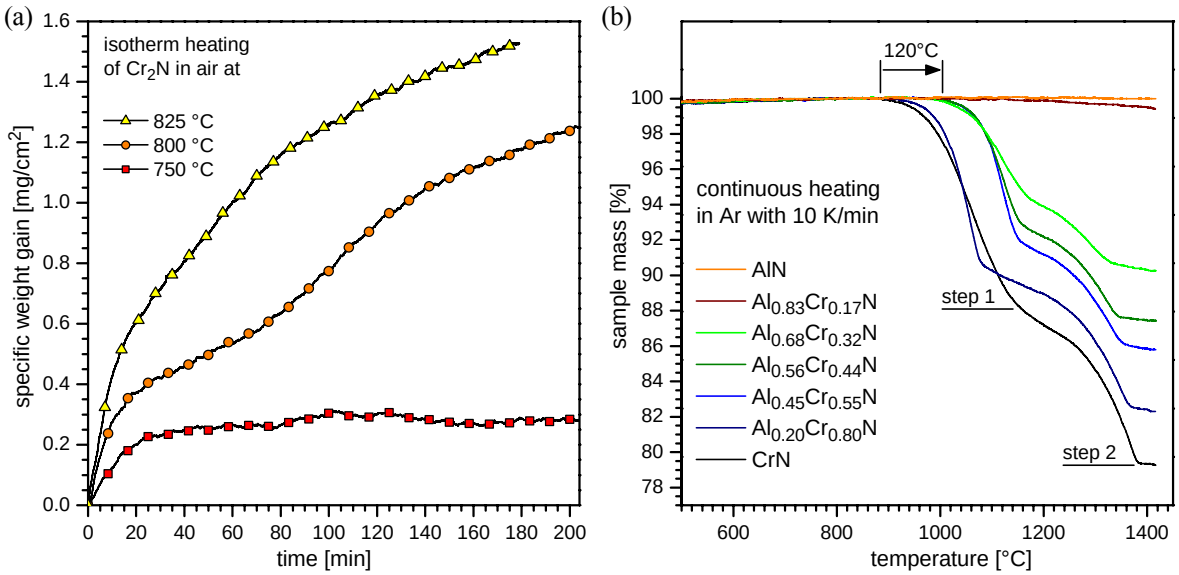

Fig. 6.3. (a) Oxidation of Cr_2N during isothermal annealing in air at different temperatures [19]. (b) Mass loss of $Al_xCr_{1-x}N$ ($0 < x < 1$) in Ar during continuous heating with 10 K/min due to decomposition.

6.1.2 Differential scanning calorimetry (DSC)

When applying high enough temperatures all materials undergo physical and/or chemical changes. Variations connected with the generation (exothermic) or consumption (endothermic) of heat can be investigated by calorimetry. Several designs based on different ways of sample arrangement and heating are available, also measuring different physical properties. To avoid confusion or misunderstanding, first of all a brief description of their differences and the corresponding names of the measurement techniques is given. However, all of them have in common, that the sample is compared to a reference material and that both, sample and reference, are exposed to a programmable time-temperature program in a specified atmosphere. In differential scanning calorimetry the difference in

heat flow rate (or power) to the sample and to the reference sample is continuously monitored during altering the temperature [165]. If just the temperature difference is measured the technique is called differential thermal analysis (DTA) [169] and is not considered in this work. Differential scanning calorimeters can be divided by the method of measurement in power compensation DSC and heat-flux DSC [165]. Power compensation instruments have separate heating for sample and reference sample and the reaction dependent temperature difference is immediately compensated by a corresponding change in the heating power [170]. This differential heating power can be related to the heat flow rate in the sample, just corrected by calibration factors due to thermal losses. In a heat-flux DSC, as used in this work (paper 1 and 2), sample and reference sample are positioned symmetrically in respect to one heating source Fig. 6.1b and the measured variable is the temperature difference [167], comparable to DTA. However, to obtain the required heat flow rate the amplitude of the signal must be correlated to the power dissipated by the studies effect [171]. This is done by calibration, e.g. employing standard samples with melting points covering the temperature range of interest and relating the measured heats of fusion to literature values [171]. The resulting calibration curves for temperature and sensitivity are just valid for one defined set of measurement conditions (heating rate, atmosphere, furnace, crucible material, sample carrier) and are not valid any more if one of this parameters is changed. Real equipments for heat-flux DSC are thermally not symmetric, resulting in a measured signal also without loaded sample. To compensate for this effect a zero line, measured with empty crucibles under identical measurement conditions, is subtracted from the original measured data [170]. One has to keep in mind that everything in the crucibles (and even the crucibles themselves) has a heat capacity and is altering the symmetry of the system, so does the sample and the reference material. One way for optimization is 'balancing' by using an inert reference material with equal thermal properties to the sample, but also empty reference crucibles are common [165]. For irreversible reactions (e.g. recovery, decomposition, crystallization, precipitation) the zero line can be achieved by performing a second measurement run (rerun) which contains the characteristics of an 'inert' sample without all the one-way reactions, already occurring in the first measurement. This technique was used successfully in paper 1 and 2.

The information of DSC measurements is manifold and can be used e.g. for the generation of phase diagrams, determining the heat capacity of a material, or investigate reactions [170]. The sign of the DSC response indicates if the reaction is endothermic or exothermic, the area under the signal corresponds to the heat of reaction, and the shape of the peak gives rise to the kind of reaction [165,170]. Also the kinetics of a reaction can be accessed by evaluating measurements performed at different heating rates [172-179], but this is complicated for multiple overlapping reactions like in many hard coatings.

The development of a DSC peak is shown schematically for melting of a pure element in Fig. 6.4a [169], whereas the DSC measurement signal is obtained by subtracting the measured reference temperature (T_R) from the measured sample temperature (T_S). Differences between real measured and ideal reaction signal are indicated by the solid and dashed lines, respectively. The characteristic temperatures are plotted on an exothermic peak (grain growth) of $TiB_{1.25}N_{0.7}$ in Fig. 6.4b [169,170,180].

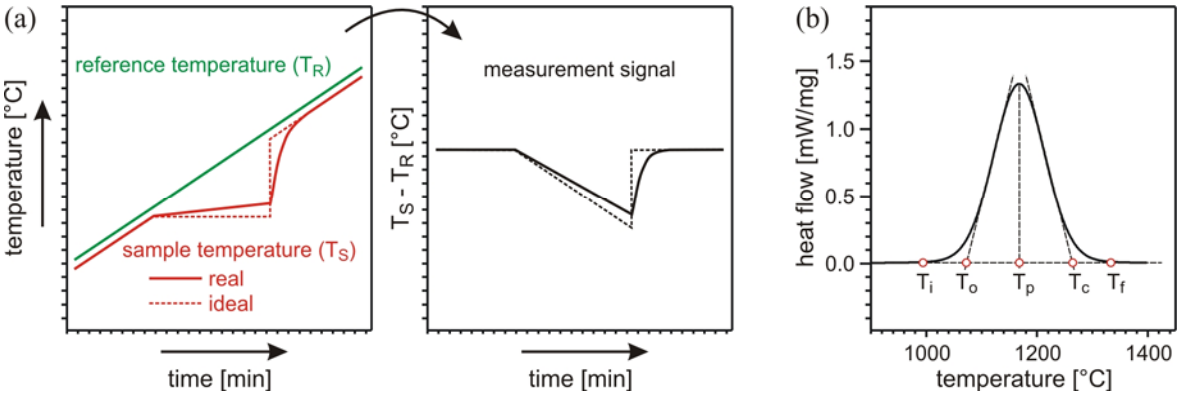

Fig. 6.4. (a) Schematic DSC signal formation on the basis of a melting process (based on [169]). (b) Characteristic DSC peak temperatures indicated at a measured grain growth peak of a $TiB_{1.25}N_{0.7}$ film [180]. T_i initial reaction temperature, T_o extrapolated onset temperature, T_p temperature of peak maximum, T_c extrapolated end temperature of the reaction, T_f final peak temperature (based on [169] and [170]).

A non-ideal shape of a DSC peak can be a result of all participating materials and their heat capacities (sample carrier, crucible, …) and/or bad thermal contact between the involved parts from sample to thermocouple, resulting in a slow response of the system to a change in the material. Additionally the sample itself, even though it is small, has finite dimensions and a limited thermal conductivity. This may cause temperature

inhomogeneities in the sample or a lag of the sample compared to furnace temperature during heating. This effect becomes stronger for higher heating rates and especially for large samples, which is undesired for applications where exact onset temperatures are required (e.g. phase diagram determination). However, the peak area is a constant with respect of time [165], resulting in more pronounced peaks with higher heating rates which can be beneficial for small reactions. The variation of the DSC signal with heating rate is shown for c-$Al_{0.45}Cr_{0.55}N$ in Fig. 6.5a. The curves show several overlapping reactions both exothermic and endothermic. Strong contributions, like the two endothermic decomposition steps, may obscure other reactions in this temperature range, making an analysis of single reactions difficult. Compared to the decomposition, the exothermic recovery peak is small, why it is shown in a magnified view in the insert of Fig. 6.5a. A comparison with $Ti_{0.34}Al_{0.66}N$, a material without endothermic contributions, is given in Fig. 6.5b. The exothermic formation peaks of Ti-rich (1) and Al-rich (2) domains by decomposition of the supersaturated $Ti_{0.34}Al_{0.66}N$ matrix are indicated [114,181].

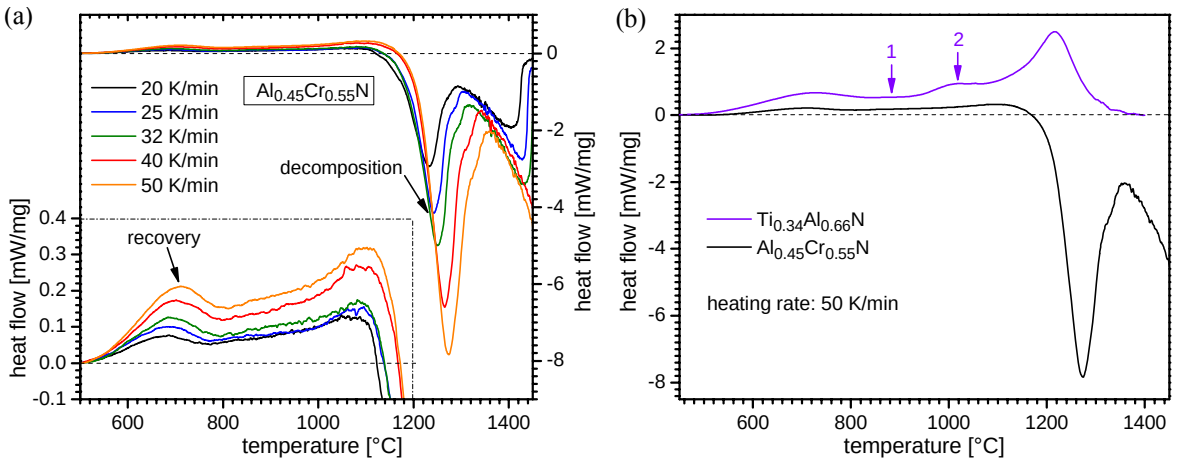

Fig. 6.5. (a) DSC curves of $Al_{0.45}Cr_{0.55}N$ arc evaporated coatings with different heating rates. (b) Comparison of arc evaporated $Al_{0.45}Cr_{0.55}N$ with strong endothermic decomposition peaks and $Ti_{0.34}Al_{0.66}N$ coatings, showing exothermic formation peaks of Ti-rich (1) and Al-rich (2) domains [114,181].

A detailed study on the precipitation behavior of c-$Al_{0.7}Cr_{0.3}N$ is presented in paper 1, where also a correlation of DSC and TGA signals is given. These investigations however are not self explaining and need additional information by XRD (chapter 4.2.1), TEM (chapter 4.2.2), or high-temperature x-ray diffraction (HT-XRD) (chapter 6.2).

6.1.3 Mass spectrometry (MS)

Combining DSC and TGA enables the access of detailed information of ongoing material reactions due to possible correlation of simultaneously obtained data. However, not every reaction results in a change in sample mass, but every variation in the TGA signal causes a corresponding DSC response. The exact determination of mechanisms underlying such changes in sample mass requires also knowledge of involved gaseous educts and/or products. This can be achieved by simultaneous analysis of the gaseous species involved in the reactions by mass spectrometry, additionally to DSC and TGA. In this work, a quadrupole mass spectrometer directly connected via a Skimmer coupling to the Netzsch STA 409C equipment was used for this task, see Fig. 6.6a. With this coupling system the detection of gaseous reaction products in the vicinity of their generation is possible by transfer via an orifice and a nozzle. The mass spectrometer consists of an ion source, a mass analyzer, and a detector system. To overcome the resulting pressure difference between the atmospheric pressure (10^5 Pa) in the sample area and the necessary high vacuum conditions (10^{-3} Pa) in the mass spectrometer, a double step pressure reduction is used. This pressure regulation system also increases the signal quality over the whole temperature range [182].

For analysis, the gas is ionized by a hot filament (Fig. 6.6a and b) which enables the separation with electric and magnetic fields according to the mass-charge ratio. This is done by the quadrupole, acting principally like a mass filter, transmitting only selected ions. It consists of two crosswise arranged pairs of electrically connected metal rods. Radio frequency (RF) and direct current (DC) voltages are superimposed to guide the ions along the rods. For a given applied voltage only ions with a certain mass-to-charge ratio can reach the detector, all others collide with the quadrupole rods. By variation of this voltage it is possible to allow other ions to pass, resulting in a possible scanning procedure.

Gas release from a sample due to decomposition is schematically illustrated in Fig. 6.6a, which shows the essential section of the Netzsch STA 409C (Fig. 6.1a). If the reaction consumes parts of the purge gas (e.g. oxidation), this results in drop of the corresponding gas level and is detected in the mass spectrometer. If the mass changes of decomposition

and oxidation would level out each other, it could still be detected by MS. Studies on the decomposition c-$Al_{0.70}Cr_{0.30}N$ by DSC, TGA, and MS are presented in paper 1.

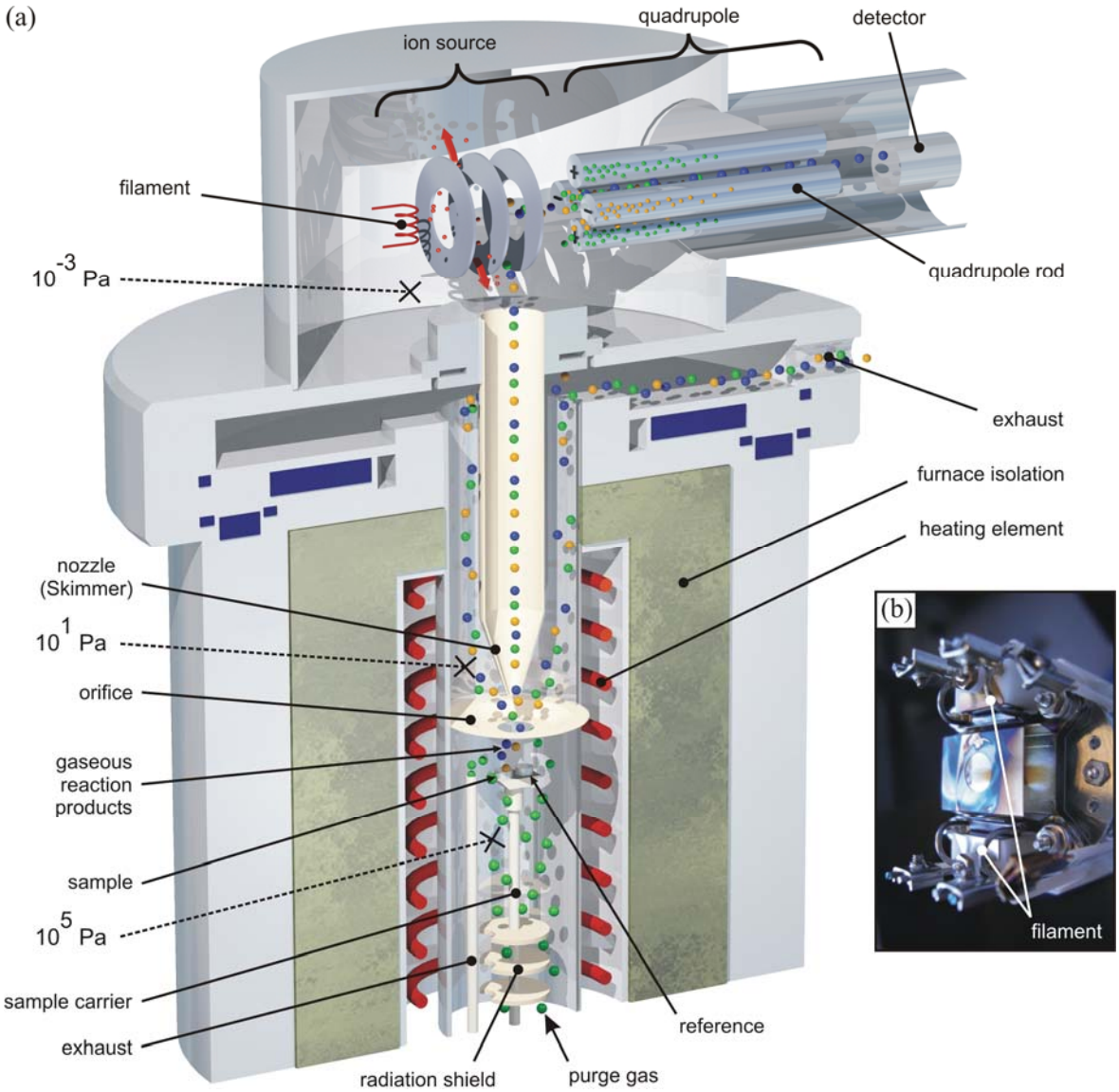

Fig. 6.6. (a) Schematic of the Skimmer coupling of a quadrupole mass spectrometer with a Netzsch STA 409C instrument (by courtesy of Netzsch-Gerätebau, Germany). (b) Picture of the ion source with filaments.

6.2 High-temperature x-ray diffraction (HT-XRD)

Structural changes in a material can be monitored in-situ during annealing using a HT-XRD compared to ex-situ investigations by XRD (4.2.1). In this work a Bruker D8 Advance equipped with an Anton Paar XRK 900 Reactor Chamber was used to investigate the development of the thin films during heat treatments up to 900 °C in inert atmosphere. Several furnace types are available, enabling the utilization of all x-ray techniques described in section 4.2.1.2 at elevated temperatures. It has just to be ensured, that the incident x-rays can reach the sample and the diffracting ones arrive at the detector. In the existing configuration for the high-temperature x-ray diffraction only θ-2θ scans were possible due to the construction of the heating chamber with x-ray transparent beryllium windows only along the scattering plane. Stepwise heating was used whereas the measuring temperature was kept constant during the diffraction experiment in the diffraction range of interest.

The investigated samples were epitaxial c-$Al_{0.68}Cr_{0.32}N$ films grown by unbalanced magnetron sputtering on MgO(001) and MgO(111), as in paper 3 and 4, respectively. Focus of this study was the comparison of thin films with similar chemical composition and different microstructure in their response to thermal loads. Source of this interest is the precipitation of w-AlN at the grain boundaries of polycrystalline arc evaporated c-$Al_{0.68}Cr_{0.32}N$ coatings on cemented carbide substrates. This effect was detected above 650 °C in ex-situ annealed samples by x-ray diffraction, shown in Fig. 6.7a (paper 2). The HT-XRD sequences of c-$Al_{0.68}Cr_{0.32}N$ on MgO(111) and MgO(001) are shown for $32° < 2\theta < 47°$ in Fig. 6.7b and c, respectively. The observable shifts in the peak positions, see magnified views in the inserts of Fig. 6.7b and c, are caused by the change in lattice parameter due to thermal expansion. For the films on MgO(001) (Fig. 6.7c) no linear lattice expansion is observed above the deposition temperature of 500 °C. This implies that the thermal expansion is overlapped by relaxation processes of the lattice.

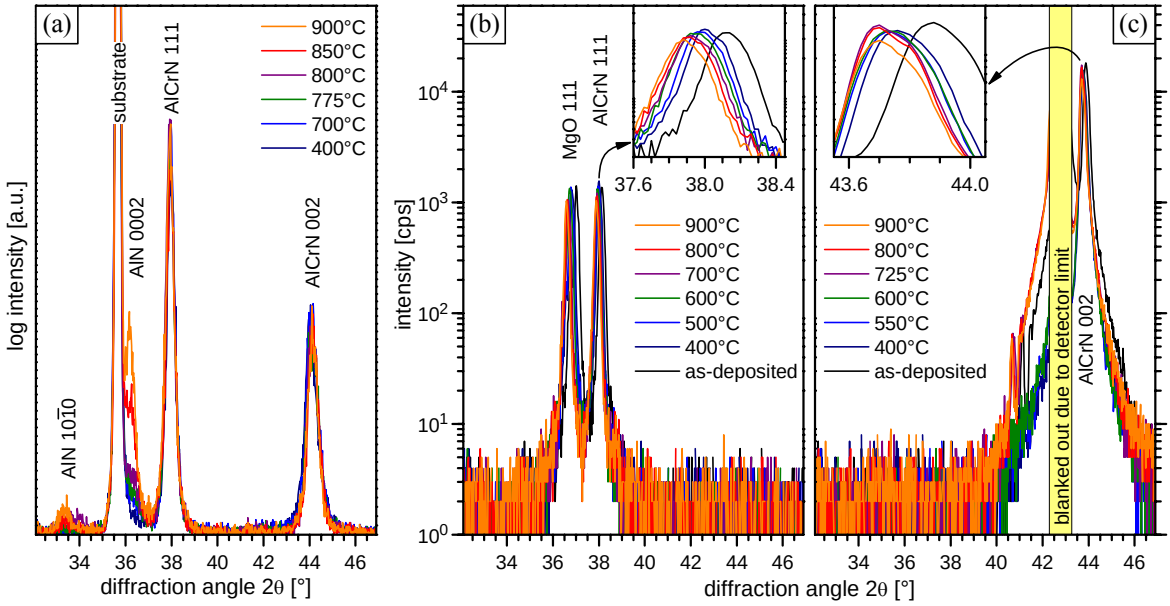

Fig. 6.7. (a) Diffractograms of polycrystalline arc evaporated c-$Al_{0.68}Cr_{0.32}N$ coatings, ex-situ annealed at different temperatures. In-situ HT-XRD measurements of epitaxially grown c-$Al_{0.68}Cr_{0.32}N$ on MgO(111) (b) and MgO(001) (c) with magnified views of the temperature induced shifts of the corresponding film peaks.

Up to the maximum furnace temperature of 900 °C, no phase transformations were detected in the epitaxially grown materials contrary to polycrystalline c-$Al_{0.68}Cr_{0.32}N$ films. There, the peak intensities increase with annealing temperature at the standard positions for AlN due to the growing phase fraction (Fig. 6.7a). Differences in the precipitation behavior may be attributed to missing nucleation sites in the epitaxial films, however, also other factors (film density, defect density, macro particles) related to the different deposition technique can not be ruled out at this stage.

7 Summary and conclusions

Within this work, the microstructural design of hard coatings for high temperature applications is studied, based on the model system $Al_xCr_{1-x}N$. This system is related to CrN which shows good hardness, oxidation resistance, chemical inertness, and anti-adhesive properties; however, its thermal stability is insufficient for modern high-performance applications. Increasing the Al-content along the pseudobinary CrN-AlN tie line of the ternary phase diagram changes the bonding structure and therefore also the resulting properties. Since $Al_xCr_{1-x}N$ is of high commercial interest, an industrial PVD arc evaporation system is used in this work to deposit a series of coatings with various Al-contents. For a detailed study on the design of structure and thermal stability of hard coatings epitaxial films are grown on differently oriented MgO substrates by laboratory-scale reactive unbalanced magnetron sputtering system. Structural investigations are performed by x-ray diffraction and transmission electron microscopy, mechanical properties are obtained by nanoindentation measurements, and thermal stability as well as high temperature reactions of the $Al_xCr_{1-x}N$ films are studied by simultaneous thermal analysis which combines differential scanning calorimetry, thermal gravimetric analysis, and mass spectrometry.

$Al_xCr_{1-x}N$ shows a phase transition from cubic (c) rock salt (B1) to hexagonal wurtzite (w) (B4) structure at AlN-contents in the range 0.7 - 0.75, dependent on the deposition technique. For arc evaporation, c-$Al_xCr_{1-x}N$ is stable up to an Al/Cr ratio of 70/30 ($x = 0.7$). However, the highest reported Al-content in the cubic modification is obtained in this work with c-$Al_{0.81}Cr_{0.19}N$, which could be epitaxially stabilized for ~100 nm by sputtering on MgO(001) templates. Detailed knowledge of this B1/B4 transition is important because c-$Al_xCr_{1-x}N$ shows superior mechanical properties compared to w-$Al_xCr_{1-x}N$, with an optimum close to the transition. Therefore, this work focuses on c-$Al_xCr_{1-x}N$, and especially on the investigation of the high-temperature behavior, the corresponding changes in structure and mechanical properties and the development of a detailed understanding of the underlying processes.

Simultaneous thermal analysis is conducted to determine the influence of Al on the thermal stability of the material, stating a stabilizing effect for AlN-contents ≥45 mol%, increasing the onset of decomposition (breaking of Cr-N bonds) by ~120 °C, from ~940 to ~1060 °C. Also the oxidation resistance is improved significantly by adding Al to the CrN, resulting in a dense solid solution $(Al,Cr)_2O_3$ oxide scale acting as diffusion barrier and protecting the remaining film and substrate material underneath. Further oxidation can proceed by diffusion of oxygen through the oxide which requires higher temperatures. In-situ STA oxidation experiments reveal for $Al_{0.56}Cr_{0.44}N$ coatings an onset of minor oxidation of ~1000 °C which is an increase of ~300 °C compared to CrN. Rapid oxidation of $Al_{0.56}Cr_{0.44}N$ starts at ~1200 °C, a temperature where also diffusion of substrate material can not be neglected any more. Due to the exceptionally good high-temperature behavior, additionally to improved mechanical properties, special emphasis is laid on films with chemical compositions close to the B1/B4 transition.

STA studies with different nitrogen partial pressures in an otherwise inert atmosphere show a strong influence on the N-loss and in general on the phase stability of c-$Al_{0.56}Cr_{0.44}N$ coatings. However, for the most demanding conditions (0% nitrogen in the atmosphere) the nitride shows stability in the B1 phase up to ~1030 °C which is increased by ~150 °C under 100% nitrogen conditions. At higher temperatures, the Cr-N bonds in the material break and a decomposition process starts which is investigated in detail for $Al_{0.56}Cr_{0.44}N$ and $Al_{0.68}Cr_{0.32}N$ in inert Ar atmospheres up to 1500 °C. In general, the decomposition of CrN proceeds along a two-step reaction process to pure metallic Cr and N_2 gas via the intermediate step of Cr_2N. These two steps are also observed for c-$Al_{0.56}Cr_{0.44}N$, where the remaining matrix becomes successively Al enriched during the decomposition. For continuous heating in Ar with a heating rate of 10 K/min, the decomposition is finished at ~1350 °C with a resulting structure of transformed w-AlN and Cr grains. $Al_{0.68}Cr_{0.32}N$, having an Al-content close to the B1/B4 transition, shows precipitation of w-AlN at grain boundaries by nucleation and growth as an additional reaction at ~650 °C. Thereby, the Al-level in the matrix depletes which can result in a local loss of the stabilization effect, causing a preferred (and earlier) decomposition. CrN dissociation itself proceeds along the same already described two-step reaction route to Cr via Cr_2N. For precipitation of w-AlN in the metastable c-$Al_xCr_{1-x}N$, the system has to

overcome the necessary activation energy to start the phase transformation plus the strain energy caused by the ~26% larger molar volume of w-AlN. The driving forces are thus not sufficient in c-$Al_{0.56}Cr_{0.44}N$ to initiate such precipitation at temperatures before the Cr-N bonds start to break.

Due to the different lattice structure of w-AlN and the resulting strain fields caused by the volume difference to the cubic matrix, the precipitates represent effective barriers for dislocation glide. The effect on the film hardness depends on size and distribution of the w-AlN precipitates which on the other hand depend on the annealing temperature. Initial precipitation generates a hardness peak at 725 °C with a ~5% increase compared to the as-deposited value of 30 GPa. Subsequent growth and coarsening induced by exceeding this temperature results in a hardness drop to 27.5 GPa after annealing at 900 °C. This is caused by the lower hardness of w-AlN and the reduction of Al in the c-$Al_xCr_{1-x}N$ matrix. Due to the absence of precipitation in c-$Al_{0.56}Cr_{0.44}N$, the solid solution hardening effect is not altered and the hardness remains on a constant high level of 30 GPa up to 1000 °C, by far exceeding the state of recovery. Apart from the hardness increase from 23 GPa for CrN to 30 GPa for the arc evaporated $Al_{0.56}Cr_{0.44}N$ and $Al_{0.68}Cr_{0.32}N$ coatings, the predominant hardening mechanisms suggest different temperature ranges for optimized application.

Precipitation of w-AlN in c-$Al_xCr_{1-x}N$ is observed for the first time during this work. However, the effect of grain boundaries on the kind of precipitation and the onset temperature remained unclear and become therefore subject of further investigations. A decrease in grain boundary density was obtained by epitaxial growth of c-$Al_xCr_{1-x}N$ on MgO(111) and MgO(001) templates. The developed microstructure in these films is influenced by the ad-atom mobility on the different surfaces. Whereas epitaxial single-crystal $Al_{0.68}Cr_{0.32}N$ films are grown on MgO(001) substrates, fine epitaxial columns are obtained on MgO(111). The average column diameter is dependent on the chemical composition and decreases with increasing Al-content. $Al_{0.68}Cr_{0.32}N$ on MgO(001) substrates exhibits a few nm thick pseudomorphic strained layer before epitaxial growth proceeds with a fully relaxed lattice parameter. Even though these films show a dislocation network, no grain or domain boundaries are observed. Subsequent in-situ annealing studies by high-temperature x-ray diffraction show phase stabilities up to

900 °C without any precipitation for epitaxial $Al_{0.60}Cr_{0.40}N$ and $Al_{0.68}Cr_{0.32}N$ films on either MgO(001) and MgO(111) substrates. Hence, this shows the strong dependence of annealing induced w-AlN formation on the grain boundary density.

In conclusion, metastable rock salt $Al_xCr_{1-x}N$ films with Al-contents close to the B1/B4 transition show a significant improvement in thermal stability, oxidation resistance, and hardness compared to CrN. The ability of c-$Al_{0.68}Cr_{0.32}N$ coatings for precipitation hardening offers interesting opportunities for self-adaptation during application. Further improvements of the coatings or even a tailoring of this effect could be obtained by additional alloying elements or optimized microstructure, like reduction of internal boundaries as shown for the epitaxial c-$Al_{0.68}Cr_{0.32}N$ layers. Development of functional coatings based on $Al_xCr_{1-x}N$ has to consider the effect of alloying elements on the developed phases. For obtaining single-phase rock salt structures, which performed best in mechanical applications up to now, Al/Cr ratios between 50/50 and 60/40 should be considered as starting compositions. High Al-containing c-$Al_xCr_{1-x}N$ solid solutions as hard protective coatings, however, enable already the access to high-temperature applications up to 1000 °C in various atmospheres, including air, under mechanically demanding conditions.

8 Symbols and abbreviations

8.1 Symbols

a	…	lattice parameter for cubic, or for basal plane in hexagonal materials
A_c	…	contact area
a_f	…	lattice parameter of the film
a_s	…	lattice parameter of the substrate
$a_{\parallel}$	…	in-plane lattice parameter for cubic materials
$a_{\perp}$	…	out-of-plane lattice parameter for cubic materials
a'	…	superstructure lattice parameter for basal plane in hexagonal materials
$\mathbf{a}_1$, $\mathbf{a}_2$, $\mathbf{a}_3$	…	basis vectors of the crystal lattice in real space
$\mathbf{b}_1$, $\mathbf{b}_2$, $\mathbf{b}_3$	…	primitive vectors of reciprocal lattice
c	…	lattice parameter perpendicular to basal plane for hexagonal materials
c'	…	superstructure lattice parameter perpendicular to a' for hexagonal materials
d	…	lattice plane spacing
F	…	indentation force
$\mathbf{G}$	…	vector from origin in reciprocal space to reciprocal lattice point
h	…	indentation depth
h,k,l	…	Miller indices
$\mathbf{K}_0$	…	incident wave vector
$\mathbf{K}$	…	diffracted wave vector
n	…	integral number
$\mathbf{Q}$	…	scattering vector
q_x, q_z	…	components of scattering vector
R_a	…	average roughness
T_a	…	annealing temperature
T_c	…	extrapolated end temperature of the reaction
T_f	…	final peak temperature of reaction

T_i	…	initial reaction temperature
T_m	…	melting temperature
T_o	…	extrapolated onset temperature of reaction
T_p	…	temperature of peak maximum
T_R	…	reference temperature
T_S	…	sample temperature
T_s	…	substrate temperature
V	…	volume of crystal unit cell
V_S	…	bias voltage
α	…	wetting angle
α_i	…	incidence angle of x-rays for grazing incidence measurements
$2 \cdot \Delta$	…	path difference of incident and diffracted x-rays
Γ	…	full width at half maximum
$\gamma_{S\text{-}V}$	…	surface energy of the free substrate surface
$\gamma_{S\text{-}F}$	…	surface energy of the film/substrate interface
$\gamma_{F\text{-}V}$	…	surface energy of the film surface to the vapor
θ	…	scattering angle
λ	…	wavelength
$\xi_{\parallel}$	…	lateral x-ray coherence length
$\xi_{\perp}$	…	vertical x-ray coherence length

8.2 Abbreviations

AE	…	Arc Evaporation
bcc	…	Body-Centered Cubic
B1	…	Crystal lattice structure designation, equivalent with rock salt type
B4	…	Crystal lattice structure designation, equivalent with wurtzite type
BF	…	Bright-Field
BSZM	…	Basic Structure Zone Model
c-	…	Cubic (NaCl) Structure
cc	…	Cemented Carbide
CDF	…	Centered Dark-Field
cps	…	Counts Per Second
CTE	…	Coefficient of Thermal Expansion
DTG	…	Derivative Thermogravimetry
EELS	…	Electron Energy Loss Spectroscopy
EDX	…	Energy Dispersive X-ray Spectroscopy
ERDA	…	Elastic Recoil Detection Analysis
fcc	…	Face-Centered Cubic
DC	…	Direct Current
DF	…	Dark-Field
DSC	…	Differential Scanning Calorimetry
DTA	…	Differential Thermal Analysis
HAADF	…	High-Angle Annular Dark Field
hcp	…	Hexagonal Closed Packed
HR-XRD	…	High-Resolution X-ray Diffraction
HT-XRD	…	High-Temperature X-ray Diffraction
MS	…	Mass Spectrometry
QMS	…	Quadrupole Mass Spectrometer
PIPS	…	Precision Ion Polishing System
PVD	…	Physical Vapor Deposition
RBS	…	Rutherford Backscattering Spectroscopy

RF	…	Radio Frequency
RLP	…	Reciprocal Lattice Point
RSM	…	Reciprocal Space Map
SA(E)D	…	Selected Area (Electron) Diffraction
SEM	…	Scanning Electron Microscope
SIMS	…	Secondary Ion Mass Spectroscopy
STA	…	Simultaneous Thermal Analysis
STEM	…	Scanning Transmission Electron Microscopy
SZM	…	Structure Zone Model
TA	…	Thermal Analysis
TEM	…	Transmission Electron Microscopy
TG	…	Thermogravimetry
TGA	…	Thermogravimetric Analysis
TOF	…	Time-Of-Flight
UBMS	…	Unbalanced Magnetron Sputtering
XPS	…	X-ray Photoelectron Spectroscopy
XRD	…	X-ray Diffraction
XRD	…	X-ray Diffraction
w-	…	Wurtzite Structure
XTEM	…	Cross-Sectional Transmission Electron Microscopy

9 References

[1] T. Massalski (Ed.), Binary Alloy Phase Diagrams, ASM International, 1990.

[2] Powder Diffraction File (Card 11-0065 for CrN), International Centre for Diffraction Data, ICDD - JCPDS, 1998.

[3] D. Gall, C.S. Shin, T. Spila, M. Odén, M.J.H. Senna, J.E. Greene, I. Petrov, J. Appl. Phys. 91/6 (2002) 3589.

[4] K. Inumaru, K. Koyama, N. Imo-Oka, S. Yamanaka, Phys. Rev. B 75/5 (2007) 054416.

[5] L.M. Corliss, N. Elliott, J.M. Hastings, Phys. Rev. 117/4 (1960) 929.

[6] J.F. Harrison, J. Phys. Chem. 100/9 (1996) 3513.

[7] F. Stevens, I. Carmichael, F. Callens, M. Waroquier, J. Phys. Chem. A 110/14 (2006) 4846.

[8] L. Hultman, Vacuum 57/1 (2000) 1.

[9] J. Almer, M. Oden, L. Hultman, G. Håkansson, J. Vac. Sci. Technol. A 18/1 (2000) 121.

[10] M.A. Djouadi, C. Nouveau, O. Banakh, R. Sanjines, F. Levy, G. Nouet, Surf. Coat. Technol. 151 (2002) 510.

[11] P.H. Mayrhofer, F. Rovere, M. Moser, C. Strondl, R. Tietema, Scr. Mater. 57/3 (2007) 249.

[12] P.H. Mayrhofer, H. Willmann, A. Reiter, 49th SVC Annual Technical Conference, Society of Vacuum Coaters, Washington, 2006, p. 575.

[13] Gmelins Handbuch der Anorganischen Chemie, vol. 8, Verlag Chemie GmbH, Weinheim, 1962, p. 157.

[14] S.J. Kim, T. Marquart, H.F. Franzen, J. Less Common Met. 158/1 (1990) L9.

[15] W. Ernst, Diploma Thesis, Thermal decomposition of CrN hard coatings, Department of Physical Metallurgy and Materials Testing, University of Leoben, 2006.

[16] A. Aubert, R. Gillet, A. Gaucher, J.P. Terrat, Thin Solid Films 108/2 (1983) 165.

[17] O. Knotek, W. Bosch, M. Atzor, W.-D. Münz, D. Hoffman, J. Goebel, High Temp. - High Press. 18/4 (1986) 435.

[18] W.D. Münz, J. Göbel, Surf. Eng. 3/1 , 1987 (1987) 47.

[19] P.H. Mayrhofer, H. Willmann, C. Mitterer, Surf. Coat. Technol. 146 (2001) 222.

[20] J. Vetter, Surf. Coat. Technol. 76-77/1-3 (1995) 719.

[21] T. Björk, M. Berger, R. Westergård, S. Hogmark, J. Bergström, Surf. Coat. Technol. 146-147 (2001) 33.

[22] T. Hurkmans, D.B. Lewis, J.S. Brooks, W.D. Münz, Surf. Coat. Technol. 86-87/1-3 (1996) 192.

[23] T. Massalski (Ed.), Binary Alloy Phase Diagrams, ASM International, 1990.

[24] P.H. Mayrhofer, C. Mitterer, H. Clemens, Adv. Eng. Mater. 7/12 (2005) 1071.

[25] P.H. Mayrhofer, D. Music, J.M. Schneider, Appl. Phys. Lett. 88/7 (2006) 071922.

[26] Powder Diffraction File (Card 25-1133 for B4 AlN), International Centre for Diffraction Data, ICDD - JCPDS, 1998.

[27] Powder Diffraction File (Card 46-1200 for B1 AlN), International Centre for Diffraction Data, ICDD - JCPDS, 1998.

[28] I.W. Kim, A. Madan, M.W. Guruz, V.P. Dravid, S.A. Barnett, J. Vac. Sci. Technol. A 19/5 (2001) 2069.

[29] Q. Li, I.W. Kim, S.A. Barnett, L.D. Marks, J. Mater. Res. 17/5 (2002) 1224.

[30] I. Petrov, E. Mojab, R.C. Powell, J.E. Greene, L. Hultman, J.E. Sundgren, Appl. Phys. Lett. 60/20 (1992) 2491.

[31] N.E. Christensen, I. Gorczyca, Phys. Rev. B 50/7 (1994) 4397.

[32] J. Birch, S. Tungasmita, V. Darakchieva, in: T. Paskova, B. Monemar (Eds.), Vacuum Science and Technology: Nitrides as seen by the technology, Research Signpost, Kerala, 2002, p. 421.

[33] O. Ambacher, J. Phys. D-Appl. Phys. 31/20 (1998) 2653.

[34] M. Kasu, N. Kobayashi, J. Cryst. Growth 221/1-4 (2000) 739.

[35] K.S. Stevens, M. Kinniburgh, A.F. Schwartzman, A. Ohtani, R. Beresford, Appl. Phys. Lett. 66/23 (1995) 3179.

[36] http://www.ioffe.ru/SVA/NSM/Semicond/index.html, Ioffe Physico-Technical Institute, 2007.

[37] M. Atzor, Dissertation, Aspekte des Magnetronsputterns zur Herstellung verschleiß- und korrosionsbeständiger Schichten auf Chrombasis, Serie 5: Grund- und Werkstoffe, No 156, RWTH Aachen, VDI-Verlag Düsseldorf, 1989.

[38] O. Knotek, M. Atzor, A. Barimani, F. Jungblut, Surf. Coat. Technol. 42/1 (1990) 21.

[39] S. Hofmann, H.A. Jehn, Werkst. Korros.-Mater. Corros. 41/12 (1990) 756.

[40] S. Hofmann, Thin Solid Films 193/1-2 (1990) 648.

[41] O. Knotek, F. Löffler, H.-J. Scholl, Surf. Coat. Technol. 45/1-3 (1991) 53.

[42] O. Knotek, F. Loffler, C. Barimani, G. Kraemer, Surface Coatings for Advanced Materials, vol. 246, Transtec Publications Ltd, Zurich-Uetikon, 1997, p. 29.

[43] M. Okumiya, M. Griepentrog, Surf. Coat. Technol. 112/1-3 (1999) 123.

[44] J. Vetter, E. Lugscheider, S.S. Guerreiro, Surf. Coat. Technol. 98/1-3 (1998) 1233.

[45] Y. Ide, K. Kishitake, T. Nakamura, J. Jpn. Inst. Met. 63/12 (1999) 1576.

[46] A. Sugishima, H. Kajioka, Y. Makino, Surf. Coat. Technol. 97/1-3 (1997) 590.

[47] Y. Makino, K. Nogi, Surf. Coat. Technol. 98/1-3 (1998) 1008.

[48] C. Kunisch, R. Loos, M. Stüber, S. Ulrich, Z. Metallkd. 90/10 (1999) 847.

[49] B.C. Schramm, H. Scheerer, H. Hoche, E. Broszeit, E. Abele, C. Berger, Surf. Coat. Technol. 188-189 (2004) 623.

[50] A.E. Reiter, V.H. Derflinger, B. Hanselmann, T. Bachmann, B. Sartory, Surf. Coat. Technol. 200/7 (2005) 2114.

[51] W. Kalss, A. Reiter, V. Derflinger, C. Gey, J.L. Endrino, Int. J. Refract. Met. Hard Mat. 24/5 (2006) 399.

[52] H. Scheerer, H. Hoche, E. Broszeit, B. Schramm, E. Abele, C. Berger, Surf. Coat. Technol. 200/1-4 (2005) 203.

[53] G.S. Fox-Rabinovich, B.D. Beake, J.L. Endrino, S.C. Veldhuis, R. Parkinson, L.S. Shuster, M.S. Migranov, Surf. Coat. Technol. 200/20-21 (2006) 5738.

[54] J.L. Endrino, G.S. Fox-Rabinovich, C. Gey, Surf. Coat. Technol. 200/24 (2006) 6840.

[55] E. Spain, J.C. Avelar-Batista, M. Letch, J. Housden, B. Lerga, Surf. Coat. Technol. 200/5-6 (2005) 1507.

[56] J.L. Endrino, G.S. Fox-Rabinovich, A. Reiter, S.V. Veldhuis, R.E. Galindo, J.M. Albella, J.F. Marco, Surf. Coat. Technol. 201/8 (2007) 4505.

[57] K. Bobzin, E. Lugscheider, M. Maes, P.W. Gold, J. Loos, M. Kuhn, Surf. Coat. Technol. 188-189 (2004) 649.

[58] C. Brecher, G. Spachtholz, K. Bobzin, E. Lugscheider, O. Knotek, M. Maes, Surf. Coat. Technol. 200/5-6 (2005) 1738.

[59] J.L. Endrino, V. Derflinger, Surf. Coat. Technol. 200/1-4 (2005) 988.

[60] M. Zhu, M. Li, Y. Zhou, Surf. Coat. Technol. 201/6 (2006) 2878.

[61] E. Lugscheider, K. Bobzin, S. Barwulf, T. Hornig, Surf. Coat. Technol. 133 (2000) 540.

[62] M. Brizuela, A. Garcia-Luis, I. Braceras, J.I. Oñate, J.C. Sánchez-López, D. Martínez-Martínez, C. López-Cartes, A. Fernández, Surf. Coat. Technol. 200/1-4 (2005) 192.

[63] R. Wuhrer, W.Y. Yeung, Scr. Mater. 50/12 (2004) 1461.

[64] R. Wuhrer, W.Y. Yeung, Pricm 5: the Fifth Pacific Rim International Conference on Advanced Materials and Processing, Pts 1-5, vol. 475-479, Trans Tech Publications Ltd, Zurich-Uetikon, 2005, p. 4001.

[65] H.C. Barshilia, N. Selvakumar, B. Deepthi, K.S. Rajam, Surf. Coat. Technol. 201/6 (2006) 2193.

[66] J. Lin, B. Mishra, J.J. Moore, W.D. Sproul, Surf. Coat. Technol. 201/7 (2006) 4329.

[67] X.Z. Ding, X.T. Zeng, Surf. Coat. Technol. 200/5-6 (2005) 1372.

[68] J.C. Sánchez-López, D. Martínez-Martínez, C. López-Cartes, A. Fernández, M. Brizuela, A. García-Luis, J.I. Oñate, J. Vac. Sci. Technol. A 23/4 (2005) 681.

[69] G.S. Kim, S.Y. Lee, Surf. Coat. Technol. 201/7 (2006) 4361.

[70] K. Bobzin, E. Lugscheider, R. Nickel, P. Immich, Materialwiss. Werkstofftech. 37/10 (2006) 833.

[71] W.Y. Yeung, S.N. Dub, R. Wuhrer, Y.V. Milman, Sci. Sinter. 38/3 (2006) 211.

[72] J. Lin, B. Mishra, J.J. Moore, W.D. Sproul, J.A. Rees, Surf. Coat. Technol. 201/16-17 (2007) 6960.

[73] S. Ulrich, H. Holleck, J. Ye, H. Leiste, R. Loos, M. Stüber, P. Pesch, S. Sattel, Thin Solid Films 437/1-2 (2003) 164.

[74] R. Sanjinés, O. Banakh, C. Rojas, P.E. Schmid, F. Lévy, Thin Solid Films 420-421 (2002) 312.

[75] O. Banakh, P.E. Schmid, R. Sanjinés, F. Lévy, Surf. Coat. Technol. 163-164 (2003) 57.

[76] A. Kayani, T.L. Buchanan, M. Kopczyk, C. Collins, J. Lucas, K. Lund, R. Hutchison, P.E. Gannon, M.C. Deibert, R.J. Smith, D.S. Choi, V.I. Gorokhovsky, Surf. Coat. Technol. 201/7 (2006) 4460.

[77] Y. Sun, Y.H. Wang, H.P. Seow, J. Mater. Sci. 39/24 (2004) 7369.

[78] A.E. Reiter, C. Mitterer, B. Sartory, J. Vac. Sci. Technol. A 25/4 (2007) 711.

[79] R. Franz, J. Neidhardt, B. Sartory, R. Kaindl, R. Tessadri, P. Polcik, V.H. Derflinger, C. Mitterer, Tribol. Lett. 23/2 (2006) 101.

[80] J. Romero, M.A. Gómez, J. Esteve, F. Montalà, L. Carreras, M. Grifol, A. Lousa, Thin Solid Films 515/1 (2006) 113.

[81] R. Kaindl, R. Franz, J. Soldan, A. Reiter, P. Polcik, C. Mitterer, B. Sartory, R. Tessadri, M. O'Sullivan, Thin Solid Films 515/4 (2006) 2197.

[82] M. Uchida, N. Nihira, A. Mitsuo, K. Toyoda, K. Kubota, T. Aizawa, Surf. Coat. Technol. 177-178 (2004) 627.

[83] M. Kawate, A.K. Hashimoto, T. Suzuki, Surf. Coat. Technol. 165/2 (2003) 163.

[84] E. Lugscheider, K. Bobzin, T. Hornig, A. Maes, Thin Solid Films 420-421 (2002) 318.

[85] H. Hasegawa, M. Kawate, T. Suzuki, Surf. Coat. Technol. 200/7 (2005) 2409.

[86] H. Hasegawa, T. Suzuki, Surf. Coat. Technol. 188-189 (2004) 234.

[87] A. Kimura, M. Kawate, H. Hasegawa, T. Suzuki, Surf. Coat. Technol. 169-170 (2003) 367.

[88] M. Kawate, A. Kimura, T. Suzuki, J. Vac. Sci. Technol. A 20/2 (2002) 569.

[89] P.E. Gannon, C.T. Tripp, A.K. Knospe, C.V. Ramana, M. Deibert, R.J. Smith, V.I. Gorokhovsky, V. Shutthanandan, D. Gelles, Surf. Coat. Technol. 188-189 (2004) 55.

[90] R.J. Smith, C. Tripp, A. Knospe, C.V. Ramana, A. Kayani, V. Gorokhovsky, V. Shuffhanandan, D.S. Gelles, J. Mater. Eng. Perform. 13/3 (2004) 295.

[91] M. Hirai, Y. Ueno, T. Suzuki, W.H. Jiang, C. Grigoriu, K. Yatsui, Jpn. J. Appl. Phys. Part 1 - Regul. Pap. Short Notes Rev. Pap. 40/2B (2001) 1056.

[92] M. Hirai, T. Suzuki, H. Suematsu, W. Jiang, K. Yatsui, J. Vac. Sci. Technol. A 21/4 (2003) 947.

[93] T. Massalski (Ed.), Binary Alloy Phase Diagrams, ASM International, 1990.

[94] H. Baker (Ed.), ASM Handbook, ASM International, 1992.

[95] J.C. Schuster, H. Nowotny, J. Mater. Sci. 20/8 (1985) 2787.

[96] P. Villars, A. Prince, H. Okamoto (Eds.), Handbook of Ternary Alloy Phase Diagrams, ASM International, 1995.

[97] Y. Makino, Surf. Coat. Technol. 193/1-3 (2005) 185.

[98] P.H. Mayrhofer, unpublished results.

[99] Y. Ide, T. Nakamura, K. Kishitake, in: B. Mishra, C. Yamauchi (Eds.), Second International Conference on Processing Materials for Properties, TMS (The Minerals, Metals & Materials Society), San Francisco, 2000, p. 291.

[100] A.C. Fischer-Cripps, P. Karvánková, S. Vepřek, Surf. Coat. Technol. 200/18-19 (2006) 5645.

[101] R.A. Andrievskii, Russ. Chem. Rev. 66/1 (1997) 57.

[102] M. Odén, J. Almer, G. Håkansson, M. Olsson, Thin Solid Films 377-378 (2000) 407.

[103] R.A. Andrievski, I.A. Anisimova, V.P. Anisimov, Thin Solid Films 205/2 (1991) 171.

[104] D.L. Smith, Thin-Film Deposition: Principles & Practice, McGraw-Hill Inc., New York, 1995.

[105] G. Kienel, K. Röll, Vakuum-Beschichtung 2, VDI-Verlag GmbH, Düsseldorf, 1992.

[106] M. Konuma, Film Deposition by Plasma Techniques, 10, Springer Verlag, Berlin Heidelberg, 1992.

[107] H.-D. Steffens, J. Wilden, Moderne Beschichtungsverfahren, DGM Informationsgesellschaft, Oberursel, 1996.

[108] B. Rother, J. Vetter, Plasma-Beschichtungsverfahren und Hartstoffschichten, Deutscher Verlag für Grundstoffindustrie GmbH, Leipzig, 1992.

[109] R.F. Bunshah (Ed.), Handbook of Hard Coatings: Deposition Technologies, Properties and Applications, Noyes Publications, Norwich, New York, 2001.

[110] C. Engström, T. Berlind, J. Birch, L. Hultman, I.P. Ivanov, S.R. Kirkpatrick, S. Rohde, Vacuum 56/2 (2000) 107.

[111] A. Anders, Ieee Transactions on Plasma Science 31/5 (2003) 1052.

[112] A. Anders, Ieee Transactions on Plasma Science 31/5 (2003) 1060.

[113] R.L. Boxman, S. Goldsmith, Surf. Coat. Technol. 52/1 (1992) 39.

[114] P.H. Mayrhofer, C. Mitterer, L. Hultman, H. Clemens, Prog. Mater. Sci. 51/8 (2006) 1032.

[115] D.M. Mattox, J. Vac. Sci. Technol., A 7/3 (1989) 1105.

[116] J.B. Wachtman, R.A. Haber (Eds.), Ceramic films and coatings, Noyes Publications, Westwood, New Jersey, USA, 1993.

[117] W. Ensinger, Nucl. Instrum. Methods Phys. Res., Sect. B 127-128 (1997) 796.

[118] W. Gissler, H.A. Jehn (Eds.), Advanced Techniques for Surface Engineering, Kluwer Academic Publishers, Dordrecht, The Netherlands, 1992.

[119] J.A. Venables, G.D.T. Spiller, M. Hanbücken, Rep. Prog. Phys. 47/4 (1984) 399.

[120] S. Mahieu, Doctoral thesis, Biaxial alignment in sputter deposited thin films, Solid State Science, Ghent University 2006.

[121] J.E. Greene, Thin Film Nucleation, Growth, & Microstructure Evolution, AVS course at the ICMCTF, San Diego, 2006.

[122] M. Ohring, The material science of thin films, Academic Press, San Diego, California, 1991.

[123] Y. Kajikawa, S. Noda, H. Komiyama, J. Vac. Sci. Technol. A 21/6 (2003) 1943.

[124] E. Kunnen, S. Mangin, V.V. Moshchalkov, Y. Bruynseraede, A. Vantomme, A. Hoser, K. Temst, Thin Solid Films 414/2 (2002) 262.

[125] T. Seppänen, P.O.Å. Persson, L. Hultman, J. Birch, G.Z. Radnóczi, J. Appl. Phys. 97/8 (2005) 083503.

[126] I. Petrov, P.B. Barna, L. Hultman, J.E. Greene, J. Vac. Sci. Technol. A 21/5 (2003) S117.

[127] C.V. Thompson, Annu. Rev. Mater. Sci. 30/1 (2000) 159.

[128] P.B. Barna, M. Adamik, Thin Solid Films 317/1-2 (1998) 27.

[129] M. Zinke-Allmang, Thin Solid Films 346/1-2 (1999) 1.

[130] A.M. Brown, M.F. Ashby, Acta Metall. 28/8 (1980) 1085.

[131] B.A. Movchan, A.V. Demchish, Phys. Met. Metallogr. 28/4 (1969) 83.

[132] J.A. Thornton, J. Vac. Sci. Technol. 11/4 (1974) 666.

[133] J.A. Thornton, J. Vac. Sci. Technol. 12/4 (1975) 830.

[134] J.A. Thornton, Annu. Rev. Mater. Sci. 7 (1977) 239.

[135] J.A. Thornton, J. Vac. Sci. Technol. A 4/6 (1986) 3059.

[136] S. Mahieu, P. Ghekiere, D. Depla, R. De Gryse, Thin Solid Films 515/4 (2006) 1229.

[137] E. Mirica, G. Kowach, H. Du, Cryst. Growth Des. 4/1 (2004) 157.

[138] R. Messier, A.P. Giri, R.A. Roy, J. Vac. Sci. Technol. A 2/2 (1984) 500.

[139] H.T.G. Hentzell, C.R.M. Grovenor, D.A. Smith, J. Vac. Sci. Technol. A 2/2 (1984) 218.

[140] P.J. Kelly, R.D. Arnell, J. Vac. Sci. Technol. A 16/5 (1998) 2858.

[141] M. Adamik, P.B. Barna, I. Tomov, Thin Solid Films 317/1-2 (1998) 64.

[142] P.B. Barna, M. Adamik, in: Y. Pauleau, P.B. Barna (Eds.), NATO Advanced Research workshop on Protective Coatings and Thin Films: Synthesis, Characterization and Applications, Kluwer Academic Publishers, Alvor, Portugal, 1996.

[143] W.H. Bragg, W.L. Bragg, Proceedings of the Royal Society of London. Series A, Containing Papers of a Mathematical and Physical Character 88/605 (1913) 428.

[144] M. Birkholz, Thin Film Analysis by X-Ray Scattering, Wiley-VCH Verlag GmbH & Co. KGaA, Weinheim, 2006.

[145] B.D. Cullity, Elements of X-Ray Diffraction, Addison-Wesley Publishing Company Inc., 1978.

[146] P.v.d. Sluis, J. Phys. D: Appl. Phys. 26/4A (1993) A188.

[147] D.B. Williams, C.B. Carter, Transmission Electron Microscopy (1 Basics), Springer Science+Business Media Inc., New York, 1996.

[148] D.B. Williams, C.B. Carter, Transmission Electron Microscopy (2 Diffraction), Springer Science+Business Media Inc., New York, 1996.

[149] D.B. Williams, C.B. Carter, Transmission Electron Microscopy (3 Imaging), Springer Science+Business Media Inc., New York, 1996.

[150] D.B. Williams, C.B. Carter, Transmission Electron Microscopy (4 Spectrometry), Springer Science+Business Media Inc., New York, 1996.

[151] P. Goodhew, D. Brook, B. Tanovic, A. Green, I. Jones, www.matter.org.uk/tem/, The University of Liverpool, 2000.

[152] P.O.Å. Persson, lecture notes of the course 'Transmission Electron Microscopy', Linköping, Sweden, 2006.

[153] T. Chudoba, in: A. Cavaleiro, J.T.M. De Hosson (Eds.), Nanostructured Coatings, Springer Science+Business Media, LLC, New York, 2006.

[154] E. Arzt, Acta Mater. 46/16 (1998) 5611.

[155] P. Haasen, Physical Metallurgy, Cambridge University Press, Cambridge, 1996.

[156] W.D. Callister, Materials Science and Engineering - An Introduction, John Wiley & Sons, Inc. , New York, 2003.

[157] R.W. Cahn, P. Haasen, Physical Metallurgy, 1-3, North-Holland, Amsterdam, 1996.

[158] G. Gottstein, Physikalische Grundlagen der Materialkunde, Springer Verlag, Berlin, 2007.

[159] D.A. Porter, K.E. Easterling, Phase Transformations in Metals and Alloys, CRC Press, 1992.

[160] A.C. Fischer-Cripps, Nanoindentation, Springer Science+Business Media LLC, New York, 2004.

[161] DIN EN ISO 14577-1, 2003.

[162] DIN EN ISO 14577-2, 2003.

[163] DIN EN ISO 14577-3, 2003.

[164] W.C. Oliver, G.M. Pharr, J. Mater. Res. 7/6 (1992) 1564.

[165] M.E. Brown (Ed.), Handbook of Thermal Analysis and Calorimetry, Elsevier Science B.V., Amsterdam, 1998.

[166] F. Spaepen, C.V. Thompson, Appl. Surf. Sci. 38/1-4 (1989) 1.

[167] C. Michaelsen, K. Barmak, T.P. Weihs, J. Phys. D-Appl. Phys. 30/23 (1997) 3167.

[168] H. Willmann, P.H. Mayrhofer, P.O.Å. Persson, A.E. Reiter, L. Hultman, C. Mitterer, Scr. Mater. 54/11 (2006) 1847.

[169] W.F. Hemminger, H.K. Cammenga, Methoden der Thermischen Analyse, Springer Verlag, Berlin, 1989.

[170] G.W.H. Höhne, W. Hemminger, H.-J. Flammersheim, Differential Scanning Calorimetry - An Introduction for Practitioners, Springer Verlag, Berlin, 1996.

[171] J. Rouquerol, P. Boivinet, in: R.C. Mackenzie (Ed.), Differential Thermal Analysis, vol. 2, Academic Press Inc., London, 1972, p. 23.

[172] J. Opfermann, J. Therm. Anal. Cal. 60/2 (2000) 641.

[173] H.E. Kissinger, Anal. Chem. 29/11 (1957) 1702.

[174] M.E. Brown, M. Maciejewski, S. Vyazovkin, R. Nomen, J. Sempere, A. Burnham, J. Opfermann, R. Strey, H.L. Anderson, A. Kemmler, R. Keuleers, J. Janssens, H.O. Desseyn, C.R. Li, T.B. Tang, B. Roduit, J. Malek, T. Mitsuhashi, Thermochim. Acta 355/1-2 (2000) 125.

[175] M. Maciejewski, Thermochim. Acta 355/1-2 (2000) 145.

[176] S. Vyazovkin, Thermochim. Acta 355/1-2 (2000) 155.

[177] A.K. Burnham, Thermochim. Acta 355/1-2 (2000) 165.

[178] B. Roduit, Thermochim. Acta 355/1-2 (2000) 171.

[179] J. Vázquez, P.L. López-Alemany, P. Villares, R. Jiménez-Garay, J. Phys. Chem. Solids 61/4 (2000) 493.

[180] P.H. Mayrhofer, H. Willmann, C. Mitterer, Thin Solid Films 440/1-2 (2003) 174.

[181] P.H. Mayrhofer, A. Horling, L. Karlsson, J. Sjolen, T. Larsson, C. Mitterer, L. Hultman, Appl. Phys. Lett. 83/10 (2003) 2049.

[182] E. Kaisersberger, E. Post, Thermochim. Acta 324/1-2 (1998) 197.

10 Publications

Papers included in this thesis and my contributions* to them

I. Thermal Stability of Al-Cr-N Hard Coatings

H. Willmann, P.H. Mayrhofer, P.O.Å. Persson, A.E. Reiter, L. Hultman, C. Mitterer

Published in Scripta Materialia 54 (2006) 1847-1851

II. Hardness and phase stability of Al-Cr-N hard coatings under thermal load

H. Willmann, P.H. Mayrhofer, L. Hultman, C. Mitterer

Submitted to Journal of Vacuum Science & Technology A – Vacuum, Surfaces, and Films

III. Single-crystal growth of NaCl-structure Al-Cr-N thin films on MgO(001) by magnetron sputter epitaxy

H. Willmann, M. Beckers, F. Giuliani, J. Birch, P.H. Mayrhofer, C. Mitterer, L. Hultman

Submitted to Scripta Materialia

IV. Epitaxial growth of Al-Cr-N thin films on MgO(111)

H. Willmann, M. Beckers, J. Birch, P.H. Mayrhofer, C. Mitterer, L. Hultman

Submitted to Thin Solid Films

	Conception and planning	Experiments	Analysis and Interpretation	Manuscript preparation
Paper I	100	100	90	100
Paper II	100	100	100	100
Paper III	75	65	65	100
Paper IV	75	65	65	100

* supervision and iteration work of the manuscripts by the co-authors is not included

Publications related to this thesis

V. Thermal Stability and Age-Hardening of Al-Cr-N Hard Coatings

H. Willmann, P.H. Mayrhofer, L. Hultman, C. Mitterer

Bodycote 10th Anniversary Prize Paper Competition Finalist 2006

Published in International Heat Treatment and Surface Engineering 1/2 (2007) 75-79

VI. Structure Evolution of Cr-Al-N Hard Coatings

P.H. Mayrhofer, H. Willmann, A.E. Reiter

Published in the Proceedings of the 49th SVC Annual Technical Conference, Society of Vacuum Coaters, Washington, 2006, p. 575.

VII. Thermal Decomposition Routes of CrN Hard Coatings – Comparison between Reactive Arc Evaporation and Magnetron Sputtering

W. Ernst, J. Neidhardt, H. Willmann, B. Sartory, P.H. Mayrhofer, C. Mitterer

Manuscript in final preparation

VIII. Thermal decomposition of CrN hard coatings

W. Ernst

Diploma Thesis, University of Leoben 2006

Publication I

Thermal Stability of Al-Cr-N Hard Coatings

H. Willmann

P.H. Mayrhofer

P.O.Å. Persson

A.E. Reiter

L. Hultman

C. Mitterer

Published in

Scripta Materialia 54 (2006) 1847-1841

Thermal Stability of Al-Cr-N Hard Coatings

H. Willmann[1,2], P.H. Mayrhofer[3,4], P.O.Å. Persson[2,5], A.E. Reiter[6], L. Hultman[2], C. Mitterer[3,7]

[1] Materials Center Leoben, 8700 Leoben, Austria
[2] IFM Material Physics, Division of Thin Film Physics, Linköping University, 58183 Linköping, Sweden
[3] Department of Physical Metallurgy and Materials Testing, University of Leoben, 8700 Leoben, Austria
[4] Materials Chemistry, RWTH-Aachen, 52074 Aachen, Germany
[5] FEI Company, 5651 GG Eindhoven, The Netherlands
[6] Balzers Ltd., 9496 Balzers, Liechtenstein
[7] Christian Doppler Laboratory for Advanced Hard Coatings, University of Leoben, 8700 Leoben, Austria

Keywords: Differential scanning calorimetry, Thermogravimetric analysis, Analytical electron microscopy, Decomposition, AlCrN

Abstract

Heat treatment of arc evaporated cubic $Al_{0.7}Cr_{0.3}N$ hard coatings in Ar up to 1450 °C causes precipitation of AlN. The Cr-enriched matrix transforms into Cr via Cr_2N under N_2 release. These reactions are investigated by simultaneous thermal analysis, mass spectrometry, X-ray diffraction, and analytical transmission electron microscopy.

Introduction

Hard protective coatings are widely used to expand the usability of cutting- and metal forming tools. Important requirements are sufficient hardness, high wear-, corrosion-, and oxidation-resistance as well as good thermal stability. In modern cutting applications such as high-speed and/or dry cutting the temperature at the cutting edge can exceed 1000 °C [1,2]. Consequently, the applied protective coating must be capable of withstanding these extreme conditions. $Al_xCr_{1-x}N$ provides high hardness [3-12], superior oxidation resistance [11-15], and good tribological behavior [9-11,16]. These properties

depend on chemical composition and microstructure [8,9,14,17] and when optimized, excellent performance in cutting tests can be obtained [17]. While the oxidation resistance is discussed intensively in literature [11-15,17], the temperature dependent structural and compositional evolution is essentially unexplored. Two stability-related questions are discussed in literature. The first addresses the limit of Al solubility in the face-centered cubic (fcc) CrN phase [9,17-20], the second deals with the onset of decomposition of the supersaturated phase into its stable constituents [13,14,16,17].

Several deposition techniques and setups are reported for synthesizing $Al_xCr_{1-x}N$ coatings [6,9,11,12,17,19]. Recent results conclude improved mechanical and thermal properties for increasing Al content in the fcc-structure (up to $x = 0.75$) [12-14,17]. Exceeding the solubility limit for Al results in hexagonal wurtzite type (w) structure [17,19,20] and the mechanical properties degrade [12,17]. Consequently, $Al_{0.7}Cr_{0.3}N$ coatings - which have been shown to perform excellent in cutting tests [17] - are the focus of this work.

Here, we use a combination of differential scanning calorimetry (DSC), thermal gravimetric analysis (TGA) and mass spectrometry (MS), to investigate the decomposition process of supersaturated cubic $Al_{0.7}Cr_{0.3}N$ coatings in detail. X-ray diffraction (XRD) and scanning transmission electron microscopy (STEM) in combination with energy dispersive X-ray analysis (EDX) were utilized to attribute the observed DSC, TGA, and MS results. The complex decomposition process of supersaturated $Al_{0.7}Cr_{0.3}N$ coatings is described.

Experimental details

The depositions were carried out using a Balzers Rapid Coating System (RCS), described in ref. 17. The equipment was operated in the cathodic arc evaporation setup with four metallic compound targets (Al/Cr at% ratio = 70/30). The target current was 140 A, the base pressure was below $1x10^{-3}$ Pa, and the nitrogen pressure during the reactive deposition process was 3.5 Pa. A bias voltage of -40 V was applied to the substrates and their temperature was kept at 500 °C. Two-fold substrate rotation [17] was used to obtain uniform film properties. The substrates were cleaned by plasma etching prior to deposition.

A Netzsch STA 409C instrument with a quadrupole mass spectrometer (QMS) connected through a skimmer coupling system was used for DSC, TGA, and MS measurements as well as for annealing samples for subsequent XRD and TEM investigations. To avoid the influence of the substrate material in the DSC measurements, the coatings were chemically removed from their low-alloyed steel substrates using a 10 mol% nitric acid. After filtering and cleaning, the film material was mechanically ground to a fine powder whereof ~30 mg were used for each measurement. Dynamical heating up to 1450 °C was performed in a flow of Ar (50 sccm, 99.999% purity) using a heating rate of 20 K/min. The DSC system was calibrated in temperature and sensitivity by the pure elements Sn, Zn, Al, Ag, and Au. For detecting N_2, the atomic mass unit 28 was monitored by the QMS.

XRD measurements of as-deposited and annealed samples were carried out on a Siemens D500 diffractometer in the Bragg-Brentano (θ-2θ) geometry using Cu-K_α radiation. The electron microscopy investigations were obtained from plan-view samples deposited on single-crystal sapphire discs (Al_2O_3, Ø 3 mm × 0.1 mm, (0001) oriented). Due to the high annealing temperatures (T_a), sapphire was chosen to avoid interdiffusion of substrate and film material. STEM was performed on a Tecnai G^2 TF 20 UT microscope operating at 200 keV. The probe size used was <1 nm and the images were recorded with a high-angle annular dark field (HAADF) detector. A camera length of 90 mm was used to promote preferential mass-thickness contrast and to reduce the influence of diffraction contrast. Chemical compositions were measured with energy dispersive X-ray analysis (EDX) during STEM investigations.

Results and Discussion

EDX measurements showed that the chemical composition of the as-deposited coatings was $Al_{0.7}Cr_{0.3}N$, corresponding to the Al/Cr ratio in the target.

Figure 1a shows a typical DSC signal and the mass loss for $Al_{0.7}Cr_{0.3}N$ as a function of the annealing temperature. The monitored N_2 signal of the MS measurement is presented in Fig. 1b. This signal starts to deviate from the baseline at T_a ~ 925 °C where also the onset of sample mass loss can be detected in TGA. During the heat treatment up to

1450 °C, several reactions in the film material are superimposing indicated by the overlapping reaction peaks in the DSC and MS signal as well as by the changing slopes of the TGA curve. As the release of nitrogen is directly connected to mass loss, any change in MS signal corresponds to a change in TGA and vice versa. Both measurement techniques indicate an incomplete decomposition process even at 1450 °C, i.e. the MS signal does not reach the baseline, and the TGA signal is not horizontal.

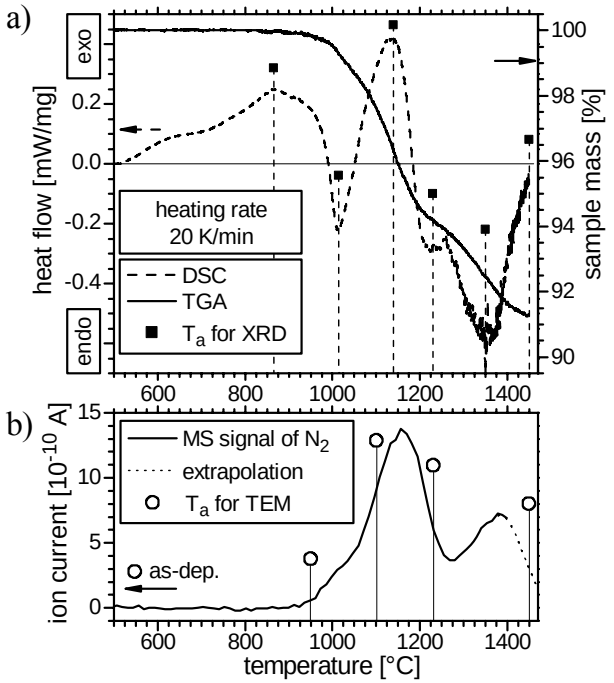

Fig. 1. a) DSC and TGA of $Al_{0.7}Cr_{0.3}N$ in inert atmosphere with indicated annealing temperatures for XRD measurements. b) Corresponding MS signal with marked temperatures for TEM investigations.

Various exothermic and endothermic reactions can correspondingly be detected by DSC up to 1450 °C (Fig. 1a). The first exothermic reaction with a peak maximum at ~625 °C (onset slightly higher than the deposition temperature), is related to recovery processes [21,22,23]. Deposition-induced lattice defects, responsible for a compressive residual stress state, anneal out due to increased diffusivity at elevated temperatures.

XRD investigations were performed on samples annealed at temperatures indicated in Fig. 1a in order to explain the reactions detected via DSC, TGA, and MS. Figure 2a shows diffractograms of these specimens including positions for fcc-AlCrN, located

between fcc-CrN and fcc-AlN, as well as w-AlN, hexagonal (hex) Cr_2N, and body-centered cubic (bcc) Cr. The lattice parameter for Cr_2N is between the values given by different JCPDS-files [24]. For the sample annealed at 865 °C the (200) and (220) AlCrN matrix peaks show a reduced full width at half maximum of ~23% confirming the above mentioned recovery effects during annealing. The thermal stability range of the phases present during decomposition of $Al_{0.7}Cr_{0.3}N$ is schematically summarized in Fig. 2b.

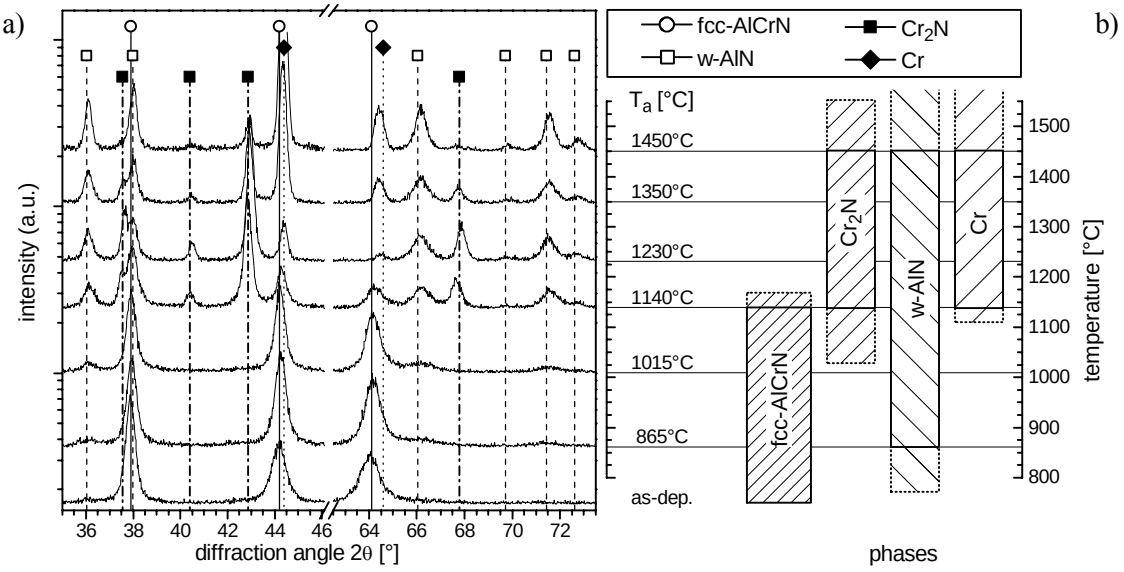

Fig. 2. a) XRD evolution of an $Al_{0.7}Cr_{0.3}N$ film with annealing temperature. b) Bars represent detected phases, dashed extensions indicate the estimated existence range of the occurring phases.

For detailed investigation of the as-deposited structure, selected area electron diffraction (SAED) was performed on a plan-view sample. Figure 3a shows the obtained STEM image with minor variations in contrast resulting from different orientated grains. The contrast for the HAADF images in this work is optimized for changes in mass and thickness whereas these parameters are almost uniform for this sample. The low contrast indicates negligible contribution due to diffraction even at the most extreme conditions for the used parameters. The corresponding SAED pattern is presented in Fig. 3b. In addition to the diffraction rings from the fcc-structured polycrystalline AlCrN matrix, weak w-AlN reflexes can be detected (Fig. 3b). This is not confirmed by XRD results (Fig. 2a), which show no w-AlN in the as-deposited state. It has been reported [25] that different substrate

materials can influence the formed structure of AlCrN during deposition. However, grazing incidence XRD of the coating on sapphire shows a diffractogram comparable to the one in Fig. 2a, i.e. also without w-AlN reflexes. SAED of a coating on cemented carbide substrate shows pure cubic structure. We therefore conclude that small amounts of w-AlN phase (below the detection limit of XRD) are present in the as-deposited coatings on sapphire.

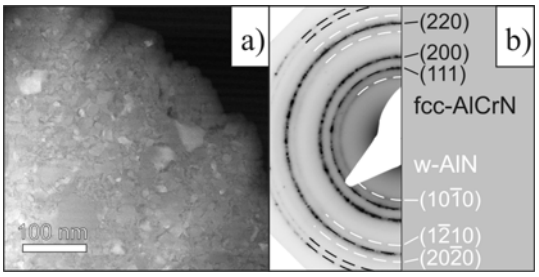

Fig. 3. a) STEM plan-view image (HAADF) of $Al_{0.7}Cr_{0.3}N$ in the as-deposited state; grains appear in a uniform grey tone, a thickness induced contrast-gradient is superposed. b) SEAD pattern with standard diffraction rings for fcc-AlCrN and w-AlN.

For T_a = 865 °C, small fractions of w-AlN can be detected even by XRD, and with higher T_a their peak intensity increases continuously (Fig. 2a). The corresponding nucleation and growth processes result in an exothermic contribution to the DSC signal, represented by a broad peak with a detected maximum at ~875 °C (Fig. 1a). It is reasonable to estimate the real peak temperature at temperatures above 900 °C since a strong endothermic contribution related to decomposition is superimposed at T_a > 925 °C. Simultaneously, the XRD patterns show a reduction in the AlCrN matrix peak intensity for increasing T_a (Fig. 2a). The decrease is small for 865 °C < T_a < 1015 °C, becomes pronounced for higher temperatures and for $T_a \geq$ 1230 °C fcc-AlCrN is below the detection limit. The formation of AlN precipitates leads to a gradual Cr enrichment of the matrix. After obtaining a sufficient driving force from a combination of temperature and chemical composition of the matrix, release of nitrogen is initiated (see the MS signal in Fig. 1b) and consequently the sample mass decreases (Fig. 1a). This decomposition of the material results in an endothermic reaction during DSC measurement with a maximum slightly above 1000 °C.

The reduction of N-content in the matrix causes also a transformation into hex-Cr_2N. For the ideal case, without any remaining Al in the matrix, it is proposed that the stoichiometry of fcc-CrN approaches $CrN_{0.5}$ before transforming into hex-Cr_2N. A corresponding phase transformation causes an exothermic contribution to the DSC measurement of $Al_{0.7}Cr_{0.3}N$, which is now depleted in N. Furthermore also the slope of the TGA signal changes, indicating a different N-release rate compared to the cubic structure. During XRD investigations Cr_2N can be detected in samples annealed between 1140 and 1450 °C. At atmospheric pressure, depending on ambient atmosphere, bulk Cr_2N starts to decompose into bcc-Cr and N_2 gas at temperatures below 1000 °C [26]. This predicted decomposition can first be seen in our material at 1140 °C. The decomposition is visible during DSC as a pronounced endothermic reaction (see Fig. 1a, reaction peak maximum at ~1350 °C) and the reduced mass-loss slope in the TGA signal. Additionally, an exothermic contribution to the DSC scan is caused by the occurring transformation from hex into bcc lattice. In the temperature range 1000 – 1450 °C several endothermic and exothermic reactions are superimposing, and hence the separation of individual contributions to the DSC signal is difficult. Figure 1b indicates the N-release of the Cr_2N decomposition by the MS peak maximum at ~1380 °C. The maximum intensity of Cr_2N during XRD investigations is obtained for samples annealed at 1230 °C. The bcc-Cr phase can be observed for $T_a \geq 1140$ °C as a shoulder of the matrix peak at $2\theta \sim 64.6°$. After annealing the films at 1450 °C, mainly w-AlN and bcc-Cr with small fractions of hex-Cr_2N (Fig. 2a) are present. The latter explains the uncompleted N-release for $T_a = 1450$ °C as detected by TGA. This is also proven by MS measurements. Because of the high thermal stability of AlN (~2800 °C), we propose that the reduction in sample mass is due to the loss of chromium-bonded nitrogen. Our results indicate that this loss is completed at ~1550 °C for the used annealing conditions (see Fig. 2b).

To further verify the obtained results of DSC, TGA, MS, and XRD, the microstructural changes of the material were investigated by TEM for samples annealed at 950, 1100, 1230, and 1450 °C (indicated in Fig. 1b). The obtained STEM images are presented in Fig. 4a-d, respectively. Assuming only a minor change in thickness across the investigated sample area, the image contrast may be attributed to pure mass (density) changes, where low atomic mass appears dark.

The sample annealed at 950 °C (Fig. 4a) shows precipitates (dark regions), next to coarsened matrix grains, along triple junctions and at grain boundaries. Chemical analysis by EDX confirms that these are composed of Al and N. The surrounding areas of these AlN precipitates are consequently Cr enriched and appear bright in Fig. 4a. The bright tissue is generated from sites of early decomposition, most probably from grain and phase boundaries. This also corresponds well with the MS measurement, where a small N-release (maximum at T_a ~ 1015 °C) slightly before the main peak (maximum at T_a ~ 1140 °C) suggests that this phase separation process starts with weakly bonded nitrogen leaving from the grain and phase boundaries.

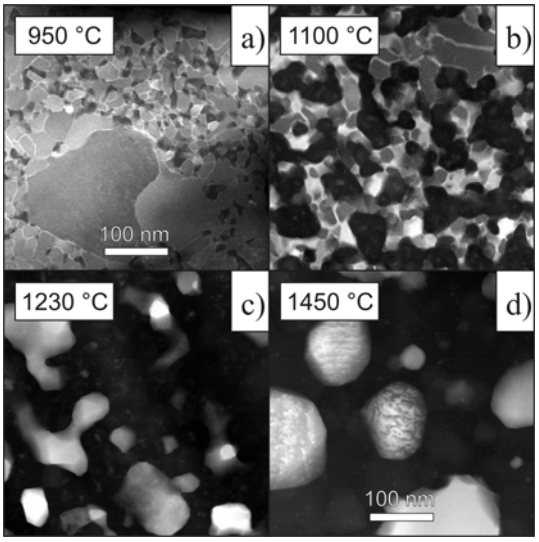

Fig. 4. STEM plan view images (HAADF) of $Al_{0.7}Cr_{0.3}N$ after annealing at a) 950 °C, b) 1100 °C, c) 1230 °C, and d) 1450 °C.

The sample annealed at 1100 °C (Fig. 4b) shows an increase in volume fraction of AlN precipitates. The bright tissue is more pronounced and the Cr-enriched areas, which form next to these precipitates, can be verified by EDX to have the chemical composition of Cr_2N. This is in agreement to XRD where Cr_2N is detected for samples annealed at $T_a \geq 1140$ °C.

Increasing the annealing temperature to 1230 °C (Fig. 4c) generates a microstructure where w-AlN grains almost completely encapsulate the initial matrix grains. Growth and increase in volume fraction of these AlN precipitates is the main reason for the more pronounced w-AlN XRD peaks (see Fig. 2a). EDX analysis confirms the described

decomposition process of the matrix into Cr via Cr_2N. The intermediate stage of this reaction at 1230 °C can be seen in Fig. 4c, where Cr and Cr_2N appear with different contrasts.

In Fig. 4d (T_a = 1450 °C) spherically shaped grains up to 0.5 µm in size embedded in AlN are visible. The coarsening is driven by the potential for the system to reduce its total interfacial energy which is measured as heat release in the DSC. The presence of Cr_2N grains at this temperature, as indicated by XRD, could be confirmed by TEM/EDX investigations. An EDX line scan across the grains displayed in Fig. 4d is shown in Fig. 5, including the distribution of the elements Al, Cr, and N and their fits. The signal labeled $N^{(Cr)}$ represents the nitrogen bonded to Cr under the assumption of stoichiometric AlN presence. The resulting ratio of Cr to $N^{(Cr)}$ equals 2:1 which corresponds to a chemical composition of Cr_2N. The measurement indicates an overlap of two AlN and Cr_2N grains. A schematic illustration of the probed volume is included in Fig. 5.

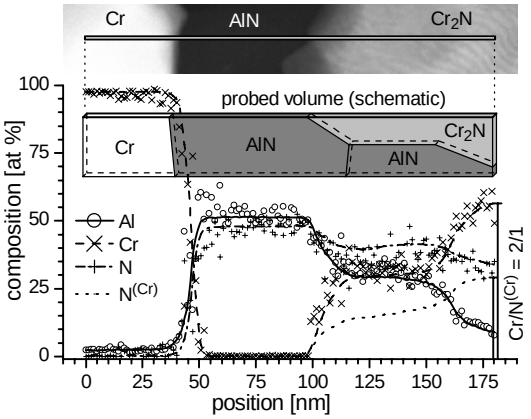

Fig. 5. EDX line scan at an $Al_{0.7}Cr_{0.3}N$ sample annealed at 1450 °C. Fitted curves for Al, Cr, and N are provided. $N^{(Cr)}$ shows N bonded to Cr. The schematic drawing indicates the probed volume under the line scan.

Conclusions

The investigated arc evaporated $Al_{0.7}Cr_{0.3}N$ hard coatings are supersaturated fcc-structured in the as-deposited state. During annealing in inert atmosphere up to 1450 °C with 20 K/min the material undergoes decomposition with several superimposing reactions. After recovery which occurs at temperatures slightly above the deposition temperature, formation and growth of w-AlN precipitates at grain boundaries and triple

junctions can be seen, and hence the matrix becomes Cr-enriched. Further annealing causes N-loss (for T_a > 925 °C) and subsequently transformation to Cr via the intermediate step of Cr_2N, which is completed at 1550 °C under the used conditions. Fcc-structured AlCrN matrix can be detected during annealing up to 1140 °C, what indicates a stabilization of the Cr-N bonds by Al. At 1450 °C the structure is mainly composed of bcc-Cr and w-AlN with minor fractions of hex-Cr_2N left.

Our results clearly demonstrate the potential of AlCrN coatings for ageing processes with precipitations, which offer explanations for the superior mechanical properties of this material even at high temperatures.

Acknowledgements

The authors want to thank Dr. Jörg Neidhardt (Christian Doppler Laboratory for Advanced Hard Coatings at the University of Leoben) for the support in sample deposition. We are also grateful to Jens Emmerlich (IFM – Thin Film Physics, Linköping University) for the support in the gracing incidence XRD measurement. H.W. is grateful for the support of his stay in Linköping by the Marie Curie fellowship. P.H.M is supported by the Erwin Schrödinger Program (project J2469-N02) of the Austrian Science Fund. L.H. acknowledges support from the Swedish Research Council (VR). The work done in Leoben was supported by the Technologie Impulse G.m.b.H within the framework of the K-plus competence center program and by the Christian Doppler Society.

References

[1] Nomura T. Moriguchi H. Tsuda K. Isobe K. Ikegaya A. Moriyama K. Int. J. Refract. Met. Hard Mat. 1999;17:397.

[2] Modern Metal Cutting. Sweden: Tofters Tryckeri AB; 1994. p. I-32.

[3] Wuhrer R. Yeung WY. Scr. Mater. 2004;50:1461.

[4] Knotek O. Atzor M. Barimani A. Jungblut F. Surf. Coat. Technol. 1990;42:21.

[5] Kawate M. Kimura A. Suzuki T. J. Vac. Sci. Technol. A 2002;20(2):569.

[6] Ulrich S. Holleck H. Ye J. Leiste H. Loos R. Stüber M. Pesch P. Sattel S. Thin Solid Films. 2003;437:164.

[7] Lugscheider E. Bobzin K. Hornig T. Maes M. Thin Solid Films 2002;420-421;318

[8] Hasegawa H. Suzuki T. Surf. Coat. Technol. 2004;188-189:234.

[9] Ide Y. Nakamura T. Kishitake K. Second International Conference on Processing Materials for Properties. The Minerals, Metals & Materials Society. San Francisco, California. 2000. p. 291.

[10] Okumiya M. Griepentrog M. Surf. Coat. Technol. 1999;112:123.

[11] Vetter J. Lugscheider E. Guerreiro SS. Surf. Coat. Technol. 1998;98:1233.

[12] Hirai M. Ueno Y. Suzuki T. Jiang W. Grigoriu C. Yatsui K. Jpn. J. Appl. Phys. 2001;40:1056.

[13] Kawate M. Hashimoto AK. Suzuki T. Surf. Coat. Technol. 2003;165:163.

[14] Banakh O. Schmid PE. Sanjinés R. Lévy F. Surf. Coat. Technol. 2003;163-164:57.

[15] Smith RJ. Tripp C. Knospe A. Ramana CV. Kayani A. Gorokhovsky V. Shutthanandan V. Gelles DS. J. Mater. Eng. Perform. 2004;13(3):295.

[16] Lugscheider E. Bobzin K. Bärwulf S. Hornig T. Surf. Coat. Technol. 2000;133-134:540.

[17] Reiter AE. Derflinger VH. Hanselmann B. Bachmann T. Sartory B. Surf. Coat. Technol. 2005;200:2114.

[18] Kimura A. Kawate M. Hasegawa H. Suzuki T. Surf. Coat. Technol. 2003;169-170:367.

[19] Makino Y. Nogi K. Surf. Coat. Technol. 1998;98:1008.

[20] Sugishima A. Kajioka H. Makino Y. Surf. Coat. Technol. 1997;97:590.

[21] Mayrhofer PH. Hörling A. Karlsson L. Sjölén J. Larsson T. Mitterer C. Hultman L. Appl. Phys. Lett. 2003;83:2049.

[22] Mayrhofer PH. Clemens H. Mitterer C. Z. Metallk. 2005;5:468.

[23] Mayrhofer PH. Mitterer C. Hultman L. Clemens H. Prog. Mater. Sci. accepted

[24] Powder Diffraction File (Card 11-0065 for fcc-CrN, Card 46-1200 for fcc-AlN, Card 25-1133 for w-AlN, Card 35-0803 and 3-1191 for hex-Cr_2N, Card 06-0694 for bcc-Cr). International Center for Diffraction Data, JCPDF – ICDD 1998.

[25] Sun Y. Wang H. Seow HP. J. Mater. Sci. 2004;39:7369.

[26] Gmelins Handbuch der anorganischen Chemie. Weinheim: Verlag Chemie GmbH; 1962. p.160.

Publication II

Hardness and phase stability of Al-Cr-N hard coatings under thermal load

H. Willmann

P.H. Mayrhofer

L. Hultman

C. Mitterer

Submitted to

Journal of Vacuum Science & Technology A – Vacuum, Surfaces, and Films

Hardness and phase stability of Al-Cr-N hard coatings under thermal load

H. Willmann[1,2)], P.H. Mayrhofer[3)], L. Hultman[2)], C. Mitterer[4)]

[1)] Materials Center Leoben, 8700 Leoben, Austria
[2)] IFM Material Physics, Division of Thin Film Physics, Linköping University, 58183 Linköping, Sweden
[3)] Department of Physical Metallurgy and Materials Testing, University of Leoben, 8700 Leoben, Austria
[4)] Christian Doppler Laboratory for Advanced Hard Coatings, at the Department of Physical Metallurgy and Materials Testing, University of Leoben, 8700 Leoben, Austria

Abstract

Microstructural evolution of arc evaporated single-phase cubic $Al_{0.56}Cr_{0.44}N$ and $Al_{0.68}Cr_{0.32}N$ coatings has been investigated during annealing up to 1450 °C in Ar, N_2, and synthetic air. A combination of differential scanning calorimetry, thermogravimetric analysis and mass spectrometry is used to determine reactions of the material during in-situ annealing. X-ray diffraction and analytical transmission electron microscopy studies show that wurtzite type AlN precipitation in $Al_{0.68}Cr_{0.32}N$ coatings at annealing temperatures $T_a \geq 650$ °C is responsible for a hardness increase from the as-deposited value of ~30 GPa to a maximum of ~31.6 GPa at $T_a \sim 725$ °C. At higher temperatures the hardness decreases to ~27.5 GPa with $T_a = 900$ °C. The lower Al containing coating ($Al_{0.56}Cr_{0.44}N$) maintains its as-deposited hardness value of ~30 GPa during annealing up to 1000 °C, however, without AlN precipitation. All investigated $Al_xCr_{1-x}N$ coatings demonstrate high thermal stability and excellent hot hardness due to solid solution and precipitation hardening.

Keywords: precipitation hardening, age-hardening, AlN, AlCrN, CrAlN, thermal analysis

Introduction

CrN based coatings are well established for industrial applications. The addition of Al in a metastable solid solution $Al_xCr_{1-x}N$ has been shown to combine an improved

oxidation resistance with high hardness and good thermal stability.[1-10] Although AlN is hexagonal (wurtzite type, B4 structure) in its stable modification (w-AlN), PVD techniques with limited kinetics[11,12] allow the incorporation of a certain mole fraction in face-centered cubic (fcc) NaCl-structure (B1) $Al_xCr_{1-x}N$.[1-10,13,14] Calculations by the band parameters method based on the concept of localized electron theory results in a maximum metastable solubility of 77.2% AlN in cubic CrN.[15] Exceeding this limit in the Al-Cr-N system causes the formation of $Al_xCr_{1-x}N$ in the hexagonal wurtzite-type structure.[10,13,14] Different techniques are reported for synthesizing such ternary compounds,[1-10,13,14] where arc evaporation as a common industrial process was chosen in this work.

Apart from alloying to modify the bonding structure, several other mechanisms are influencing the hardness of binary and ternary systems.[11] An increased material hardness due to hindrance in dislocation movement can be achieved by varying deposition parameters (e.g. particle flux, ion energy, deposition temperature) to increase the defect density or reduce grain size. However, recovery processes and recrystallization at elevated temperatures can degrade this contribution. Another approach for higher hardness is the implementation of obstacles for dislocation glide in the film. This can be achieved during deposition by a two-phase structure resulting in dispersion hardening or with a post-deposition annealing treatment to form precipitates. Transformation processes of supersaturated coatings with resulting obstacles for dislocation glide can effectively suppress or even surmount the hardness loss due to recovery processes during annealing.[16] Correspondingly, precipitation also influences the bonding characteristics due to a resulting chemical change in the remaining matrix. For modern hard coatings, a combination of these mechanisms is utilized to achieve the optimum performance,[11] but the crucial point in high-temperature applications is the resistance of the various mechanisms against thermal loads.

Recently we reported that $Al_xCr_{1-x}N$ coatings, with an AlN mole fraction of $x \sim 0.7$, exhibit precipitation of w-AlN for post-deposition annealing temperatures (T_a) above 650 °C.[17] Due to this phase separation process, the remaining matrix becomes Cr-enriched and at $T_a \geq 975$ °C breaking of the Cr-N bonds within this remaining matrix causes nitrogen loss and, thus, the transformation into Cr via the intermediate step of Cr_2N.[17] Detailed investigations of the onset-temperature for phase decomposition and the

mechanisms of N-loss in $Al_xCr_{1-x}N$ are necessary, especially with respect to the ambient atmosphere. In order to investigate reactions and the mechanisms behind the phase transformations, we use single-phase cubic $Al_xCr_{1-x}N$ coatings with AlN mole fractions close to the metastable solubility limit and films with lower AlN contents. Annealing treatments of these films are conducted in Ar, N_2, and synthetic air up to 1450 °C. Finally, we determine the hardness over annealing temperature for the resulting coatings up to 900 °C.

Experimental details

Mirror-polished cemented carbide (cc) inserts (THM 08) and low-alloyed steel substrates were coated via cathodic arc evaporation in a commercial deposition system (Balzers Rapid Coating System, RCS). For the preparation of $Al_xCr_{1-x}N$ coatings with two different compositions, four arc sources were equipped with metallic compound targets having Al/Cr ratios of 60/40 and 70/30 operated with a current of 140 A each. The base pressure in the chamber was below 1×10^{-3} Pa and the nitrogen pressure during deposition was 3.5 Pa. The substrates were plasma-etched prior to the deposition which was conducted with a twofold planetary substrate rotation. During deposition, a bias potential of -40 V was applied and the substrate temperature was kept constant at 500 °C. The deposition rate was ~55 nm/min and with the deposition times of 90 min for the 60/40 and 45 min for the 70/30 configuration, film thicknesses of ~5.0 µm and ~2.4 µm were achieved, respectively.

The film compositions were analyzed by Rutherford backscattering spectroscopy (RBS) and time-of-flight elastic recoil detection analysis (TOF-ERDA). The RBS measurements were performed using a 2 MeV $^4He^+$ beam at an incidence angle to the substrate normal of 7° and a scattering angle of 167°. The obtained data were fitted with the SIMNRA simulation code.[18] The ERDA measurements were performed using an $^{127}I^{9+}$ ion beam (40 MeV) and a collection angle of the recoiled atoms of 45° relative to the incoming beam direction. A detailed description of the used TOF setup is given in Ref. 19. The resulting time-of-flight over recoil energy spectra were transformed to elemental depth

profiles using the CONTES code.[20] Resolutions for the two techniques were ±1% for the Al/Cr ratio (RBS) and the stoichiometry of the nitrides (TOF-ERDA).

Coatings on cemented carbide substrates were annealed under Ar atmosphere in a Nabertherm N117HR furnace for 60 min at temperatures between 500 and 1000 °C in order to perform structural investigations and indentation experiments as a function of T_a.

The individual samples, in the as-deposited and annealed state, were investigated by x-ray diffraction (XRD) with a Siemens D500 diffractometer in Bragg-Brentano (θ-2θ) geometry using Cu-Kα radiation.

Detailed investigations of the microstructure were conducted by transmission electron microscopy (TEM) and scanning transmission electron microscopy (STEM) using a Tecnai G^2 TF 20 UT microscope operating at 200 keV. In STEM mode, the probe size was <1 nm and the images were recorded with a high-angle annular dark field (HAADF) detector. A camera length of 90 mm was used to increase the mass-thickness contrast and to reduce the influence of diffraction contrast. Energy-dispersive x-ray spectroscopy (EDS) during STEM investigations was used to correlate the different contrasts with chemical compositions.

Simultaneous thermal analysis (STA), consisting of thermogravimetric analysis (TGA), differential scanning calorimetry (DSC), and mass spectrometry (MS), was conducted with a Netzsch STA 409C connected with a quadrupole mass spectrometer through a skimmer coupling. Dynamical heating with a heating rate of 20 K/min to a maximum temperature of 1450 °C was performed in three different atmospheres, Ar (50 sccm, 99.999% purity), N_2 (50 sccm, 99.999% purity), and synthetic air (50 sccm, 20% O_2 and 80% N_2). For studying the chemical influence on the thermal stability, both coating compositions were investigated in Ar at a lower heating rate (10 K/min) for better separation of the occurring reactions. The STA equipment was calibrated in temperature and sensitivity for DSC measurements using pure elements (Sn, Zn, Al, Ag, and Au). To avoid interdiffusion and influences of the substrate material during STA measurements, the coatings were chemically removed from their low-alloyed steel substrates using a 10 mol% nitric acid. After filtering and cleaning, the coating material was mechanically ground to a fine powder whereof ~30 mg were used for each measurement.

Indentation experiments of samples in the as-deposited state and after annealing in Ar up to 900 °C were performed with a NanoIndenter II equipped with a Berkovich diamond tip. Compared to the applied load of 25 mN for the indentation experiments of the coatings, resulting in an indentation depth of ~200 nm, the load for the substrate measurements was chosen to be 300 mN to probe a larger volume with a significant assembly of grains (indentation depth ~880 nm). For each sample, the results of 40 indents were averaged to achieve a statistically relevant measure of hardness. Fused SiO_2 was used as reference. The hardness values were determined from the unloading segments of the load-displacement data following the method of Oliver and Pharr.[21]

Results and discussion

Chemical analysis by RBS and TOF-ERDA of the coatings prepared from the targets with Al/Cr ratios of 60/40 and 70/30 reveals stoichiometric nitrides with an Al/Cr ratio of 56/44 and 68/32, respectively. The total impurity level of H, C, and O in the coatings is below 1%, resulting in a chosen nomenclature for the coatings in this work of $Al_{0.56}Cr_{0.44}N$ and $Al_{0.68}Cr_{0.32}N$. Comparisons of film and target compositions exhibit a loss of Al during deposition. Figure 1 shows XRD line profiles of $Al_{0.68}Cr_{0.32}N$ and $Al_{0.56}Cr_{0.44}N$ coatings on cemented carbide (a and b) as well as the corresponding powdered samples (c and d) indicating that the as-deposited coatings are single-phase face-centered cubic (fcc) for both compositions. Calculation of the lattice parameters for $Al_{0.56}Cr_{0.44}N$ and $Al_{0.68}Cr_{0.32}N$ coatings out of the corresponding 2θ values of the peak maxima obtained from the line profiles of the powder specimen results in 4.112±0.006 and 4.100±0.004 Å, respectively.

Figure 2 shows a cross-sectional bright-field transmission electron micrograph of $Al_{0.68}Cr_{0.32}N$ (a) and selected area diffraction (SAD) patterns from $Al_{0.68}Cr_{0.32}N$ (b) and $Al_{0.56}Cr_{0.44}N$ (c). The coatings on cemented carbide have a dense polycrystalline structure with elongated grains along the growth direction. The grain size as well as the grain size evolution along the thickness of the film is comparable between the investigated $Al_{0.56}Cr_{0.44}N$ and $Al_{0.68}Cr_{0.32}N$ coatings including a fine-grained nucleation layer. SAD confirms the XRD results of a single-phase fcc structure.

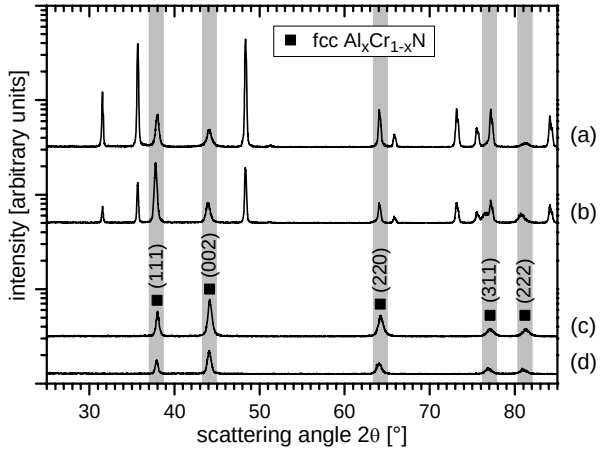

Fig. 1. XRD line scans of as-deposited $Al_xCr_{1-x}N$ coatings on cemented carbide substrates with Al/Cr ratios of 68/32 (a) and 56/44 (b), and $Al_xCr_{1-x}N$ powder after removing from their low-alloyed steel substrate with Al/Cr ratios of 68/32 (c) and 56/44 (d). Calculated lattice plane positions for a fcc crystal having a lattice parameter of 4.1Å are indicated by the center of grey columns.

Investigations of thermal stability have to consider that in $Al_xCr_{1-x}N$[17,22] and CrN[22,23] the Cr-N bonds break during annealing above ~1000 °C to form Cr under the release of N_2 via the intermediate step of Cr_2N. As shown in literature,[24] this dissociation of CrN into its components (Cr and N_2) depends on the nitrogen partial pressure.

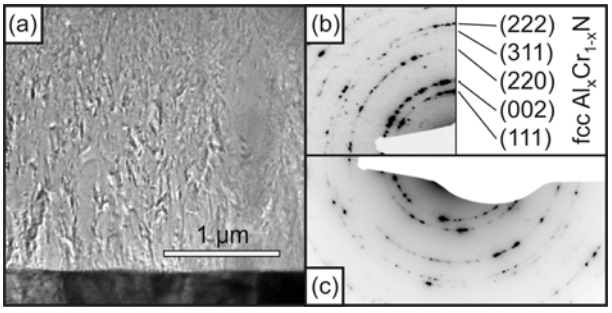

Fig. 2. (a) Cross-sectional bright-field TEM micrograph (b) and SAD pattern from the as-deposited $Al_{0.68}Cr_{0.32}N$ coating and (c) SAD pattern from the as-deposited $Al_{0.56}Cr_{0.44}N$ coating.

Consequently, comparative STA studies are conducted in Ar and N_2 atmosphere for $Al_{0.56}Cr_{0.44}N$ to verify the extent of this effect. Additionally, synthetic air is used for investigations on film oxidation and its influence on CrN dissociation, see Figs. 3a-c. Annealing in N_2 atmosphere results in an ~150 °C higher onset temperature (T_o) for the

N-loss compared to the annealing results obtained in Ar (T_o ~ 1030 °C, see Fig. 3a), where the N_2 partial pressure is essentially zero. Furthermore, the second dissociation step from Cr_2N into Cr and N_2 is completely suppressed during annealing up to 1450 °C in N_2 atmosphere (see Fig. 3a).

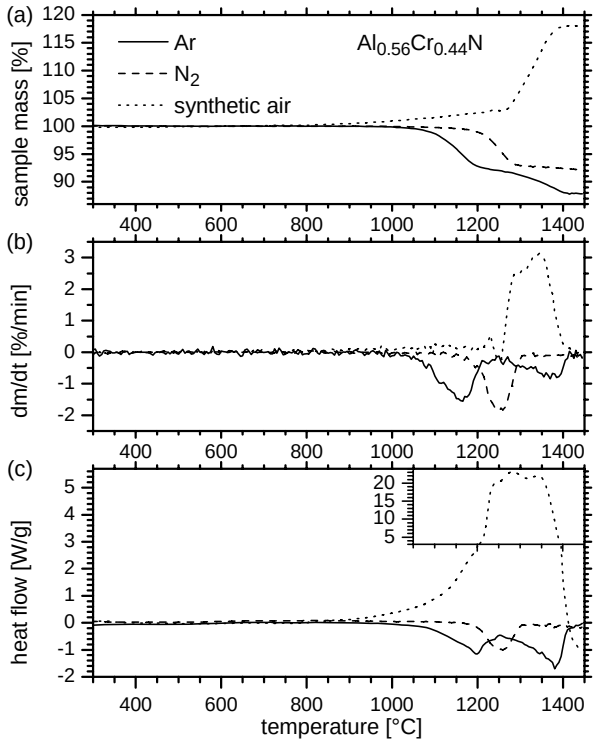

Fig. 3. (a) TGA, (b) DTG and (c) DSC results from an $Al_{0.56}Cr_{0.44}N$ coating with a heating rate of 20 K/min in different atmospheres (Ar, N_2, and synthetic air).

In synthetic air, the described effect of a different nitrogen partial pressure is superimposed by oxidation which can be seen in the TGA results by a mass gain starting at ~1000 °C (Fig. 3a). Nevertheless, the onset of dissociation of CrN into Cr_2N and nitrogen is shifted even to higher temperatures (~1220 °C) than for N_2 conditions. Figure 3b shows this more clearly by the first derivative of the TGA signal (DTG) where the area under the curve represents the reaction specific mass-loss. There, the overlap of oxidation and dissociation (~1220 °C) becomes more prominent. This elevated onset of dissociation can be explained by the formation of an $(Al,Cr)_2O_3$ oxide layer,[25] as XRD shows for the sample annealed to 1450 °C in synthetic air, acting as a diffusion barrier inhibiting the nitrogen out-diffusion of $Al_xCr_{1-x}N$. Due to the large specific surface of the powder

material used for the STA investigations our specimen shows a pronounced mass increase during oxidation (Fig. 3a). The DSC signal (Fig. 3c) confirms the result of TGA and DTG of a two-step dissociation reaction in Ar (4 CrN → 2 Cr_2N + N_2 and 2 Cr_2N → 4 Cr + N_2) and the suppressed second reaction step in N_2 by two and one endothermic features, respectively. Up to 900 °C the DSC and TGA signals of our $Al_xCr_{1-x}N$ films are similar for the three used atmospheres Ar, N_2, and synthetic air (see Fig. 3). For the cemented carbide substrate material, on the other hand, a protection against reactions with the ambient atmosphere must be ensured for ex-situ annealing experiments up to 900 °C; this is why Ar was the choice for comparative annealing studies of $Al_{0.56}Cr_{0.44}N$ and $Al_{0.68}Cr_{0.32}N$.

Figure 4 shows the development of sample mass over temperature in Ar atmosphere demonstrating comparable characteristics in thermal stability for the films with Al/Cr ratios of 56/44 and 68/32. The onset temperature for the mass-loss of $Al_{0.68}Cr_{0.32}N$ is ~1030 °C. The lower Al-containing $Al_{0.56}Cr_{0.44}N$ coating yields a ~30 °C higher onset temperature. Different total mass-loss of both compositions can be explained by the Cr content and their consequently different amount of Cr-N bonds. Theoretical mass loss values for $Al_{0.56}Cr_{0.44}N$ and $Al_{0.68}Cr_{0.32}N$, based on the calculated content of nitrogen bonded to Cr, correspond to 9.1 and 11.8 wt%, respectively. These values are in excellent agreement with the measured mass losses of 9.0 and 11.7 wt% under the used conditions and indicate a complete separation of CrN into Cr and N_2. This is corroborated by MS results (Fig. 4b) showing that the signal caused by N_2 release approaches again the zero level at ~1375 °C. Figure 4c shows the corresponding DSC signals with two strong endothermic features related to two CrN decomposition steps as described in Refs. 17 and 22.

For $Al_{0.56}Cr_{0.44}N$ and $Al_{0.68}Cr_{0.32}N$, no sample mass-loss (Fig. 4a) or N_2 release (Fig. 4b) can be detected during the experiments in Ar atmosphere up to the onset of this dissociation at ~1030 °C. A detailed investigation of the heat flow signal (magnified region in Fig. 4c) reveals a difference between the two investigated coatings regarding the exothermic contribution in the temperature range 650-900 °C. The exothermic signal in the temperature range 500-700 °C can be attributed to recovery (see next paragraph) which starts slightly above the deposition temperature.[11,16] Although these reactions are similar for both compositions, the DSC signal from $Al_{0.68}Cr_{0.32}N$ indicates an additional

exothermic feature which results in an exothermic peak at ~820 °C superimposed by the recovery processes and the endothermic CrN dissociation. For the $Al_xCr_{1-x}N$ film with lower Al content ($Al_{0.56}Cr_{0.44}N$), this peak can not be detected (Fig. 4c). Above 900 °C, the strong endothermic contribution due to the breaking of Cr-N bonds becomes dominant for both coatings.

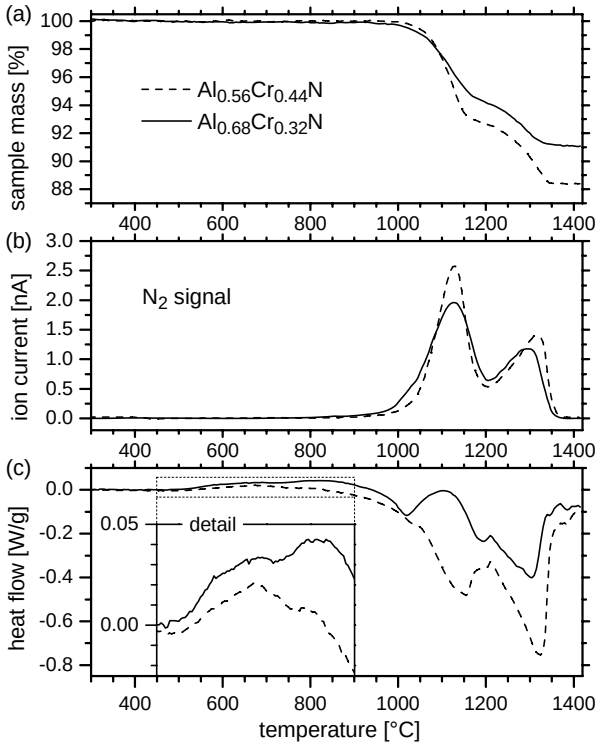

Fig. 4. (a) TGA, (b) MS, and (c) DSC investigations of $Al_{0.56}Cr_{0.44}N$ and $Al_{0.68}Cr_{0.32}N$ coatings with a heating rate of 10 K/min in Ar atmosphere.

Figure 5 shows XRD patterns from $Al_{0.56}Cr_{0.44}N$ (a) and $Al_{0.68}Cr_{0.32}N$ (b) coatings on cemented carbide after annealing treatment in Ar up to 900 °C. The displayed 2θ range in Fig. 5 (34.5° - 40.5°) covers a substrate peak and the fcc $Al_xCr_{1-x}N$ (111) reflex as well as the w-AlN (0002) position. For both compositions, the full width at half maximum (FWHM) of the $Al_xCr_{1-x}N$ (111) peak at 750 °C is decreased by ~2.5% compared to the respective as-deposited state implying recovery in this temperature range as suggested by DSC (Fig. 4c). The XRD results also indicate that $Al_{0.56}Cr_{0.44}N$ stays single-phase up to 1000 °C whereas for $Al_{0.68}Cr_{0.32}N$ precipitation of w-AlN can be detected with $T_a \geq 700$ °C. Consequently, the exothermic signal during DSC of $Al_{0.68}Cr_{0.32}N$ (see detail

in Fig. 4c) with a maximum at ~820 °C is assigned to w-AlN precipitation. In contrast to thermal investigations of $Ti_{1-x}Al_xN$, where the formation of w-AlN occurs via cubic AlN,[16] no indication for such a precipitation route can be observed here during annealing of $Al_{0.68}Cr_{0.32}N$ (Fig. 5b). These results indicate that the energetic requirements for an intermediate precipitation step with respect of driving and retarding forces are not fulfilled for the $Al_xCr_{1-x}N$ coatings in the investigated compositional range. Due to the lattice mismatch between the fcc $Al_xCr_{1-x}N$ matrix and w-AlN, their precipitation involves nucleation and growth.

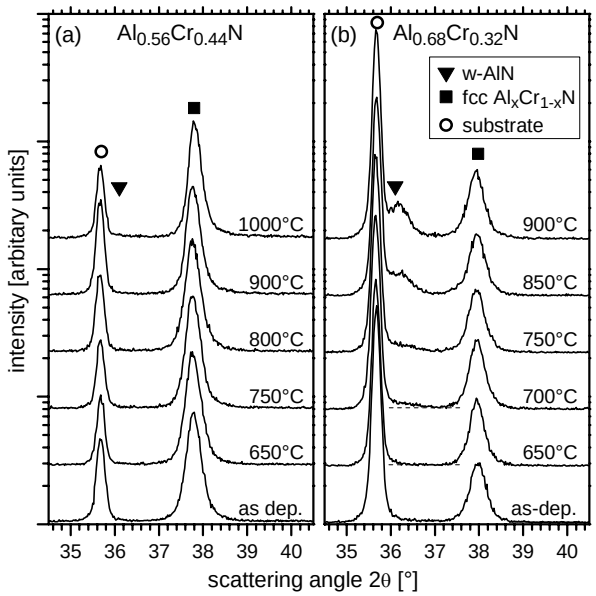

Fig. 5. XRD patterns from (a) $Al_{0.56}Cr_{0.44}N$ and (b) $Al_{0.68}Cr_{0.32}N$ coatings on cemented carbide substrates after thermal annealing.

Cross-sectional bright-field TEM micrographs of $Al_{0.68}Cr_{0.32}N$ annealed at 750 °C (Fig. 6a) show no significant change in the microstructure compared to the as-deposited state which is also valid for $Al_{0.56}Cr_{0.44}N$. SAD however, emphasizes the different structural development of $Al_{0.56}Cr_{0.44}N$ with exclusively fcc diffraction rings (Fig. 6c) compared to $Al_{0.68}Cr_{0.32}N$ (Fig. 6b) where additional rings of w-AlN are present. Contrary to bright-field TEM, where no distinguishable contrast can be seen between matrix and precipitates, STEM with an HAADF detector enables this differentiation. Investigating an area of constant thickness with the chosen STEM settings allows obtaining a qualitative

relation of contrast with chemical composition. Figure 7 shows a detailed view of $Al_{0.68}Cr_{0.32}N$ annealed at 750 °C where dark areas are related to phases of low atomic mass and correspond to AlN as confirmed by EDS during STEM. This confirms XRD (Fig. 5) and DSC (Fig. 4c) results of present w-AlN precipitates at this temperature. Plan-view as well as cross-sectional investigations (Figs. 7a and b) indicate that the precipitates are located at the grain boundaries of the $Al_xCr_{1-x}N$ matrix in our $Al_{0.68}Cr_{0.32}N$ coating.

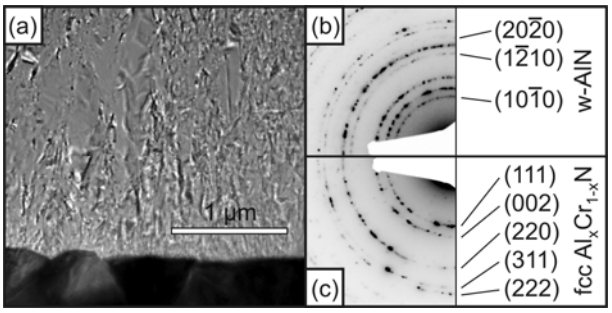

Fig. 6. (a) Cross-sectional bright-field TEM micrograph and (b) SAD pattern from an $Al_{0.68}Cr_{0.32}N$ coating annealed at 750 °C and (c) SAD pattern from an $Al_{0.56}Cr_{0.44}N$ coating annealed at 750 °C.

In the as-deposited state, the two investigated coatings show hardness values of 30±1.3 GPa which corresponds well with reported values for $Al_xCr_{1-x}N$.[1,3,5,8-10] The hardness evolution with annealing temperature of the coatings is displayed in Fig. 8. $Al_{0.56}Cr_{0.44}N$ shows a constant hardness of ~30 GPa up to 900 °C which is ~400 °C beyond the onset of recovery (compare Fig. 4c). Even after annealing the sample at 1000 °C for 60 min, there is no softening although inter-diffusion of substrate material into the coating can not be excluded.[26] The substrate hardness of 21±0.6 GPa shows also no dependency on the annealing history. The coating with higher Al content ($Al_{0.68}Cr_{0.32}N$) on the other hand exhibits a hardness development with T_a. Starting with a stable value of 30±1.3 GPa exceeding the deposition temperature (500 °C), the hardness increases from $T_a = 650$ °C gradually up to 31.6±1.3 GPa at $T_a = 725$ °C. The increase of the mean-hardness values indicate that w-AlN precipitation starts at $T_a \sim 650$ °C as suggested by DSC (Fig. 4c). Due to the small size and volume fraction at the onset of precipitation, XRD intensity for w-AlN is below the detection limit at $T_a = 650$ °C (see Fig. 5b). After the peak in mean-hardness value of 31.6 GPa, the hardness declines to 27.5±1 GPa at $T_a = 900$ °C.

Such a dependence of hardness on the annealing temperature is typical for precipitation hardening.[11]

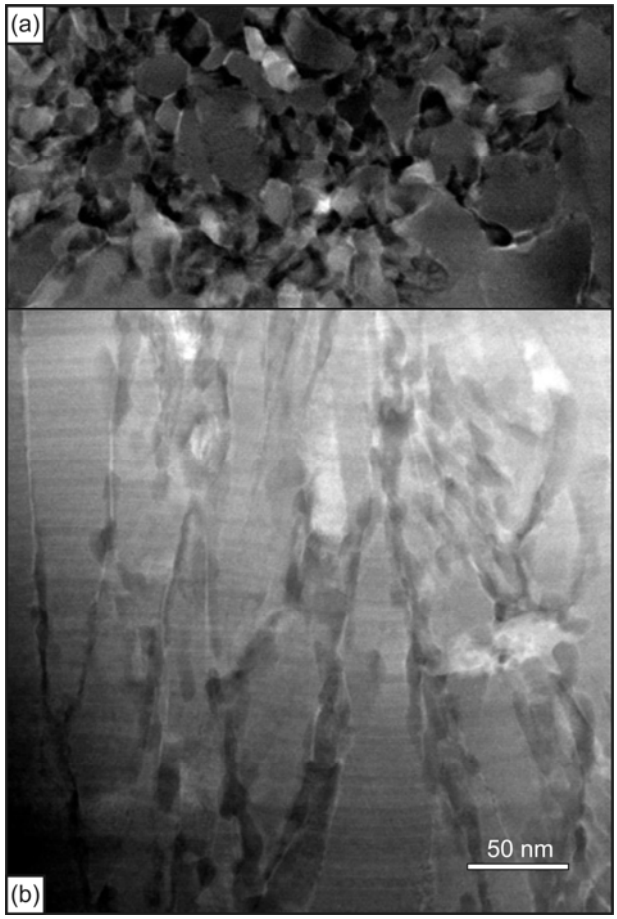

Fig. 7. (a) HAADF plan-view and (b) cross-sectional STEM images from the $Al_{0.68}Cr_{0.32}N$ coating annealed at 750 °C.

The effectiveness of precipitation hardening depends on distribution, size, and number of precipitates which hinder dislocation glide. Especially at the early stages of w-AlN precipitation, their small size combined with a high distribution density results in a hardness increase. Consequently, the hardness for $Al_{0.68}Cr_{0.32}N$ reaches a maximum in the temperature range 650-725 °C, compare Figs. 8, 4c, and 5b. As w-AlN provides a different structure with a huge lattice mismatch to the matrix, effective obstacles are formed. Furthermore, the ~26% larger molar volume of w-AlN compared to the cubic modification[27] introduces compressive strain fields in their surrounding, offering an additional contribution to the elevated hardness. With increasing volume fraction of

w-AlN, having ~30% lower hardness than $Al_xCr_{1-x}N$,[1,4,10] the influence of this softer phase on the compound becomes dominant (at $T_a > 725$ °C), resulting in a lower indentation hardness than the as-deposited value (at $T_a \geq 800$ °C).

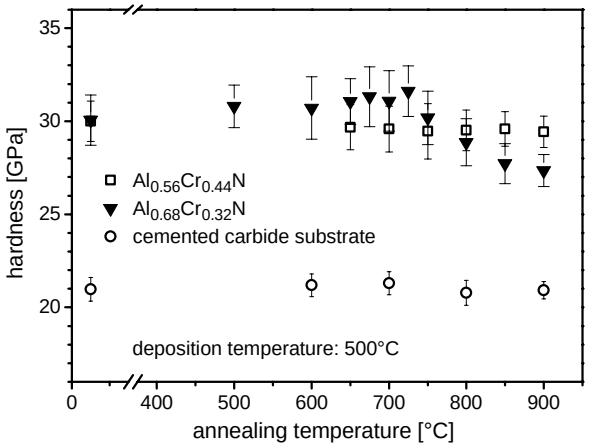

Fig. 8. Hardness of $Al_{0.56}Cr_{0.44}N$ and $Al_{0.68}Cr_{0.32}N$ coatings and their cemented carbide substrate after annealing for 60 min in Ar at different temperatures.

For precipitation of w-AlN in metastable single-phase cubic $Al_xCr_{1-x}N$, the system has to overcome not only the necessary activation energy to start the phase transformation, but also the strain energy caused by the larger molar volume of w-AlN.[28] Whereas the onset temperature for w-AlN precipitation is found to be at ~650 °C for $Al_{0.68}Cr_{0.32}N$, no w-AlN precipitation can be detected for $Al_{0.56}Cr_{0.44}N$ by DSC, XRD, and SAD up to a temperature where already CrN dissociation starts. These results indicate that the energetic balance promotes w-AlN precipitation for $Al_{0.68}Cr_{0.32}N$ but not for the lower Al-containing $Al_{0.56}Cr_{0.44}N$.

Conclusions

Single-phase $Al_{0.56}Cr_{0.44}N$ and $Al_{0.68}Cr_{0.32}N$ hard coatings can be synthesized in the NaCl structure by arc evaporation. Both as-deposited coatings exhibit a similar dense polycrystalline microstructure with grains elongated in growth direction. Dependent on the atmosphere during simultaneous thermal analysis, Cr-N bonds in the material start to break at ~1030 °C in Ar, at ~1180 °C in N_2, and at ~1220 °C in synthetic air, respectively.

Oxidation during annealing experiments in synthetic air starts at ~1000 °C. The investigated $Al_{0.56}Cr_{0.44}N$ coatings are composed of w-AlN and Cr_2N or w-AlN and Cr after annealing at 1450 °C in N_2 or Ar, respectively. This is due to the influence of the different nitrogen partial pressure on the CrN dissociation. In Ar atmosphere up to 1450 °C, dissociation consists of two completed reaction steps resulting in the formation of Cr whereas under N_2 conditions the second dissociation step from Cr_2N to Cr is suppressed. Up to 900 °C, no influence of the used annealing atmosphere on the STA measurements could be detected. $Al_{0.56}Cr_{0.44}N$ coatings remain single-phase crystalline during annealing up to 900 °C. Although this temperature exceeds the onset of recovery by ~400 °C the hardness remains unaffected at ~30 GPa. $Al_{0.68}Cr_{0.32}N$ coatings on the other hand undergo precipitation of w-AlN, which occurs preferentially at grain boundaries by nucleation and growth. In the early precipitation stages, these act as obstacles for dislocation glide and hence hardness increases from the as-deposited value of ~30 GPa to ~31.6 GPa at T_a = 725 °C. Exceeding this temperature, w-AlN becomes dominant in the matrix due to increased volume fraction and size, and hence the hardness decreases to ~27.5 GPa with T_a = 900 °C. Both coatings show a general high thermal stability with high hardness up to 900 °C with effective age-hardening of $Al_{0.68}Cr_{0.32}N$ in the temperature range of ~650-725 °C.

Acknowledgements

The authors want to thank Dr. Jörg Neidhardt (Christian Doppler Laboratory for Advanced Hard Coatings at the University of Leoben) for the support in sample deposition. We are also grateful to Dr. Manfred Beckers (IFM – Thin Film Physics Division, Linköping University) for the chemical analysis carried out at the National Tandem Accelerator Facility at Uppsala University, Sweden. The work done in Leoben was financed within the framework of the Austrian Kplus Competence Center Program and in part by the Christian Doppler Research Association. The work done in Linköping was financed within the Swedish Foundation for Strategic Research (SSF) Strategic Research Center MS^2E on Materials Science for Nanoscale Surface Engineering.

Literature:

[1] A.E. Reiter, V.H. Derflinger, B. Hanselmann, T. Bachmann, B. Sartory, Surf. Coat. Technol. 200, 2114 (2005).

[2] W. Kalss, A.E. Reiter, V. Derflinger, C. Gey, J.L. Endrino, Int. J. Refract. Met. Hard Mat. 24, 399 (2006).

[3] J. Vetter, E. Lugscheider, S.S. Guerreiro, Suf. Coat. Technol. 98, 1233 (1998).

[4] H. Hasegawa, T. Suzuki, Surf. Coat. Technol. 188-189, 234 (2004).

[5] X.-Z. Ding, X.T. Zeng, Surf. Coat. Technol. 200, 1372 (2005).

[6] O. Banakh, P.E. Schmid, R. Sanjinés, F. Lévy, Surf. Coat. Technol. 163-164, 57 (2003).

[7] M. Kawate, A.K. Hashimoto, T. Suzuki, Surf. Coat. Technol. 165, 167 (2003).

[8] Y. Ide, T. Nakamura, K. Kishitake, Second International Conference on Processing Materials for Properties, Edited by B. Mishra and C. Yamauchi, TMS (San Francisco 2000), p. 291.

[9] M. Hirai, Y. Ueno, T. Suzuki, W. Jiang,, C. Grigoriu, K. Yatsui, Jpn. J. Appl. Phys. 40, 1056 (2001).

[10] M. Kawate, A. Kimura, T. Suzuki, J. Vac. Sci. Technol. A 20(2), 569 (2002).

[11] P.H. Mayrhofer, C. Mitterer, L. Hultman, H. Clemens, Prog. Mater.Sci. 54, 1032 (2006).

[12] L. Hultman, Vacuum 57, 1 (2000).

[13] A. Sugishima, H. Kajioka, Y. Makino, Surf. Coat. Technol. 97, 590 (1997).

[14] Y. Makino, K. Nogi, Surf. Coat. Technol. 98, 1008 (1998).

[15] Y. Makino, Surf. Coat. Technol. 193, 185 (2005).

[16] P.H. Mayrhofer, A. Hörling, L. Karlsson, J. Sjölén, T. Larsson, C. Mitterer, L. Hultman, Appl. Phys. Lett. 83(10), 2049 (2003).

[17] H. Willmann, P.H. Mayrhofer, P.O.Å. Persson, A.E. Reiter, L. Hultman, C. Mitterer, Scripta Mater. 54, 1847 (2006).

[18] M. Mayer, Technical Report IPP9/113, (Max-Planck-Institut für Plasmaphysik, Garching, Germany, 1997)

[19] Y. Zhang, H.J. Whitlow, T. Winzell, I.F. Bubb, T. Sajavaara, K. Arstila, J. Keinonen, Nucl. Instr. and Meth. in Phys. Res. B 149, 477 (1999).

[20] M.S. Janson, CONTES instruction manual (2004).

[21] W.C. Oliver, G.M. Pharr, J. Mater. Res. 7(6), 1564 (1992).

[22] P.H. Mayrhofer, H. Willmann, A.E. Reiter, 49th Annual Technical Conference Proceedings (Society of Vacuum Coaters, 2006), p. 575.

[23] F-H. Lu, H-Y. Chen, Thin Solid Films 398-399, 368 (2001).

[24] J.P. Neumann, M. Venkatraman, in T.B. Massalski (editor), Binary Alloy Phase Diagrams, volume 2, 2nd ed., (ASM International, Metals Park, Ohio, 1990), p. 1293.

[25] A.E. Reiter, C. Mitterer, M. Ante, B. Sartory, J. Vac. Sci. Technol. A submitted.

[26] A. Hörling, J. Sjölén, L. Karlsson, M.Odén, L. Hultman, J. Vac. Sci. Technol. A20(5), 1815 (2002).

[27] Powder Diffraction File (Card 25-1133 for hex-AlN, Card 42-1200 for cub-AlN), International Centre for Diffraction Data, ICDD – JCPDS, (1998).

[28] P.H. Mayrhofer, F.D. Fischer, H.J. Böhm, C. Mitterer, J.M. Schneider, Acta Mater. 55, 1441 (2007).

Publication III

Single-crystal growth of NaCl-structure Al-Cr-N thin films on MgO(001) by magnetron sputter epitaxy

H. Willmann
M. Beckers
F. Giuliani
J. Birch
P.H. Mayrhofer
C. Mitterer
L. Hultman

Submitted to
Scripta Materialia

Single-crystal growth of NaCl-structure Al-Cr-N thin films on MgO(001) by magnetron sputter epitaxy

H. Willmann[1,2,a)], M. Beckers[2)], F. Giuliani[2)], J. Birch[2)], P.H. Mayrhofer[3)], C. Mitterer[3)], L. Hultman[2)]

[1)] Materials Center Leoben, 8700 Leoben, Austria
[2)] IFM Material Physics, Division of Thin Film Physics, Linköping University, 58183 Linköping, Sweden
[3)] Department of Physical Metallurgy and Materials Testing, University of Leoben, 8700 Leoben, Austria

Single-crystal NaCl-structure $Al_{0.68}Cr_{0.32}N$ thin films were deposited onto MgO(001) substrates. The films exhibit cube-on-cube epitaxial growth with an initial pseudomorphic strained layer before complete relaxation into an isotropic lattice parameter of 4.119 Å as shown by symmetric high-resolution x-ray diffraction and asymmetric reciprocal space maps. The relaxation proceeds via a threading dislocation network as revealed by transmission electron microscopy. Films of 900 nm thickness have a hardness of 32.4±0.5 GPa, an elastic modulus of 460.8±5 GPa, and a room-temperature resistivity of 2.7×10^3 Ωcm.

Keywords: CrAlN, x-ray diffraction, nanoindentation, transmission electron microscopy, single crystal growth,

Magnetron sputtering of thin films can be used to grow metastable ternary phases of otherwise immiscible binary equilibrium phases due to the high quenching rate at the arrival on the substrate. The new phases offer new material properties for potential applications. A less studied material is $Al_xCr_{1-x}N$ in which cubic (c) B1 NaCl-structure CrN and hexagonal B4 wurtzite-structure AlN (w-AlN) are the equilibrium phases. The metastable hexagonal modification (w-$Al_xCr_{1-x}N$) is used for band gap engineering and production of dilute magnetic semiconductors.[1,2] The metastable c-$Al_xCr_{1-x}N$ on the other hand is used as protective hard coating in cutting and forming applications.[3]

Polycrystalline c-$Al_xCr_{1-x}N$ shows increased thermal stability, oxidation resistance, and hardness compared to CrN.[3-9] Magnetron sputter epitaxy of CrN[10] and w-AlN,[11] as well as molecular beam epitaxy of w-$Al_xCr_{1-x}N$[1] films have been reported. However, there are no results on epitaxial c-$Al_xCr_{1-x}N$ films, which could enable specific studies on the phase transformations known to take place in the polycrystalline films.[4,12]

Here, we present first results of smooth, single-crystal epitaxial c-$Al_xCr_{1-x}N$ films on MgO(001) substrates with thicknesses up to 900 nm. The films grow with a cube-on-cube relation to the MgO template with an initial pseudomorphic strained layer and subsequent fully relaxed lattice linked to an observed threading dislocation network formed during film growth.

All films were grown in a load-locked high-vacuum deposition system described elsewhere.[13] The base pressure in the chamber was 2.67×10^{-4} Pa (2×10^{-6} Torr), while reactive sputtering was carried out in pure N_2 (99.999 %) at a pressure of 0.4 Pa (3×10^{-3} Torr). Polished $10\times10\times0.5$ mm^3 MgO(001) wafers and equal pyrolytic graphite pieces were used as substrates, thermally degassed at ~750 °C for 60 min and afterwards set to a constant deposition temperature of 500 °C, with an applied bias of -40 V. The substrates were positioned on a rotating substrate holder at a distance of 92 mm from the planar unbalanced magnetron, which is tilted by 25° to the substrate normal. A 75 mm diameter $Al_{0.70}Cr_{0.30}$ compound target was used, operated at a constant power of 250 W with an according deposition rate of ~4.9 nm/min. The resulting film thicknesses for 10, 60, and 180 min deposition time were 50, 300, and 900 nm, respectively. Chemical composition of the films was analyzed by Rutherford backscattering spectroscopy (RBS) with a 2 MeV $^4He^+$ beam, evaluated with the SIMNRA code.[14] Structural characterization was carried out by high-resolution x-ray diffraction (HR-XRD), through radial (2θ-ω) scans, rocking (ω) curves, as well as reciprocal space maps (RSM) of the symmetric 002 and the asymmetric 113 peaks, using a Philips X'pert MRD diffractometer equipped with monochromator and analyzer crystals, resulting in Cu-K_α monochromacy of $\Delta\lambda/\lambda = 4.3183\times10^{-3}$. Cross-sectional and plan-view transmission electron microscopy (TEM) was performed on a Tecnai G^2 TF 20 UT microscope operating at 200 keV. A UMIS nanoindenter equipped with a Berkovich diamond tip was used for obtaining

mechanical properties at an indentation force of 10 mN. The room-temperature resistivity was measured with a Jandel four-point probe with a spring loaded linear measurement head.

RBS revealed nitrogen stoichiometry for all films, with an (Al,Cr)/N ratio of 1.00±0.02, cross-checked by samples deposited onto pyrolytic graphite. The chemical composition was $Al_{0.68\pm0.01}Cr_{0.32\pm0.01}N$, in good agreement with the target Al/Cr ratio. Full-range HR-XRD data with $25° < 2\theta < 85°$ and azimuthal scans, both not shown here, prove single-phase cube-on-cube growth of NaCl-structure films. Figure 1a displays the essential section of the HR-XRD data around the substrate and the 50 and 300 nm thick film 002 peaks. Both curves show MgO 002 at $2\theta = 42.924°$, corresponding to an out-of-plane lattice parameter of $a_\perp = 4.211$ Å, matching the literature value of 4.2112 Å for MgO.[15] Additionally, a symmetric c-$Al_{0.68}Cr_{0.32}N$ 002 peak at $2\theta = 44.238°$ is visible for the 50 nm thick film, corresponding to $a_\perp = 4.091$ Å. With increasing film thickness the peak splits into a doublet with main intensity at a lower angle of $2\theta = 43.910°$ ($a_\perp = 4.120$ Å). Since the composition is constant over the whole film thickness, this peak shift indicates an initial pseudomorphic strained interlayer, with gradual change towards relaxed growth for increasing film thickness. The 900-nm-thick $Al_{0.68}Cr_{0.32}N$ film displayed similar peak shape and intensity as the 300 nm one. The calculated out-of-plane lattice parameters for these two films lie between the values for CrN (4.162 Å)[10] and c-AlN (4.045 Å)[15] as indicated by the spacers for $Al_{0.68}Cr_{0.32}N$ in Fig. 1a, and correspond well with values for polycrystalline material of comparable chemical composition.[7-9] The full width at half maximum ($\Gamma_{2\theta-\omega}$) of the film 002 peak is 0.42° for the 50 nm and 0.15° for the thicker films, compared to 0.07° for the single-crystal substrate MgO 002, hence the corresponding vertical x-ray coherence length $\xi_\perp$ grows with increasing film thicknesses. Its value of $\xi_\perp = 650$ Å for the thick $Al_{0.68}Cr_{0.32}N$ films is in the range of epitaxially grown NaCl-structure binary nitrides with comparable lattice mismatch, i.e. ~950 Å for CrN[10], ~1000 Å for TaN,[16] or 1900 Å for TiN.[17] Figure 1b shows the corresponding rocking curves measured at the 2θ values of maximum intensity. The full width at half maximum (Γ_ω) decreases from 0.92° to 0.45° for increasing film thickness from 50 to 300 nm. This

difference is likely related to the strain fields within the pseudomorphic interlayer. The calculated lateral x-ray coherence length $\xi_{\parallel}$ for the thick films, indicating good crystal quality, is 260 Å and comparable to epitaxial CrN (~800 Å),[10] TaN (~210 Å),[16] and TiN (~900 Å)[17] films.

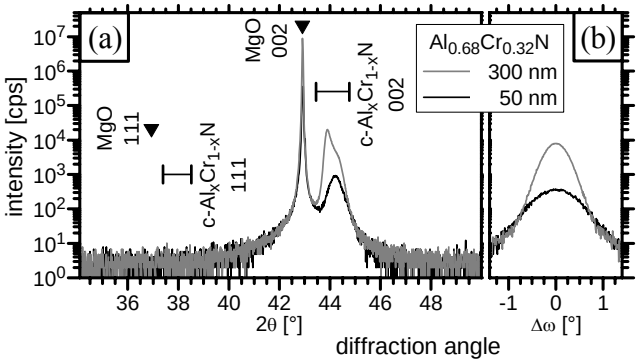

Fig. 1. (a) High-resolution x-ray diffraction and (b) rocking-curves from 50 and 300 nm thick $Al_{0.68}Cr_{0.32}N$ films on MgO(001).

The strain state as well as the correct in-plane ($a_{\parallel}$) and out-of-plane lattice parameters were obtained from asymmetric RSMs around the film 113 peak. The RSM for the 300 nm thick film is displayed in Fig. 2 with the arrow indicating the direction from the origin of reciprocal space. The main intensity of the film lies directly on this line, indicating fully relaxed growth with derived lattice constants of $a_{\perp} = 4.119$ Å and $a_{\parallel} = 4.118$ Å, which correspond well to the $a_{\perp}$ values calculated from the symmetric XRD for the thick films. The shape of the reciprocal lattice point is not symmetrical elliptic, but extended towards the position of the fully pseudomorphic strained state, indicated by the intersection of the dashed and dotted line. This secondary intensity distribution stems from relaxation of a fully strained interlayer to fully relaxed growth as already suggested by the symmetric XRD data.

To further elucidate the relaxation process, the samples were analyzed by plan-view and cross-sectional TEM. Figure 3a and 3b show bright-field and dark-field micrographs (using the g = (040) diffraction condition) of the 900 nm film at the same specimen position, respectively. The film is dense with a flat surface and exhibits no observable grain or domain boundaries, which is revealed by bright-field plan-view TEM whereof a representative area is shown in Fig. 3c. The corresponding spot pattern of the selected area electron diffraction in Fig. 3d implies single-crystal growth. The only observed features

within the film are fine diffraction contrast lines due to threading dislocations shown in the bright-field and dark-field images of Fig. 3a and 3b, respectively. These dislocations are segmented and their traces make angles of 50-60° with the substrate surface. The formation of such a dislocation network with a density of ~3×10^{10} cm^{-2} is not surprising, considering the ~2.18% lattice mismatch between $Al_{0.68}Cr_{0.32}N$ and the larger MgO. Taking into account the coefficients of thermal expansion with $CTE_{MgO} > CTE_{c\text{-}AlCrN}$[10,18] even aggravates the situation at the deposition temperature of 500 °C. The classification of the dislocations' nature and crystallographic orientations is ongoing.

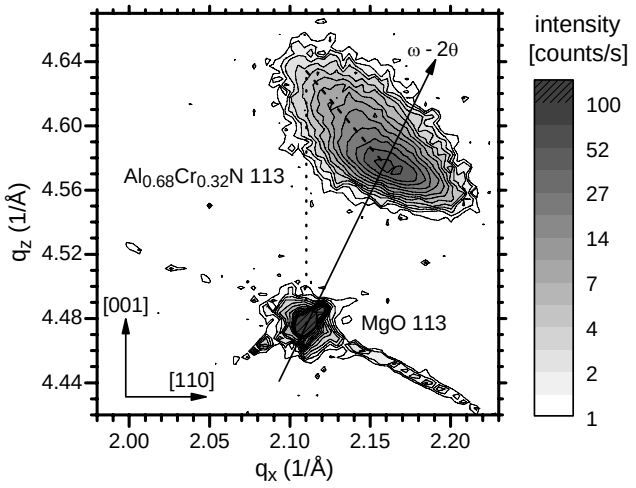

Fig. 2. Asymmetric reciprocal space map around the 113 reflection of a 300 nm thick $Al_{0.68}Cr_{0.32}N$ film on MgO(001).

For studies on mechanical properties, nanoindentation measurements were carried out on the 900 nm thick film. An initial load variation from 2-30 mN with corresponding indentation depths of ~40-300 nm, respectively, ensured conditions of a fully developed plastic deformation zone and no substrate influence. Statistical evaluation over 20 indents yield a hardness of 32.4±0.5 GPa and an elastic modulus of 460.8±5 GPa. Polycrystalline c-$Al_xCr_{1-x}N$ films with comparable chemical composition show similar hardness of ~30 GPa[5-9] but lower elastic modulus of ~350 GPa[5,6] which may be attributed to their lower film density. Compared to single-crystal CrN(001) with a hardness of 28.5 GPa and an elastic modulus of 405 GPa, the increased values due to the change in bonding character by Al-addition is evident.[10] The Cr substitution by Al is also reflected by the room-temperature resistivity, which, measured on 900 nm thick $Al_{0.68}Cr_{0.32}N$, results in

2.7×10^{3} Ωcm in comparison to 7.7×10^{-2} Ωcm for single-crystal CrN.[10] This approaches the semiconducting behavior of w-$Al_{0.93}Cr_{0.07}N$ with values of ~7.5×10^{4} Ωcm.[2]

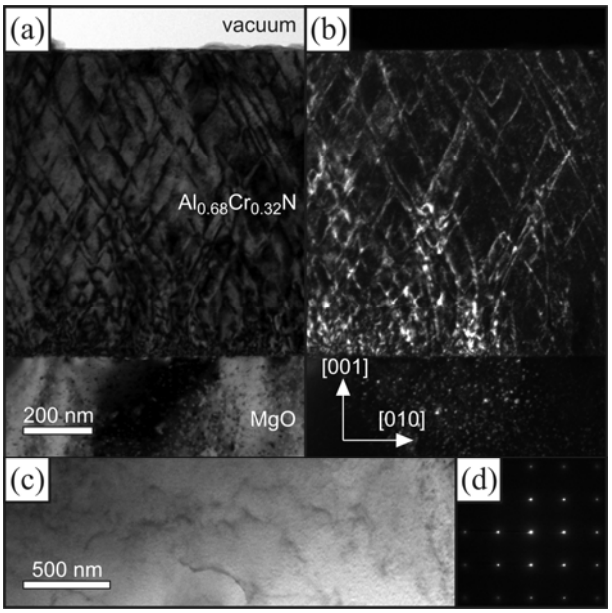

Fig. 3. Cross-sectional transmission electron micrographs from an $Al_{0.68}Cr_{0.32}N$ film on MgO(001) near the [100] zone axis in (a) bright-field and (b) dark-field using the g = (040) diffraction condition. (c) Plan-view bright-field micrograph with corresponding selected area diffraction pattern (d) of the same sample.

In conclusion, we demonstrated the feasibility of single-crystal c-$Al_{0.68}Cr_{0.32}N$ film growth onto MgO(001) substrates by unbalanced magnetron sputtering epitaxy. The films exhibit a relaxed lattice parameter of 4.119 Å and contain threading dislocations network on inclined planes. The solid solution $Al_{0.68}Cr_{0.32}N$ films show improved mechanical properties due to modified bonding characteristics, exhibiting a hardness of 32.4±0.5 GPa and elastic modulus of 460.8±5 GPa. The room-temperature resistivity of $Al_{0.68}Cr_{0.32}N(001)$ is 2.7×10^{3} Ωcm which is orders of magnitude higher than for CrN(001).

The authors thank Dr. F. Eriksson and N. Ghafoor (Linköping University) for support regarding the deposition system. Dr. R. Daniel and Prof. G. Dehm (University of Leoben) are acknowledged for assistance with nanoindentation measurements and discussions on the dislocation network, respectively. The ion beam analyses have been carried out at the FZD Dresden, Germany supported by RITA Contract No. 025646. Work

done in Leoben was financed within the framework of the Austrian Kplus Competence Center Program. Targets have been supplied by Plansee GmbH, Lechbruck, Germany. Work done in Linköping was financed by the Swedish Research Council (VR) and the Swedish Foundation for Strategic Research (SSF) Strategic Research Center MS^2E on Materials Science for Nanoscale Surface Engineering.

[1] A. Y. Polyakov, N. B. Smirnov, A. V. Govorkov, R. M. Frazier, J. Y. Liefer, G. T. Thaler, C. R. Abernathy, S. J. Pearton, and J. M. Zavada, Appl. Phys. Lett. 85 (18), 4067 (2004).

[2] Y. Endo, T. Sato, A. Takita, Y. Kawamura, and M. Yamamoto, IEEE Trans. Magn. 41 (10), 2718 (2005).

[3] A. E. Reiter, V. H. Derflinger, B. Hanselmann, T. Bachmann, and B. Sartory, Surf. Coat. Technol. 200 (7), 2114 (2005).

[4] H. Willmann, P. H. Mayrhofer, P. O. Å. Persson, A. E. Reiter, L. Hultman, and C. Mitterer, Scr. Mater. 54 (11), 1847 (2006).

[5] J. Lin, B. Mishra, J. J. Moore, W. D. Sproul, and J. A. Rees, Surf. Coat. Technol. 201 (16-17), 6960 (2007).

[6] J. Romero, M. A. Gómez, J. Esteve, F. Montalà, L. Carreras, M. Grifol, and A. Lousa, Thin Solid Films 515 (1), 113 (2006).

[7] M. Hirai, Y. Ueno, T. Suzuki, W. H. Jiang, C. Grigoriu, and K. Yatsui, Jpn. J. Appl. Phys. Part 1 - Regul. Pap. Short Notes Rev. Pap. 40 (2B), 1056 (2001).

[8] H. Hasegawa and T. Suzuki, Surf. Coat. Technol. 188-189, 234 (2004).

[9] P. H. Mayrhofer, H. Willmann, and A. Reiter, Proceeding of the 49th SVC Annual Technical Conference, Washington, 2006, pp. 575.

[10] D. Gall, C. S. Shin, T. Spila, M. Odén, M. J. H. Senna, J. E. Greene, and I. Petrov, J. Appl. Phys. 91 (6), 3589 (2002).

[11] J. Birch, S. Tungasmita, and V. Darakchieva, in: Vacuum Science and Technology: Nitrides as seen by the technology, edited by Tanya Paskova and Bo Monemar (Research Signpost, Kerala, 2002), pp. 421.

[12] H. Willmann, P. H. Mayrhofer, L. Hultman, and C. Mitterer, Journal of Vacuum Science & Technology A (submitted).

[13] F. Eriksson, G. A. Johansson, H. M. Hertz, and J. Birch, Optical Engineering 41 (11), 2903 (2002).

[14] M. Mayer, Technical Report, Report No. IPP9/113, Max-Planck-Institut für Plasmaphysik, Garching, Germany 1997.

[15] Powder Diffraction File (Card 46-1200 for c-AlN, Card 45-0946 for MgO), International Centre for Diffraction Data, 1998.

[16] C. S. Shin, D. Gall, P. Desjardins, A. Vailionis, H. Kim, I. Petrov, J. E. Greene, and M. Odén, Appl. Phys. Lett. 75 (24), 3808 (1999).

[17] C. S. Shin, S. Rudenja, D. Gall, N. Hellgren, T. Y. Lee, I. Petrov, and J. E. Greene, J. Appl. Phys. 95 (1), 356 (2004).

[18] D. N. Talwar, Phys. Status Solidi B 235 (2), 254 (2003).

Publication IV

Epitaxial growth of Al-Cr-N thin films on MgO(111)

H. Willmann

M. Beckers

J. Birch

P.H. Mayrhofer

C. Mitterer

L. Hultman

Submitted to

Thin Solid Films

Epitaxial growth of Al-Cr-N thin films on MgO(111)

H. Willmann[1,2], M. Beckers[2], J. Birch[2], P.H. Mayrhofer[3], C. Mitterer[3], L. Hultman[2]

[1] Materials Center Leoben, 8700 Leoben, Austria
[2] IFM Material Physics, Division of Thin Film Physics, Linköping University, 58183 Linköping, Sweden
[3] Department of Physical Metallurgy and Materials Testing, University of Leoben, 8700 Leoben, Austria

Abstract

Cubic rock salt structure $Al_{0.60}Cr_{0.40}N$ and $Al_{0.68}Cr_{0.32}N$ films were grown epitaxially onto MgO(111) substrates by reactive unbalanced magnetron sputtering at 500 °C. Rutherford backscattering spectroscopy reveals stoichiometric nitrides with Al/Cr ratios close to the composition of the used compound targets of 60/40 and 70/30. High resolution x-ray diffraction and transmission electron microscopy show epitaxial growth over the whole ~1.8 µm film thickness. Reciprocal space maps and selected area electron diffraction show that the $Al_xCr_{1-x}N$ films are fully relaxed by misfit dislocations. Limited ad-atom mobility in turn yields epitaxial columns which exhibit {001} top facets.

Keywords: AlCrN, CrAlN, coherence length, mosaicity, wurtzite structure, epitaxy

1. Introduction

Ternary nitrides are used in a wide range of applications from semiconductors to protective hard coatings. The binary nitrides AlN and CrN with wurtzite and rock salt crystallographic structures, respectively, have very low solubility for each other in the thermodynamic equilibrium, even at 1000 °C [1]. However, this restriction can be overcome by physical vapor deposition (PVD) techniques to form metastable solid solutions of $Al_xCr_{1-x}N$ in crystallographic modifications of the corresponding binary systems, where Al and Cr atoms are substituting for each other [2-9]. Depending on the desired application, thin film synthesis in the AlN-CrN system is approached from two

sides of the pseudobinary phase diagram. Starting from hexagonal (wurtzite type, B4) AlN, introduction of Cr is used for band gap engineering and the production of dilute magnetic semiconductors in the field of spintronics [10-15]. Vice versa alloying cubic (rock salt, B1) CrN with Al results in improved mechanical properties for rock salt structure $Al_xCr_{1-x}N$ (c-$Al_xCr_{1-x}N$) [2-6,16] and gives opportunities for cutting applications, in particular for Al-contents close to the maximum supersaturation for the B1/B4 transition in PVD films at x = 0.7 - 0.75 [2-5,17].

Both binary systems, CrN and AlN, have been grown epitaxially in their thermodynamic stable modifications as single layers [18,19]. However, up to date, only polycrystalline c-$Al_xCr_{1-x}N$ thin films have been studied. In this work, epitaxial c-$Al_xCr_{1-x}N$ films with compositions deep within the miscibility gap are presented. MgO(111) substrates are utilized as templates for growth of the single-crystal by reactive unbalanced magnetron sputtering. MgO has rock salt structure and a lattice mismatch of ~2.5% to the investigated c-$Al_xCr_{1-x}N$ films ($0.60 < x < 0.68$) with $a_{MgO} > a_{AlCrN}$.

2. Experimental details

All films were grown in a high-vacuum deposition system equipped with two planar unbalanced magnetrons tilted by 25° to the substrate normal. A detailed description is given elsewhere [20,21]. For the reactive deposition of the $Al_xCr_{1-x}N$ films, only one magnetron was used, mounted with Al/Cr compound targets with atom ratios of 60/40 or 70/30, respectively. The substrates were positioned on a rotating table at a distance of 92 mm from the Ø 75 mm target with a multi-specimen substrate holder. The base pressure of the chamber was 2.67×10^{-4} Pa (2×10^{-6} Torr), achieved using a 510 $l\cdot s^{-1}$ turbomolecular pump while sputtering was carried out in pure N_2 (99.999 %) at a pressure of 0.4 Pa (3×10^{-3} Torr), measured by a capacitance manometer.

Polished MgO(111) wafers of dimension $10\times10\times0.5$ mm^3 with an average roughness (R_a) of 0.114 nm were used as templates for the films. Additionally, substrates of pyrolytic graphite of the same size were used for detailed compositional evaluation. Prior to deposition, the MgO(111) substrates were thermally cleaned at ~750 °C for 60 min. During deposition, the substrates were kept at a constant temperature of 500 °C, measured by a

calibrated pyrometer on an $Al_xCr_{1-x}N$ coated dummy substrate, and cooled down to room temperature before removal from the deposition chamber via a load lock system.

The magnetron was operated at 0.75 A using a constant current regulation, resulting in steady discharge voltages of 370 V and 330 V for the 60/40 and 70/30 target, respectively. The substrates were positioned symmetrically around the sample holder rotation axis to achieve uniform film properties. In order to provide low-energy ion bombardment during growth, a substrate bias of -40 V was applied. Before starting the deposition, the target was plasma etched for 3 min with the substrates protected by a shutter. The influence of the film thickness on the developed microstructure was addressed by samples grown with different deposition times (10, 60, and 180 min) to cover film thicknesses from below 100 to more than 1000 nm.

The chemical compositions of the films were analyzed by Rutherford backscattering spectroscopy (RBS) with a beam of 2 MeV $^4He^+$ ions impinging at an incidence angle of 7° with respect to the surface normal, and being detected at a scattering angle of 167°. The recorded spectra were evaluated using the SIMNRA code [22]. For improved nitrogen quantification, also films from corresponding batches deposited onto pyrolytic graphite were measured, so that the maximum error for nitrogen is about 2 at%, while it is about 1 at% for the heavier Al and Cr.

Structural characterization by high-resolution symmetric x-ray diffraction (HR-XRD), rocking curves, and reciprocal space maps (RSM) were performed using a Philips X'pert MRD triple axis diffractometer with a Cu lab-source. The used optics were a parabolic graded multilayer mirror collimator, followed by a channel-cut 2-bounce Ge (220) monochromator on the primary side and an asymmetric 2-bounce Ge (220) analyzer crystal on the secondary side resulting in Cu-K_α monochromacy of $\Delta\lambda/\lambda = 4.3183\times10^{-3}$. Symmetric RSM were measured around the MgO 111 reflection, whereas intensities of the asymmetric RSMs were obtained around the MgO 113 reflection and in-plane and out-of-plane lattice spacings were evaluated by projecting the peak positions onto the [111] and [110] axes. Azimuthal XRD scans recording the {002} planes were measured with an open detector at a sample surface normal tilt of 54.7° with respect to the diffraction plane (Ψ-tilt).

A Zeiss EVO 50 scanning electron microscope (SEM) equipped with a tungsten filament was used to study the developing morphology by plan-view and fracture cross-sectional investigations in dependence of the film thickness.

Cross-sectional transmission electron microscopy (TEM) was performed on a Tecnai G^2 TF 20 UT microscope operating at 200 keV for detailed studies of the microstructure. The specimens were prepared by mechanical grinding and polishing before dimpling and a final ion milling step with Ar-ions in a Gatan precision ion polishing system (PIPS).

3. Results and discussion

RBS investigations reveal stoichiometric nitrides with an (Al,Cr)/N ratio of 1.00 for all films. The Al/Cr ratios are homogeneous over the whole film thickness and are close to the composition of the corresponding targets, resulting in chemical compositions of $Al_{0.60}Cr_{0.40}N$ and $Al_{0.68}Cr_{0.32}N$ for the 60/40 and 70/30 target setups, respectively. From the fitted RBS spectra, assuming bulk atomic CrN density, the deposition rates are calculated to be 9.7 and 4.9 nm/min for the 60/40 and 70/30 setup, respectively. For the chosen deposition times of 10, 60, and 180 min, total thicknesses of 100, 580, and 1750 nm were obtained for the $Al_{0.60}Cr_{0.40}N$ films and 50, 300, and 900 nm, respectively, for the $Al_{0.68}Cr_{0.32}N$ films. Despite identical deposition parameters, the different chemical composition of the targets affects the working point during reactive sputtering, where the lower resulting power and the higher Al-content for the 70/30 setup results in a poisoned target with a significantly reduced deposition rate.

Overview XRD 2θ–ω scans from 25-85° indicate single-phase c-$Al_xCr_{1-x}N$ films, with corresponding MgO and c-$Al_xCr_{1-x}N$ $\ell\ell\ell$ peaks. No wurtzite-structured $Al_xCr_{1-x}N$ (w-$Al_xCr_{1-x}N$) phase was observed despite the potential epitaxial relationship of $(111)_{MgO}||(0001)_{w\text{-}AlCrN}$ and $[1\bar{1}0]_{MgO}||[1\bar{2}10]_{w\text{-}AlCrN}$. HR-XRD was used to investigate the region $34° \leq 2\theta \leq 50°$, covering the 111 and 002 peak positions of c-$Al_{0.60}Cr_{0.40}N$ and c-$Al_{0.68}Cr_{0.32}N$ films of different thicknesses. Figures 1a and 1c show the 2θ-ω scans of $Al_{0.60}Cr_{0.40}N$ and $Al_{0.68}Cr_{0.32}N$ films on MgO(111). Samples with 180 min deposition time are comparable in peak position and intensity to the corresponding 60 min sample and, for

reasons of clarity, they are not displayed in Fig. 1. The peak center positions lie at 2θ values of ~36.94° and ~37.83° for c-$Al_{0.60}Cr_{0.40}N$/MgO(111) and ~36.94° and ~38.05° for c-$Al_{0.68}Cr_{0.32}N$/MgO(111).

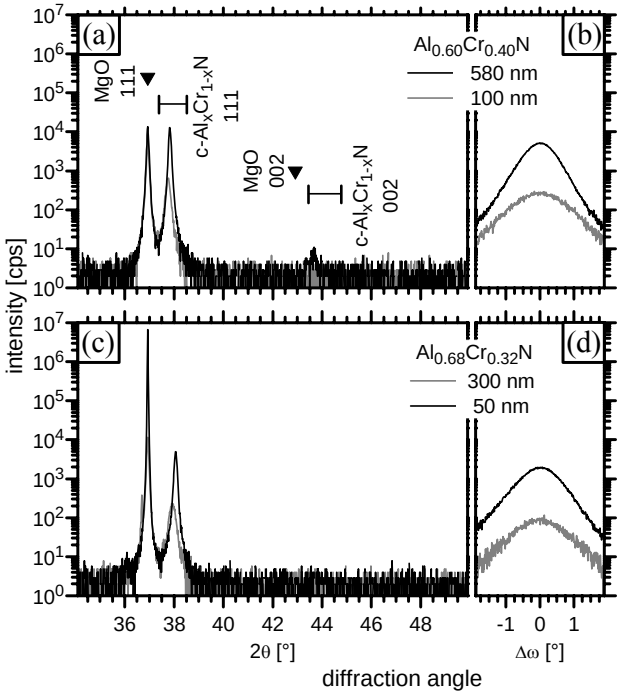

Fig. 1. HR-XRD scans of (a) $Al_{0.60}Cr_{0.40}N$ and (c) $Al_{0.68}Cr_{0.32}N$ films with the corresponding HR rocking curves (b) and (d), respectively, recorded at the position of maximum 2θ intensity. The theoretical positions are indicated for MgO [23] with a triangle, a range for c-$Al_xCr_{1-x}N$ is indicated with boarders corresponding CrN [18] and c-AlN [23].

The out-of-plane lattice parameters calculated from the above presented 2θ-positions result in 4.211 Å for MgO, which corresponds to the literature value of 4.211 Å [23]. The c-$Al_xCr_{1-x}N$ lattice parameters depend on the Al content as shown for polycrystalline coatings [3-6,8]. Here, the calculated lattice parameters are 4.116 Å for $Al_{0.60}Cr_{0.40}N$ and 4.093 Å for the $Al_{0.68}Cr_{0.32}N$ films, which are in good agreement with reported values. Heteroepitaxially grown films with comparable lattice mismatches like in the case of c-$Al_xCr_{1-x}N$/MgO are often described by the mosaic block model [24]. HR-XRD offers the possibility to access averaged vertical and lateral dimensions of these blocks by the peak width in the 2θ-ω scans (Figs. 1a and 1c) and the corresponding rocking curves (Figs. 1b

and 1d), respectively [25]. The full widths at half maximum in 2θ-ω (FWHM, Γ) is 0.04° for the MgO substrate peaks, 0.08° for the 580 nm $Al_{0.60}Cr_{0.40}N$ film, and 0.11° for the 300 nm $Al_{0.68}Cr_{0.32}N$ film. These values can be used as a measure for the vertical x-ray coherence length in the crystallites ($\xi_\perp$) [18,26-28], where smaller values indicate less defects, and/or a larger crystal size along the growth direction. For the bulk single-crystal substrates, this value is obviously smaller in comparison with films which show a natural limit for the crystal size in the vertical direction given by the film thickness. Obtained values are 120 nm for the 580 nm $Al_{0.60}Cr_{0.40}N$ film and 85 nm for the 300 nm $Al_{0.68}Cr_{0.32}N$ film showing relation to the total film thicknesses. This is also valid for the 100 nm $Al_{0.60}Cr_{0.40}N$ with $\xi_\perp$ = 54 nm ($\Gamma_{2\theta-\omega}$ = 0.17°) and the 50 nm $Al_{0.68}Cr_{0.32}N$ film with $\xi_\perp$ = 38 nm ($\Gamma_{2\theta-\omega}$ = 0.24°). A comparison of the calculated MgO substrate value of 150 nm with the ones of the thicker films (deposition time 60 and 180 min), however, show no pronounced absolute differences.

Rocking curves (ω-scans) over the 111 c-$Al_xCr_{1-x}N$ film peaks, corresponding to the 2θ-ω scans in Figs. 1a and 1c, are displayed in Figs. 1b and 1d. The FWHM of these ω-scans can be interpreted as a measure of the lateral x-ray coherence length $\xi_\parallel$, and therefore the lateral dimension of coherently diffracting domains in the different films can be compared. Absolute values for the FWHM of the thickest films are Γ_ω = 0.87° for the $Al_{0.60}Cr_{0.40}N$ (111) peak and Γ_ω = 1.11° for the $Al_{0.68}Cr_{0.32}N$ (111) peak. These Γ_ω values are higher compared to epitaxial layers of rock salt structure binary nitrides with comparable lattice mismatch, like 0.14° for TiN [26], 0.15° for CrN [18], or 0.6° for TaN [29]. Even materials that exhibit significantly larger lattice mismatches to MgO like HfN ($\Delta a \sim 7.5\%$) and ScN ($\Delta a \sim 7\%$) show smaller Γ_ω of 0.58° [27] and 0.87° [28], respectively, resulting in larger lateral coherence lengths. Calculating $\xi_\parallel$ for the thicker films (>10 min) of $Al_{0.60}Cr_{0.40}N$ and $Al_{0.68}Cr_{0.32}N$ by the relationship $\xi_\parallel = \lambda/(2\Gamma_\omega \sin\theta)$, using the Cu-$K_\alpha$ wavelength λ = 1.54056 Å, results in ~16 nm and ~12 nm, respectively. The 10 min deposited $Al_{0.60}Cr_{0.40}N$ and $Al_{0.68}Cr_{0.32}N$ samples exhibit higher Γ_ω than their thicker counterparts resulting in $\xi_\parallel$ of ~9 nm for both compositions. The small lateral dimensions of the diffracting domains may also influence the results of the vertical x-ray coherence length measurements, resulting in reduced $\xi_\perp$. Comparably lower lateral crystal

dimensions of the present c-$Al_xCr_{1-x}N$ films with the reported binary nitrides can be explained by two factors: (i) The MgO(111) templates used for epitaxial growth in this work provide a less stable heteropolar surface resulting in higher defect densities compared to the low energy MgO(001) surface, which was used in the other studies [18,26-29],. (ii) The c-$Al_xCr_{1-x}N$ (111) plan, provides three backbonds for the growing film which drastically decreases the surface ad-atom mobility. This phenomenon is further aggravated by the low substrate temperature employed in the present study.

Epitaxial relations between the MgO substrate and the as-deposited $Al_{0.60}Cr_{0.40}N$ and $Al_{0.68}Cr_{0.32}N$ films are investigated by 360° azimuthal scans over the 002 reflections (Fig. 2). The scans are performed at $2\theta = 44.055°$ for $Al_{0.60}Cr_{0.40}N$ (Fig. 2a), 44.287° for the $Al_{0.68}Cr_{0.32}N$ sample (Fig. 2b), and 42.930° for the MgO substrate (Fig. 2c), and prove an epitaxial cube-on-cube relation ($(111)_{MgO}||(111)_{c\text{-}AlCrN}$ and $[110]_{MgO}||[110]_{c\text{-}AlCrN}$) where the intensity maxima of the films lie at identical azimuthal angles as the (111) substrate peaks. However, next to the threefold symmetry of the substrate peaks (Fig. 2c), a second threefold symmetry with peaks of minor intensities and an azimuthal shift of 60° can be seen for the films in Figs. 2a and 2b. These contributions are due to the existence of either double positioning domains or stacking faults/microtwins on the (111) planes. However, their low intensity of 0.5% of the main epitaxial peaks indicates a marginal quantity that can only be seen with the open detector setup and the logarithmic scale.

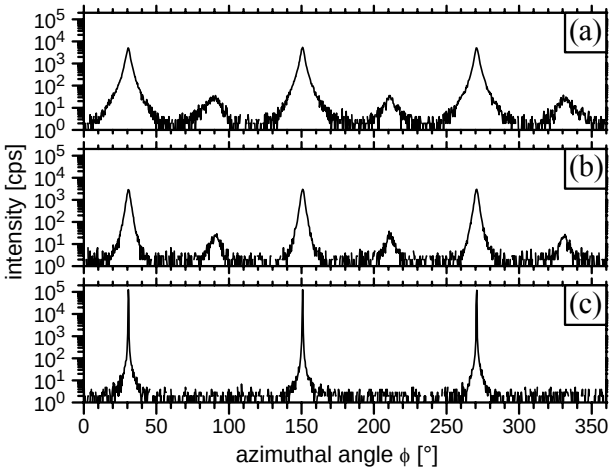

Fig. 2. Azimuthal XRD scans for $\Psi = 54.7°$ over the 002 reflections from (a) epitaxial $Al_{0.60}Cr_{0.40}N$ and (b) $Al_{0.68}Cr_{0.32}N$ films as well as from (c) the MgO(111) substrate.

Figure 3 shows reciprocal space maps (RSM) around the 113 reflection for films of both compositions (deposition time 60 min), with q_z and q_x aligned along the [001] and [110], respectively. Measured intensities of the $Al_{0.60}Cr_{0.40}N$ and the $Al_{0.68}Cr_{0.32}N$ film with their corresponding MgO substrate are displayed in Figs. 3a and 3b, respectively. The arrow indicates the direction through the origin of the reciprocal space. Both film 113 peak intensity distributions are centered on this line suggesting fully relaxed growth during the deposition process [25,30]. Consequently, the in-plane ($a_{\parallel}$) and out-of-plane ($a_{\perp}$) lattice parameters calculated from the q values of maximum intensity are identical within the accuracy of the measurement. Absolute values for MgO are $a_{\parallel} = a_{\perp} = 4.211$ Å, while $a_{\parallel} = 4.116$ and $a_{\perp} = 4.117$ Å for $Al_{0.60}Cr_{0.40}N$, and $a_{\parallel} = 4.095$ and $a_{\perp} = 4.096$ Å for $Al_{0.68}Cr_{0.32}N$.

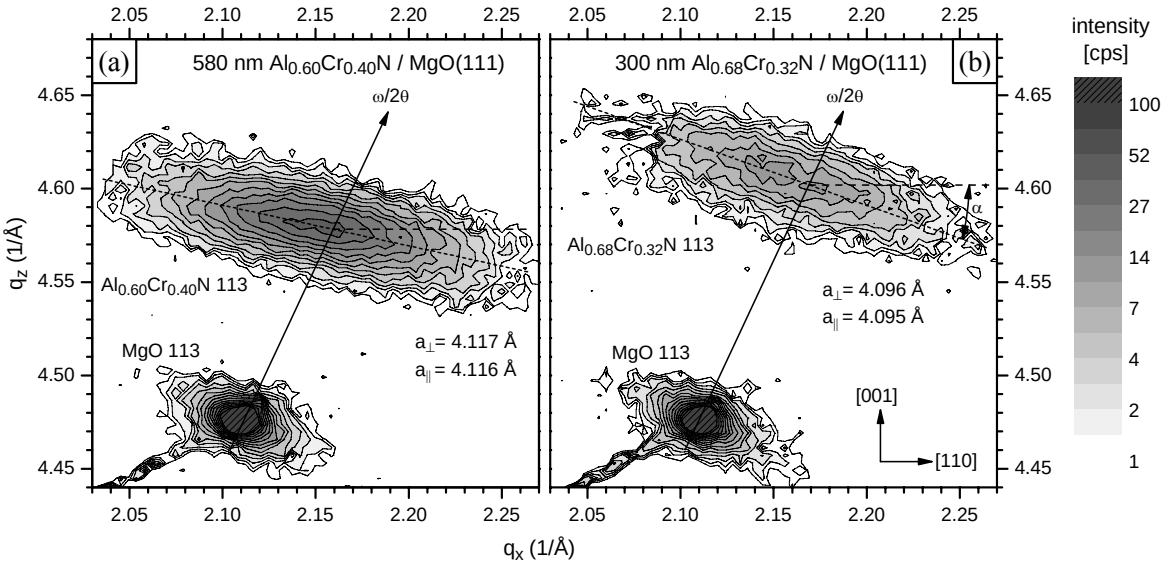

Fig. 3. Asymmetric RSMs around the 113 reflection from (a) epitaxial $Al_{0.60}Cr_{0.40}N$ and (b) $Al_{0.68}Cr_{0.32}N$ films grown on MgO(111). The intensity contours are projected into the plane with the orthogonal directions [001] and [110].

These values match the results from the 2θ-ω diffraction data in Figs. 1a and 1c, as well as from symmetric RSMs (not shown). Differences in total intensities for the films can be explained by the lower thickness of $Al_{0.68}Cr_{0.32}N$ compared to $Al_{0.60}Cr_{0.40}N$. The intensity distributions of the films are not lying perpendicular to the 2θ-ω line, but are tilted counterclockwise towards horizontal alignment. This tilt could be attributed to an influence

of the limited lateral coherence length [24], however, also the symmetric RSM exhibits a comparable tilt. Hence, the entire layer has grown with a tilt which can be calculated to be in the order of 3°. A possible explanation for the column tilt could be a minimization effect of the grain boundary energy given the initial film growth with a titled lattice induced by a substrate miscut of ~0.5°.

The above x-ray investigations suggest relaxed $Al_{0.60}Cr_{0.40}N$ and $Al_{0.68}Cr_{0.32}N$ films having epitaxial columnar film morphology with column diameters of a few nanometers, which extend over the entire film thicknesses of 1750 nm and 900 nm, respectively. The resulting lattice mismatches are ~2.26% for $Al_{0.60}Cr_{0.40}N$/MgO and ~2.81% for $Al_{0.68}Cr_{0.32}N$/MgO. Most film columns exhibit growth facets as can be observed in the SEM images in Fig. 4 for (a) fracture cross-section and (b) top view from the 1750 nm thick $Al_{0.60}Cr_{0.40}N$ film. Figure 4a depicts the fracture of the MgO substrate along the {001} cleavage planes and the fibrous columns of the film, which have cracked along their boundaries. For rock salt structures grown with (111) texture, the formation of cube corner shaped pyramids around the [111] direction is reported in literature [31]. SEM investigations of $Al_{0.60}Cr_{0.40}N$ films with different film thicknesses revealed full development of the pyramids already after 50 nm followed by a steady-state growth condition with little competition for growth between the columns where the pyramids formed by {001} planes mark their tips. This can be seen for the thick $Al_{0.60}Cr_{0.40}N$ film in Fig. 4a and b where areas of bigger facets in Fig. 4b can be related to surface defects of the initial MgO substrate resulting in regions of bigger pyramids. It is known for MgO that the (111) surface is difficult to prepare in perfect quality due to its heteropolar character [32,33].

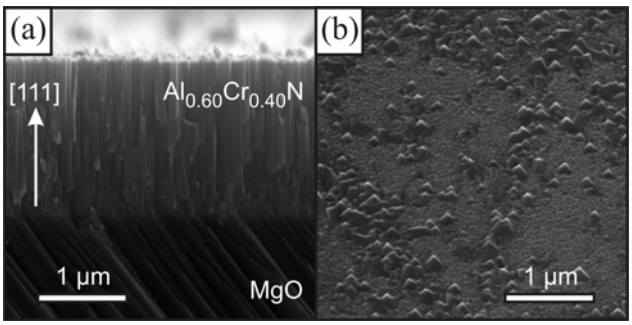

Fig. 4. SEM micrographs of (a) fracture cross-section and (b) top view of a 1750 nm thick $Al_{0.60}Cr_{0.40}N$ film grown on MgO(111).

The columnar microstructure is also apparent in cross-sectional TEM (XTEM) as shown by Fig. 5a which is an overview image from a 1750 nm thick $Al_{0.60}Cr_{0.40}N$ film grown on MgO(111). It confirms the HR-XRD results that the columns extend over the whole film thickness. Figure 5b shows the interface region of the $Al_{0.68}Cr_{0.32}N$ sample which possesses also a columnar structure. The magnified view in Fig. 5c, however, reveals that the columns are slightly narrower compared to the $Al_{0.60}Cr_{0.40}N$ case. Average column diameters for $Al_{0.60}Cr_{0.40}N$ (Fig. 5a) and $Al_{0.68}Cr_{0.32}N$ (Fig. 5b and c) correspond well to the calculated lateral x-ray coherence lengths. The regions of lower density along the columns, as indicated by the Fig. 5c, result from the non-planar growth with surface faceting leading to grooves that outline the apparent column boundaries which may, in case of a less energetic deposition, even be decorated by voids, as has been described for TiN and NbN epitaxial films [34].

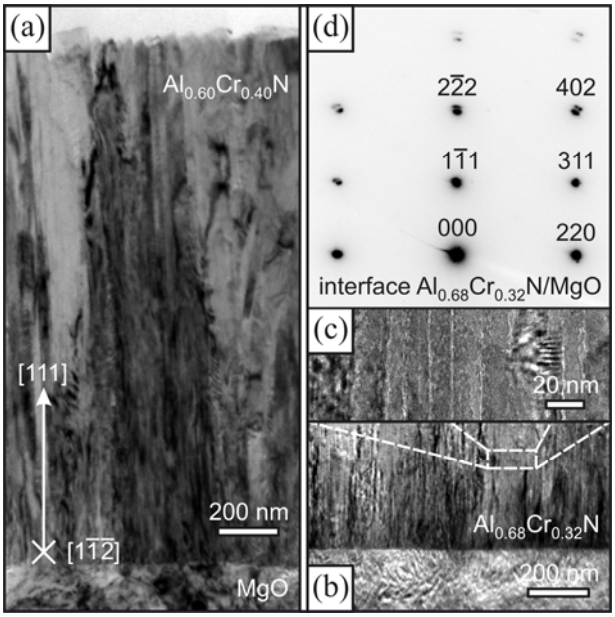

Fig. 5. (a) Cross-sectional TEM micrographs from $Al_{0.60}Cr_{0.40}N$ and (b) $Al_{0.68}Cr_{0.32}N$ films grown on MgO(111) with (c) magnified view of the columnar structure and (d) SAD spot pattern of the interface area.

The origin of this phenomenon is by self-shadowing at the film surface cusps in combination with limited ad-atom mobility. Figure 5d shows a SAD pattern, including the interface region of the $Al_{0.68}Cr_{0.32}N$ sample and the MgO substrate. The distinct spot pattern confirms epitaxial cube-on-cube relation and fully relaxed growth mode, since the

peak splits of MgO substrate and $Al_{0.68}Cr_{0.32}N$ film, especially seen for higher order reflections like (402), are aligned towards the direct beam spot. From the XTEM analysis also the obtained deposition rates from RBS could be verified.

4. Conclusion

Epitaxial $Al_{0.60}Cr_{0.40}N$ and $Al_{0.68}Cr_{0.32}N$ films can be grown on MgO(111) substrates by reactive unbalanced magnetron sputtering at deposition temperatures of 500 °C. The films grow in the rock salt structure with fully relaxed lattice parameters of ~4.116 Å for the $Al_{0.60}Cr_{0.40}N$ and ~4.093 Å for the $Al_{0.68}Cr_{0.32}N$ composition. A self-organized 3D island growth mode is observed resulting in fibrous epitaxial columns with diameters between 12 and 16 nm depending on composition. The columns extend over the whole film thickness, but are tilted slightly against the substrate normal and exhibit {001} facets on top. Differences in column diameter between the two investigated film compositions are connected with the diffusivity on the growth surface. The initial nucleus density on the (111) surface defines the final column width and depends on the Al and Cr ad-atom mobility. Differences in composition and hence mobility therefore result in different column widths.

Acknowledgments

The authors thank Dr. Fredrik Eriksson and Naureen Ghafoor (IFM – Thin Film Physics Division, Linköping University) for support regarding the deposition system. Beamtime support by the Tandem Accelerator Lab at Uppsala University, Sweden is acknowledged for the chemical analysis. Dr. Finn Giuliani and David Trinh (IFM – Thin Film Physics Division, Linköping University) are gratefully acknowledged for their assistance in TEM. The Christian Doppler Laboratory for Advanced Hard Coatings at the University of Leoben and the Plansee GmbH, Lechbruck, Germany, are acknowledged for providing target materials. Work done in Leoben was financed within the framework of the Austrian Kplus Competence Center Program. The work done in Linköping was financed by the Swedish Research Council (VR) and the Swedish Foundation for Strategic Research

(SSF) Strategic Research Center MS^2E on Materials Science for Nanoscale Surface Engineering.

Literature

[1] C. Kunisch, R. Loos, M. Stüber, S. Ulrich, Z. Metallkd. 90/10 (1999) 847.

[2] H. Hasegawa, M. Kawate, T. Suzuki, Surf. Coat. Technol. 200/7 (2005) 2409.

[3] Y. Ide, T. Nakamura, K. Kishitake, in: B. Mishra, C. Yamauchi (Eds.), Second International Conference on Processing Materials for Properties, TMS (The Minerals, Metals & Materials Society), San Francisco, 2000, p. 291.

[4] M. Kawate, A. Kimura, T. Suzuki, Journal of Vacuum Science & Technology A 20/2 (2002) 569.

[5] M. Hirai, Y. Ueno, T. Suzuki, W.H. Jiang, C. Grigoriu, K. Yatsui, Jpn. J. Appl. Phys. Part 1 - Regul. Pap. Short Notes Rev. Pap. 40/2B (2001) 1056.

[6] A.E. Reiter, V.H. Derflinger, B. Hanselmann, T. Bachmann, B. Sartory, Surf. Coat. Technol. 200/7 (2005) 2114.

[7] Y. Makino, Surf. Coat. Technol. 193/1-3 (2005) 185.

[8] P.H. Mayrhofer, H. Willmann, A. Reiter, 49th SVC Annual Technical Conference, Society of Vacuum Coaters, Washington, 2006, p. 575.

[9] H. Willmann, P.H. Mayrhofer, P.O.Å. Persson, A.E. Reiter, L. Hultman, C. Mitterer, Scr. Mater. 54/11 (2006) 1847.

[10] A.Y. Polyakov, N.B. Smirnov, A.V. Govorkov, R.M. Frazier, J.Y. Liefer, G.T. Thaler, C.R. Abernathy, S.J. Pearton, J.M. Zavada, Appl. Phys. Lett. 85/18 (2004) 4067.

[11] R.M. Frazier, G.T. Thaler, B.P. Gila, J. Stapleton, M.E. Overberg, O.R. Abernathy, S.J. Pearton, F. Ren, J.M. Zavada, J. Electron. Mater. 34/4 (2005) 365.

[12] D. Kumar, J. Antifakos, M.G. Blamire, Z.H. Barber, Appl. Phys. Lett. 84/24 (2004) 5004.

[13] Q. Wang, A.K. Kandalam, Q. Sun, P. Jena, Phys. Rev. B 73/11 (2006) 115411.

[14] A.Y. Polyakov, N.B. Smirnov, A.V. Govorkov, R.M. Frazier, J.Y. Liefer, G.T. Thaler, C.R. Abernathy, S.J. Pearton, J.M. Zavada, Journal of Vacuum Science & Technology B 22/6 (2004) 2758.

[15] S.Y. Wu, H.X. Liu, L. Gu, R.K. Singh, L. Budd, M. van Schilfgaarde, M.R. McCartney, D.J. Smith, N. Newman, Appl. Phys. Lett. 82/18 (2003) 3047.

[16] H. Willmann, P.H. Mayrhofer, L. Hultman, C. Mitterer, Journal of Vacuum Science & Technology A (submitted).

[17] W. Kalss, A. Reiter, V. Derflinger, C. Gey, J.L. Endrino, Int. J. Refract. Met. Hard Mat. 24/5 (2006) 399.

[18] D. Gall, C.S. Shin, T. Spila, M. Odén, M.J.H. Senna, J.E. Greene, I. Petrov, J. Appl. Phys. 91/6 (2002) 3589.

[19] J. Birch, S. Tungasmita, V. Darakchieva, in: T. Paskova, B. Monemar (Eds.), Vacuum Science and Technology: Nitrides as seen by the technology, Research Signpost, Kerala, 2002, p. 421.

[20] C. Engström, T. Berlind, J. Birch, L. Hultman, I.P. Ivanov, S.R. Kirkpatrick, S. Rohde, Vacuum 56/2 (2000) 107.

[21] F. Eriksson, G.A. Johansson, H.M. Hertz, J. Birch, Optical Engineering 41/11 (2002) 2903.

[22] M. Mayer, Technical Report, Max-Planck-Institut für Plasmaphysik, Garching, Germany, 1997.

[23] Powder Diffraction File (Card 45-0946 for MgO, Card 46-1200 for c-AlN), International Centre for Diffraction Data, ICDD - JCPDS, 1998.

[24] R. Chierchia, T. Böttcher, H. Heinke, S. Einfeldt, S. Figge, D. Hommel, J. Appl. Phys. 93/11 (2003) 8918.

[25] P.v.d. Sluis, J. Phys. D: Appl. Phys. 26/4A (1993) A188.

[26] C.S. Shin, S. Rudenja, D. Gall, N. Hellgren, T.Y. Lee, I. Petrov, J.E. Greene, J. Appl. Phys. 95/1 (2004) 356.

[27] H.S. Seo, T.Y. Lee, J.G. Wen, I. Petrov, J.E. Greene, D. Gall, J. Appl. Phys. 96/1 (2004) 878.

[28] D. Gall, I. Petrov, N. Hellgren, L. Hultman, J.E. Sundgren, J.E. Greene, J. Appl. Phys. 84/11 (1998) 6034.

[29] C.S. Shin, D. Gall, P. Desjardins, A. Vailionis, H. Kim, I. Petrov, J.E. Greene, M. Odén, Appl. Phys. Lett. 75/24 (1999) 3808.

[30] M. Birkholz, Thin Film Analysis by X-Ray Scattering, Wiley-VCH Verlag GmbH & Co. KGaA, Weinheim, 2006.

[31] B. Warot, E. Snoeck, J.C. Ousset, M.J. Casanove, S. Dubourg, J.F. Bobo, Appl. Surf. Sci. 188/1-2 (2002) 151.

[32] P.W. Tasker, Journal of Physics C: Solid State Physics 12/22 (1979) 4977.

[33] L.E. Toth, Transition Metal Carbides and Nitrides, Academic Press, Inc., New York, 1971.

[34] L. Hultman, L.R. Wallenberg, M. Shinn, S.A. Barnett, J. Vac. Sci. Technol. A 10/4 (1992) 1618.